Satellite Remote Sensing Investigations into Changing Ice-shelf Extents in the eastern Weddell Sea Sector of Antarctica

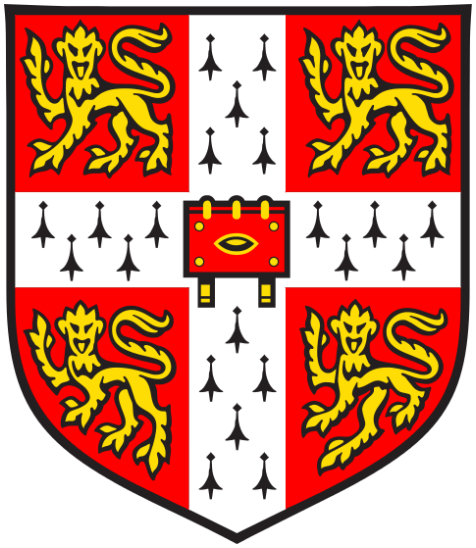

Nicholas Homer

July 2020

Submitted to the University of Cambridge for the degree of Master of Philosophy.

Scott Polar Research Institute | The University of Cambridge | Darwin College

Abstract

Satellite observations of ice-shelf collapse and related ice-mass drawdown from the Antarctic Peninsula over the past > 3 decades have been unambiguously linked to changes in atmospheric and oceanic processes as a result of anthropogenic climate change. Therefore, contemporary glaciological research is increasingly focussed on the long-term future stability of the vast West and East Antarctic Ice Sheets under different climate change scenarios, where similar changes to atmospheric and oceanic processes to those found in the Antarctic Peninsula are forecast. The floating ice shelves which extend from the ice sheet in these regions are of particular research interest because, by their very nature, they exert considerable control over the flow of the inland ice-sheet as well as respond relatively rapidly to external forcing mechanisms.

Here, new ice-shelf extent mapping is undertaken by mapping the calving front locations in the eastern Weddell Sea Sector of the East Antarctic Ice Sheet, where four of Antarctica's ten largest ice shelves are located. Calving fronts and other lengths of coastline were mapped using an adapted edge-extraction coastline delineation method, entirely within a GIS computing environment, from a variety of remotely-sensed satellite optical and radar imagery. Combined with pre-existing coastline products form the region a timeseries of ice-shelf areas is presented and discussed in the context of known and theorised ice-ocean-atmosphere interactions occurring in the region. In contrast to what is occurring in other regions of the Antarctic Ice Sheet, ice shelves are broadly found to have been synchronously advancing since the 1960s, with only the occasional detachment of large, tabular icebergs causing ice-shelf retreat on sub-decadal timescales. Most recently, total ice-shelf area along the eastern Weddell Sea coastline from Filchner to Fimbul ice shelves, inclusive, has been increasing by c. 550 km^2 yr^{-1} between 2009 and 2019.

Analysis of meteorological and sea-ice data suggests that increasing north to south surface wind-speed anomalies along the eastern Weddell Sea coastline are facilitating increased sea-ice concentrations at the margins of the ice shelves and it is argued that this may be increasing the ice-shelves' structural integrity, limiting iceberg calving activity. However, ultimately the ice shelves in this region are still primarily governed by bed-geometry and internal ice dynamical properties. Although this evidence is indicative of a region of the ice sheet in relative mass balance, the continuation of an identified surface air warming trend here will increase the likelihood of increased iceberg calving, or indeed ice-shelf retreat or collapse, as observed at the Anatectic Peninsula. However, further research is needed into the what affect warming might have on the large-scale atmospheric processes governing changes to the surface winds and related sea-ice concentration anomalies, so that better predictions as to the future of these ice shelves may be made.

Declaration

I certify that this dissertation is the result of my own work and includes nothing which is the outcome of work done in collaboration except where specifically indicated in the text.

This dissertation is not substantially the same as any work that has already been submitted before for any degree or other qualification except as declared in the preface and specified in the text.

Data sources and computer software used in this research are referenced in text, but additionally, initial computer scripts (MATLAB Antarctic Mapping Tools and XML SNAP processing scripts) were provided by Dr. Frazer Christie and Toby Benham, before being adapted. I confirm that all other processing scripts were developed by me.

The length of this dissertation does not exceed 20,000 words. This word count excludes the cover sheets, abstract, this declaration, acknowledgements, appendices, text in tables or figures and their captions, and the reference list.

Acknowledgements

I would like to express my thanks to Prof. Julian Dowdeswell for his valued glaciological expertise and advice throughout this research and his thorough feedback on draft manuscripts.

I am grateful to Dr. Frazer Christie's for sharing his glaciological, remote sensing and technical knowledge. Thank you to him and to Toby Benham for providing the aforementioned computer scripts and for further technical and GIS advice.

To all colleagues at SPRI, I extend a special thanks for providing such a welcoming, intellectually stimulating and fun environment in which to study.

Table of Contents

List of Figures

List of Tables

1 Introduction

1.1 Overall Aim

The overarching aim of this thesis is to present a new dataset of ice frontal positions along the eastern Weddell Sea (EWS) Sector of Antarctica over the past decade (2009 – 2019) and to discuss the presented changes in ice-shelf area, in the context of ice-ocean-atmosphere interactions in the sector.

1.2 Context and Justification

The Antarctic Ice Sheet (AIS) contains enough water to raise global average sea level by 58 m (Fretwell *et al.*, 2013). Satellite observations have shown that increasing contemporary sea level contributions originate from a non-uniformly thinning AIS (Helm *et al.*, 2014; McMillan *et al.*, 2014; Gardner *et al.*, 2018; Shepherd *et al.*, 2018, 2019; Rignot *et al.*, 2019), as well as from mountain glaciers and the Greenland Ice Sheet (Shepherd and Wingham, 2007; Rignot *et al.*, 2011b; Van den Broeke *et al.*, 2016; Zemp *et al.*, 2019). The AIS negative net mass balance originates largely from dynamically thinning marine-terminating glaciers and ice streams along the Antarctic Peninsula (AP) and draining marine basins of the West Antarctic Ice Sheet (WAIS). Ice-shelf collapse and dynamic thinning in these regions has been attributed to meteorological and oceanic drivers, some of which are ongoing and have been directly linked to anthropogenic climate change (e.g. Marshall *et al.*, 2006; Wåhlin *et al.*, 2010).

There has been some debate over the rate at which global sea levels will continue to rise in response to increased ice mass loss, and also concerning the long-term stability of the AIS, particularly due to continuing climate change under different emissions scenarios (Bamber and Payne, 2004; Stocker *et al.*, 2013; DeConto and Pollard, 2016). Given that sea level rise will have important global socio-economic implications (Mercer, 1978; Vaughan and Spouge, 2002), it is imperative that studies of glacier mass balance and dynamics remain a priority for all regions of the AIS, so that the magnitude and timescale of these changes can be better understood (Bamber and Payne, 2004; Pattyn and Morlighem, 2020).

Since 1820 when the first explorers set eyes Antarctica, its coastline marked by ice cliffs hundreds of metres high in places, has presented challenges for the maritime navigators and cartographers who set about mapping in the Southern continent. Surveys up to the present day have revealed that three quarters of the Antarctic coastline is fringed by ice shelves, covering an area of > 1.56 million km^2, or 11% of the total AIS area (Swithinbank, 1988; Rignot *et al.*, 2013). Advances in glaciology have revealed that these ice shelves exert an important control on the AIS mass balance, because ice leaves the continent either by melting off the base of the ice shelves, or by calving off their fronts as icebergs, at a present-day ratio of approximately 6:5 (Rignot *et al.*, 2013). The precise

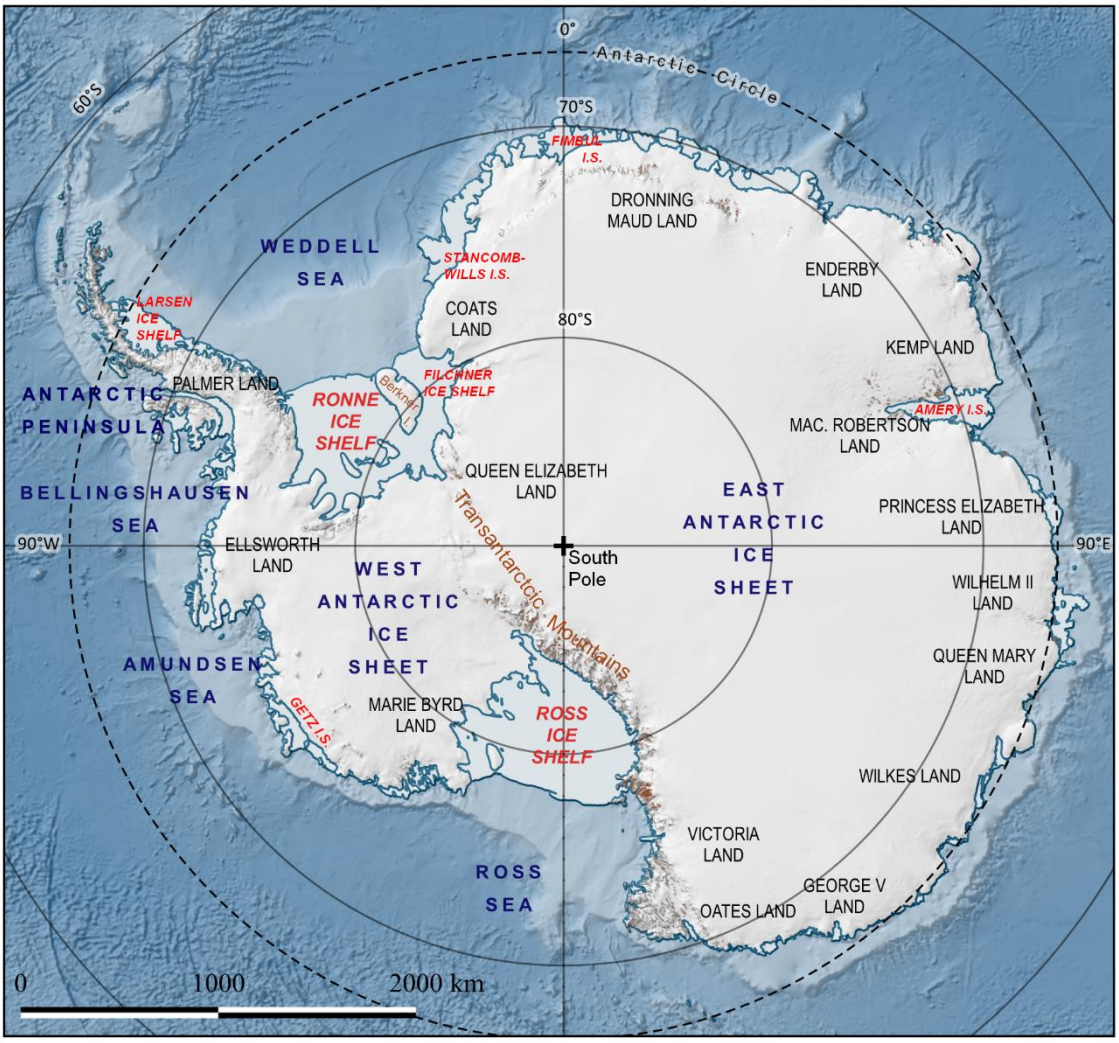

Figure 1.1: Overview map of Antarctica showing the main ice-sheet regions, sectors and major ice shelves. Data source: Norwegian Polar Institute and Quantarctica Contributors (2018).

balance between calving and undermelt is variable by region around the continent (Rignot *et al.*, 2013) and there is also a small component of loss from meltwater runoff, especially in the western AP. Ice shelves also dynamically limit the mass loss of grounded ice by way of ice-shelf buttressing, an effect which is clear to see in the accelerated drawdown of ice from the AP following the breakup of major ice shelves over the past 30 years (e.g. Scambos *et al.*, 2004). Nonetheless, some present-day mapping of ice shelves is motivated by maritime navigation or the logistics of running research stations in one of the most inaccessible places on Earth (e.g. Anderson *et al.*, 2014).

Regardless of motivation, the development and deployment of spaceborne remote sensing technologies since the 1960s has allowed for AIS coastal mapping studies on larger spatial and temporal scales, from daily monitoring of a single glacier tongue, up to mapping the entire AIS coastline for a given year. Nevertheless, there is still a disparity in the geographical focus of studies,

with relatively few ice-front mapping efforts so far undertaken for East Antarctic ice shelves and glaciers (Baumhoer *et al.*, 2018).

Ice shelf mapping requires the delineation of the calving front location (CFL), which is defined here as "the seaward limit of the ice shelf, ice tongue or ice sheet margin, where the ice front meets the ocean (where the ocean may be frozen)". This study presents a new CFL dataset is presented for the EWS region, consisting of digitised ice front locations from an assortment of Landsat-7, Landsat-8 and Sentinel-1 imagery in the years 2009, 2011, 2013, 2015, 2017 and 2019. Using this dataset, combined with existing CFL datasets, ice-shelf area changes since the 1960s are analysed and these changes are discussed in the context of the ice-ocean-atmospheric interactions occurring in the region. Furthermore, the semi-automatic CFL delineation method used in this thesis, which is undertaken entirely within a GIS computing environment, is presented and discussed.

1.3 Objectives

Given this context, which is set out in greater detail in Section 2, the objectives of this study are to:

- Describe a method for CFL delineation from various remotely-sensed imagery, using GIS software.
- Present new CFL and ice-shelf area datasets for the eastern Weddell Sea region of Antarctica for the years 2009, 2011, 2013, 2015, 2017 and 2019.
- Use these new datasets, combined with pre-existing CFL datasets, to analyse temporal variations in ice-shelf areas since the 1960s.
- Discuss these changes in the context of known and theorised ice-ocean-atmosphere interactions occurring in the region.

1.4 Thesis Structure

This thesis will first give a background to the latest understanding of the broadscale contemporary glaciological processes occurring at the Antarctica Ice Sheet (Sections 2.1.1 and 2.1.2), particularly at the continent's fringing ice shelves (Section 2.1.3) and the main mechanisms behind contemporary change to these systems (Section 2.1.3). A brief outline of existing Antarctic CFL datasets follows (Section 2.2.5), along with a discussion of the most common remote sensing and GIS methods used to create these products (Sections 2.2.1 to 2.2.4). A background of the EWS study location is then given (Section 2.3) and Section 2.4 provides a brief summary of previous glaciological study in the region.

In the methods section (Section 3), a semi-automatic radar and optical remotely-sensed imagery processing and CFL delineation method is presented (Sections 3.1 and 3.2) and estimated

error in measurements quantified (Section 3.6). The CFLs delineated using this method are presented in the results section (Section 4), along with ice-shelf area timeseries' created using a combination of new and existing CFL datasets (Sections 4.2 and 4.3). Meteorological and sea-ice data are also analysed to provide circumstantial evidence of the changes to external factors which might be driving the presented ice-shelf change (Section 4.4). Spatial and temporal CFL migration patterns are discussed in Section 5, and, combined with the sea-ice and meteorological datasets, the known and theorised ice-dynamical and ice-ocean-atmosphere mechanisms of change in the EWS region are explored (Sections 5.2 and 5.2.5).

2 Background and Previous Calving Front Location Studies in Antarctica

2.1 The Antarctic Ice Sheet: Dynamics and Contemporary Change

2.1.1 Antarctic Ice Sheet Mass Balance

Satellite observations have revealed that increasing contemporary sea level contributions originate from a non-uniformly thinning AIS (Helm *et al.*, 2014; McMillan *et al.*, 2014; Gardner *et al.*, 2018; Rignot *et al.*, 2019) as well as from Greenland and smaller ice caps and mountain glaciers (Shepherd and Wingham, 2007; Rignot *et al.*, 2013; Van den Broeke *et al.*, 2016; Zemp *et al.*, 2019). The Antarctic contribution averaged 0.49 – 0.73 mm yr^{-1} between 1992 and 2017, resulting in a total ice mass loss of 2725 ± 1400 Gt from the continent (Shepherd *et al.*, 2018, 2019). Recent numerical modelling has shown the likelihood for the mass-loss trend to continue for a set of global-warming scenarios, with the AIS potentially contributing between 0.5 and 1 m to global mean sea level rise by 2100 and furthermore, several meters on centennial timescales, under an average global atmospheric warming of 2°C above pre-industrial levels (Cornford *et al.*, 2015; Feldmann and Levermann, 2015; Ritz *et al.*, 2015; DeConto and Pollard, 2016). Albeit, these forecasts vary significantly between c. 10 cm and up to over 1 m by 2100. Further thinning, acceleration, ungrounding and mass loss from the marine-based WAIS are almost unanimously predicted by modellers (e.g. Feldmann and Levermann, 2015; Golledge *et al.*, 2015; Ritz *et al.*, 2015; DeConto and Pollard, 2016); however, a lack of knowledge around the future stability of the much larger (> 10 million km^2; 52.2 m sea level equivalent) East Antarctic Ice Sheet (EAIS) mean that these significant uncertainties in the total magnitude and timescale of future sea level contributions from the AIS remain (Stocker *et al.*, 2013; Pattyn and Morlighem, 2020).

Recent studies have found only 0.6% of the contemporary EAIS to be in dynamical imbalance (Shepherd *et al.*, 2019) with many parts of its huge interior drainage basins actually gaining mass (Gardner *et al.*, 2018; Shepherd *et al.*, 2018, 2019). However, evidence to suggest that sea levels were 10 – 30 m higher during the Pliocene, a time when atmospheric carbon dioxide concentrations were similar to what they are today at c. 400 p.p.m.v., has led to authors theorising about the possibility of sea level contributions originating in the EAIS on a scale an order of magnitude larger than that currently modelled for the WAIS (Miller *et al.*, 2012; Cook *et al.*, 2013; Rovere *et al.*, 2014). In order that sophisticated Earth systems models are better able to constrain sea level change predictions from the AIS, and in particular the EAIS, studies of glacier dynamics and mass balance in all regions of the AIS should continue to remain a priority.

One element of ice dynamics which is particularly poorly replicated by current models is the incorporation of non-linear temporal ice-shelf behaviour, particularly iceberg calving from the glacier fronts (Van der Veen, 2002; Åström *et al.*, 2014), a challenge which has been highlighted as one of the remaining "grand challenges" in ice sheet modelling (Pattyn and Morlighem, 2020) and, therefore, one which several groups are currently investigating (e.g. Liu *et al.*, 2015; DeConto and Pollard, 2016). High-resolution CFLs, and their variability through time, are needed to validate models and to aid this research with the aim of developing a general calving law (Pattyn and Morlighem, 2020).

2.1.2 Antarctic Ice Sheet and Ice Shelf Dynamics

Ice mass gained through accumulation of precipitation on an ice sheet is transported to the ice sheet margins via a network of ice streams and outlet glaciers (Rignot *et al.*, 2011a) draining significant catchment basins (Zwally *et al.*, 2012). At the coast ice typically becomes ungrounded and extends onto the surface of the sea as floating glacier tongues or ice shelves with a sometimes-extensive ocean-water filled cavity beneath. Ultimately, Antarctic ice ends up in the ocean through basal melt of these ice shelves or calving of icebergs at their fronts when the yield strength of the ice is overcome (Pollard *et al.*, 2015). Where the ice sheet-shelf system is in dynamical balance this lost mass is replaced by the flux of grounded ice across the GL into the ice shelf and thus the thickness, areal extent, and mass of the ice shelves is sustained. Because of this, over decadal timescales, CFLs fluctuate in a cyclical manner, as ice calves off either as large discrete tabular icebergs (e.g. Van der Veen, 2002; Massom *et al.*, 2015), or by way of spatially extensive disintegration into numerous smaller icebergs e.g. Larsen A and B Ice Shelves (Scambos *et al.*, 2003, 2009), and is replaced by the flow of inland ice (Cook *et al.*, 2005; Benn *et al.*, 2007; Bassis and Jacobs, 2013). CFL retreat (advance) then, is a result of either decreased (increased) mass flux from the grounded potion of the ice sheet, due to decreased (increased) accumulation or velocity, or an increase (decrease) in iceberg calving, which may be driven by increased (decreased) basal melt. However, basal melting can initiate complex feedbacks, whereby reduced back stress from a thinning ice-shelf leads to increased ice-flow velocities leading to an advance in the CFL (see Section 2.1.3).

In the AIS's current configuration, negative net ice-shelf mass balance is an outcome of enhanced basal melt and retreat due to iceberg calving, with minor mass loss due directly to surface ablation and/or accumulation change (Shepherd *et al.*, 2018; Pattyn and Morlighem, 2020). Overall, basal melt is the greater contributor to ice shelf mass loss than the calving flux at 1325 ± 235 Gt yr^{-1} and 1089 ± 139 Gt yr^{-1}, respectively (Rignot *et al.*, 2013). However, this general trend is spatially nonuniform across the AIS, with EAIS ice shelves, which have higher calving than basal-melt flux, actually gaining volume of 148 ± 45 km^3 yr^{-1} between 1994 and 2003, albeit declining somewhat to 56

± 37 km^3 yr^{-1} between 2003 and 2012, compared to overall AIS ice-shelf volume loss of 166 ± 48 km^3 yr^{-1} (Paolo *et al.*, 2015).

Whilst mass loss from ice shelves to the sea does not directly influence sea level (because the ice is already floating, causing water displacement), a reduction in the extent and thickness of ice shelves along the AP and WAIS coast has altered the flow of inland ice, triggering retreat, thinning, acceleration and ungrounding (manifested as grounding line (GL) retreat) of many marine terminating ice streams, which does cause additional sea level rise. The thinning and removal of ice shelves means that these glaciological changes propagate inland because ice shelves buttress the flow of grounded ice through back stress forces at the ice-bed boundary (Dupont and Alley, 2005; Goldberg *et al.*, 2009). Therefore, the removal of ice shelves can result in a self-sustaining destabilising feedback, whereby thinning leads to GL retreat and a loss of basal friction below the newly ungrounded ice, resulting in further thinning, acceleration and retreat (Joughin and Alley, 2011; Park *et al.*, 2013; Pattyn and Morlighem, 2020). Recent observations and modelling have confirmed how retreat of ice shelves can lead to an increase in ice drawdown and rapid collapse of glaciers (e.g. Scambos *et al.*, 2004; De Rydt *et al.*, 2015; Gudmundsson *et al.*, 2019), illustrating how ice sheet mass balance is tightly coupled with ice-shelf and glacier-tongue area and thickness. For example, on the Antarctic Peninsula, the rapid breakup and removal of about 28,000 km^2 of ice shelves over the past 60 years (Cook and Vaughan, 2010), such as Larsen A and B in 1995 and 2002 (Rott *et al.*, 2002), has been linked unambiguously to the subsequent c. 20% - 40% acceleration of tributary glaciers (Scambos *et al.*, 2004; Jacobs *et al.*, 2011; Seehaus *et al.*, 2018).

2.1.3 Mechanisms of Antarctic Ice Shelf Change

Early observations of ice shelf locations relative to the 0°C January air-temperature isotherm, led to Mercer (1978) hypothesising that atmospheric warming would lead to instability of the West Antarctic ice streams and glaciers due to atmospheric changes driving ice-shelf thinning or break-up. Since then, the buttressing ice shelves along the AP have undeniably been undergoing systematic brake-up and retreat, with atmospheric warming leading to increased surface melting and subsequent iceberg calving due to hydrofracture by meltwater ponding (Benn *et al.*, 2007; Pritchard and Vaughan, 2007; Scambos *et al.*, 2009). However, this mechanism of ice-shelf retreat is unlikely to occur on a large scale in other regions of the AIS at present due to a relative lack of surface meltwater given the colder air-temperatures, although temperatures may increase in the future due to atmospheric warming. What has become increasingly clear is that increased basal melt has also contributed to the breakup of AP ice shelves, particularly in the southwest AP, where mid-ocean waters have warmed by more than 0.5°C on average since the 1990s (Pritchard *et al.*, 2012; Cook *et al.*, 2016).

The focus of much recent research into AIS mass loss has shifted to the larger marine basins of the WAIS, particularly to the large, fast-flowing, ice streams draining the Amundsen Sea and Bellingshausen Sea sectors (Holland *et al.*, 2010; Turner *et al.*, 2017). Here, the role of ocean-water driven basal melting is clear, with ice-dynamical changes resulting from the increasing inflow of warm, salty Circumpolar Deep Water (CDW) across the continental shelf into sub-ice-shelf cavities, increasing basal melt rates and enhancing GL retreat (e.g. Jacobs *et al.*, 1992, 2011; Wåhlin *et al.*, 2010; Christie *et al.*, 2018; Konrad *et al.*, 2018). A concentrated research effort of observational and modelling studies has shown how glaciological changes occurring in the Amundsen and Bellingshausen sea regions are a result of tightly coupled ice-ocean-atmosphere interactions, where the removal of the buttressing ice shelves is largely being driven by oceanic basal melt due to increased CDW inflow, which is influenced by synoptic atmospheric conditions on a regional and hemisphere wide scale such as the El Niño Southern Oscillation (ENSO) and the Southern Annular Mode (SAM) (Thoma *et al.*, 2008; Pritchard *et al.*, 2012; Steig *et al.*, 2012; Dutrieux *et al.*, 2014; Christie *et al.*, 2016; Nicolas *et al.*, 2017; Turner *et al.*, 2017; Deb *et al.*, 2018; Paolo *et al.*, 2018; Rignot *et al.*, 2019).

The EAIS has not attracted the same level of concentrated glaciological research interest as the WAIS, probably as a result of the more modest mass-balance changes which are occurring in comparison to at the AP and WAIS (Shepherd *et al.*, 2018). However, with the increasing debate over the long-term sea level contributions from Antarctica, has come increasing interest in EAIS glaciological study. Mass flux from the EAIS is governed to a larger degree by iceberg calving than basal ice-shelf melt, although basal melt here too is not insignificant (Rignot *et al.*, 2013). As such, the mechanisms governing calving are more significant here. There is some debate as to whether calving is the cause or the result of the ice-sheet dynamics discussed above (Benn *et al.*, 2007); that is to say, does iceberg calving trigger dynamic changes up-glacier, including flow acceleration and thinning (Hughes, 1996), or is increased iceberg calving the result of changes in other parts of the glaciological system, for example thinning and weakening of ice shelves (Van Der Veen, 1996; Van der Veen, 2002). In the absence of surface meltwater to cause hydrofracturing, calving is ultimately a result of the natural cycle of ice-shelf stretching in response to large-scale ice velocity gradients, particularly where the glacier becomes afloat, but is aided by ice-shelf weakening through basal melt (Benn *et al.*, 2007). In fact, the recent hypothesis of marine ice cliff instability (MICI), theorises that ice cliffs higher than about 90 m above the sea surface become unstable and collapse, aided by basal melt, facilitating rapid ice-sheet marginal retreat (DeConto and Pollard, 2016; Pattyn and Morlighem, 2020). Therefore, the ice-ocean-atmosphere interactions which exert control on ice-shelf basal melting, will likewise have an effect on iceberg calving rates and magnitudes, as the two processes are fundamentally linked (Ma and Bassis, 2019), resulting in associated knock-on effects for up-glacier grounded ice.

Whether changes are attributed to atmospheric or oceanic drivers at a given ice shelf, bed morphology is an additional important controlling factor. For the flow of grounded (upstream) ice, bed troughs can exert control on the velocity of flow (Rignot *et al.*, 2011a), and bed rises can act as local basal or lateral pinning points for ice shelves, enhancing ice-shelf buttressing (Alley *et al.*, 2007; Jenkins *et al.*, 2010). Moreover, bed morphology can influence the access of melt-inducing CDW to ice-shelf bases and GLs, via for example, routing of CDW through cross continental-shelf troughs (Walker *et al.*, 2007; Assmann *et al.*, 2019), or by retarding oceanic water access to GLs across localised bed ridges (Jenkins *et al.*, 2010; Dutrieux *et al.*, 2014). In fact, bed morphology is what makes the WAIS particularly vulnerable to glaciological change by oceanic basal melting because it is a marine-based ice sheet, with bed troughs deepening towards the interior to depths > 2000 m (Morlighem *et al.*, 2020). It is therefore susceptible to marine ice sheet instability (MISI) due to unstable GL retreat in a positive feedback of thinning, acceleration and ungrounding in deepening water (Weertman, 1974; Schoof, 2007). Thus, geometric parameters of individual glacier basins in addition to ice sheet dynamics, are important in studies of glaciological change (Lovell *et al.*, 2017; Seehaus *et al.*, 2018) as most basins of the AIS are at least partially grounded below sea level (Fretwell *et al.*, 2013; Morlighem *et al.*, 2020), and, furthermore, even ice streams which are not affected by retrograde bedrock slopes may be susceptible to MICI (Morlighem *et al.*, 2020; Pattyn and Morlighem, 2020).

One additional determining factor in ice-shelf change in all regions of the AIS is the presence of sea ice. The effect of sea-ice formation on basal melt is evident in that sea-ice formation fundamentally affects CDW Ekman transport by altering the water column through the production of high-salinity water due to salt expulsion from the freezing seawater (Nicholls *et al.*, 2009). Although studies on the effects that predicted future sea-ice reductions (Stocker *et al.*, 2013) will have on AIS ice shelves are limited, both in terms of change mechanisms and in quantification of rates, one hypothesis is that basal melt might decrease in areas with deep GLs, leading to a stabilisation of upstream ice, due to reducing CDW advection as a result of reducing sea-ice formation (Nicholls, 1997; Nicholls *et al.*, 2009).

A further effect of sea ice is that the presence of thick multiyear landfast sea ice (fast ice) can act to increase the stability of buttressing of ice shelves by increasing their mechanical strength, reducing calving, and so a reduction in sea ice can also lead to increased rates of calving (Khazendar *et al.*, 2009; Massom *et al.*, 2010, 2018; Carr *et al.*, 2013; Miles *et al.*, 2017; Robel, 2017). Clearly, sea-ice formation is itself affected by atmospheric and oceanic circulation on a regional and hemisphere-wide scale (Maqueda *et al.*, 2004; Miles *et al.*, 2017; Turner *et al.*, 2017; Scott *et al.*, 2018) and is therefore interlinked to other ice-ocean-atmosphere interactions which are driving change around the coasts of the AIS and having important implications for AIS mass balance.

As an illustrative example, increased iceberg calving at the ice front, as a result of increased ice-shelf basal melt (Ma and Bassis, 2019) from enhanced CDW transport, affects the inflow of waters into the sub-ice-shelf cavity by altering the water column and the geometry of the cavity (Nicholls *et al.*, 2009). This, in turn, has implications for sea-ice formation and the mechanical strength of the ice-shelf system (Robel, 2017), potentially leading to destabilising positive feedback of retreat and mass loss (Thoma *et al.*, 2006). It should further be noted that internal ice dynamics, rheology and the propagation of fractures, should not be omitted in studies of CFL change, as these variables are fundamental to the flow and calving-regime of ice-shelves (Rau *et al.*, 2004; Khazendar *et al.*, 2007, 2009; Davies *et al.*, 2012; Anderson *et al.*, 2014; Cook *et al.*, 2014; Huber *et al.*, 2017; Lovell *et al.*, 2017).

The CFL is thus an important parameter for ice-sheet modelling, as well as being a proxy measure of ice-shelf area, which has important implications in glaciological studies of ice sheet dynamics and iceberg calving. Given the variety of controlling factors on ice-shelf dynamics, the knock-on impact of this on ice-sheet dynamics, and the decadal timescales over which these processes occur, monitoring of contemporary ice-shelf frontal positions remains a priority, as do studies of past ice-shelf change in lesser studied regions (Baumhoer *et al.*, 2018). In addition, CFL mapping may be warranted for maritime navigation, cartographical or logistical reasons (e.g. Anderson *et al.*, 2014). Regardless of rationale, the dynamic nature of ice shelf and glacier tongue fronts means that regular CFL monitoring is required.

2.2 Remote Sensing of Ice Fronts Around Antarctica

Prior to the availability of remote sensing instrumentation and techniques, mapping of the polar regions was a time-intensive, laborious and expensive task. The launch of the first spaceborne remote sensing instruments in the 1960s has led to a revolution in the mapping of the world's ice masses, particularly in the inaccessible polar regions, and cartographers and glaciologists have used the newly available datasets, ever increasing in quality and size, to identify the margins of the ice sheets as the boundary between land/ice and water in remotely sensed imagery. Today, numerous studies have attempted to delineate the AIS CFLs, from repeated mapping over a small geographical area to quantify temporal change, up to delineating the entire AIS coastline for a given year. A comprehensive review of the existing AIS CFL products has been written by Baumhoer *et al.* (2018), who also discuss the advantages and limitations of the different remote sensing technologies and mapping techniques in mapping CFLs. This section presents a brief overview of the different remote sensing technologies and techniques that have been used to map changing CFLs around the AIS.

2.2.1 Optical Remote Sensing

Multispectral optical satellite sensors have been used to map the AIS since the 1970s (e.g. Swithinbank and Lucchitta, 1986; Swithinbank, 1988; Williams *et al.*, 1995; Cook *et al.*, 2016; Huber *et al.*, 2017) and have been used in 50% of all published AIS CFL studies reviewed by Baumhoer *et al.* (2018). The USGS Landsat satellite series is the most popular satellite mission for imaging CFLs in glaciological and cartographical studies alike, due to its continuous time-series since the 1970s, open data access, relatively-high-resolution (tens of meters) imagery and pre-processed scenes (Baumhoer *et al.*, 2018). Landsat imagery remains important today in the format of Thematic Mapper (TM), Enhanced Thematic Mapper Plus (ETM+) and Operational Land Imager (OLI) products produced from imagery from the recent Landsat-7 (launched 1999) and Landsat-8 (launched 2013) satellites (Raup *et al.*, 2015). For studies aiming to delineate the coastlines of larger regions, or indeed the entire AIS coastline, MODIS imagery is an often-used optical satellite mission, due in part to its relatively high temporal resolution with daily revisit cycles (e.g. Scambos *et al.*, 2007; Patel *et al.*, 2020), but this is traded-off for lower spatial resolution (250 m) than Landsat. Recent declassification of US military satellite imagery from the 1960s has allowed CFLs to be mapped in certain regions a further decade earlier, back to the early 1960s (Kim *et al.*, 2001, 2007). In spite of its wide adoption, optical remote sensing imagery is not ideally suited to CFL studies due to the long, dark winters and changeable meteorological conditions which prevail over the polar regions, often with persistent cloud cover (Paul and Hendriks, 2010), and although multispectral sensors overcome some of these issues, distinguishing the ice shelf from snow-covered fast ice or identifying the CFL in areas of high crevassing, for example, requires expert knowledge and remains subjective.

2.2.2 Radar Remote Sensing

The launch of synthetic aperture radar (SAR) satellite remote sensing instrumentation in the 1990s has allowed useful imagery to be acquired year-round, regardless of light and weather conditions, and has facilitated better differentiation between ice types, due to higher contrast imagery (Wuite *et al.*, 2019). (Williams *et al.*, 1995) updated the earlier optical-derived coastal maps of Antarctica, incorporating radar imagery from the European Remote Sensing (ERS-1) satellite. Later, the RADARSAT-1 Antarctic Mapping Project (RAMP) (Jezek, 1999) created the first ever high-resolution (125 m) radar image mosaic of the entire AIS in 1997 and was updated in 2000 (Jezek, 2002). More recently, Liu *et al.* (2015) studied circum-Antarctic mass balance using manually delineated coastlines from European Space Agency (ESA) Envisat SAR imagery captured between 2005 and 2011, finding one third of AIS mass loss was due to calving. In total, Baumhoer *et al.* (2018) found radar remote

sensing satellites to be used in one third of reviewed CFL studies, with ERS and RADARSAT the most frequently cited satellite missions.

Despite the all-light, all-weather capability of radar sensors, imagery is usually lower resolution than optical imagery (c. 40+ m compared with c. 10+ m) and speckle noise can be a problem in CFL identification, including in automatic mapping approaches (Wu and Liu, 2003). Furthermore, speckle and wind roughened seas lower the intensity contrast between sea, land and ice/snow, causing for example fast ice to have similar backscatter values to those on the ice shelf (Mason and Davenport, 1996; Liu and Jezek, 2004; Modava and Akbarizadeh, 2017; Baumhoer *et al.*, 2019).

2.2.3 Coastline Delineation

The vast majority (85%) of Antarctic CFL remote sensing studies use manual delineation to extract CFLs (Baumhoer *et al.*, 2018), which requires expert knowledge to differentiate between the ice sheet, sea ice and the ocean in satellite imagery and digitising skills using GIS software. In fact, even with expert knowledge, there are likely to be scenes in which it is impossible to differentiate between fast ice and ice shelf, for example, and for this reason scientists often use a variety of satellite imagery of different sensor types in a "use all the data you can get" methodology. An example of such a study is (Lovell *et al.*, 2017), who manually mapped 135 EAIS glacier tongues over six timesteps between 1988 and 2013, using a variety of radar and optical satellite sensors, again demonstrating the capability of remotely sensed data in CFL studies.

Clearly, manual delineation is time-consuming and subject to human digitising error and, therefore, there have been numerous attempts to part-automate or fully-automate the process of CFL extraction from satellite scenes. (Sohn and Jezek, 1999) developed a method to map the ice-sheet margins automatically from ERS-1 and SPOT imagery using a Robertson Edge Detection algorithm, but issues related to snow cover prevented the technique from being deployed over a significant area. (Wu and Liu, 2003) used traditional image processing techniques including histogram screening for feature extraction and texture analysis for feature classification, but their approach was rather generalised, requiring manual thresholding adjustments and their output required some manual corrections. The first complete high-resolution (25 m) Antarctic coastline product was produced by Liu and Jezek (2004), who applied despeckling followed by a Canny Edge Detection algorithm to mosaiced RADARSAT-1 SAR imagery (Jezek, 1999, 2002). Despite using locally adapted thresholding to classify the edges, manual corrections were still required to produce the finished product, which the authors meant to be used as a consistent baseline in future circum-Antarctic coastal mapping campaigns. More recent studies have followed a similar approach, using edge detection algorithms with post-processing manual corrections (e.g. Liu *et al.*, 2015; Miles *et al.*, 2017). For example, (Miles *et al.*, 2017) were able

to map 65% of CFLs from MODIS imagery without manual corrections by classifying ice and seawater and delineating the line between these areas.

A fully automatic approach to CFL delineation in Antarctica is that of (Klinger *et al.*, 2011), who developed an algorithm to pull active contours ("snakes") inwards towards the new CFL, from a previously known CFL. This technique requires previous CFL data as input and it was noted that this method had a high computing cost and thus, further research is needed to make use of this method on a large scale. In spite of these efforts, and those attempting similar CFL delineation on the Greenland Ice Sheet (e.g. Seale *et al.*, 2011; Krieger and Floricioiu, 2017), no fully-automatic method yet exists to extract CFLs and, thus, (Baumhoer *et al.*, 2018) conclude that semi-automatic methodologies provide the best trade-off between algorithm development time and accuracy in CFL mapping studies, at least for now, whilst work to develop fully autonomous deep-learning methodologies is ongoing (e.g. Baumhoer *et al.*, 2019; Mohajerani, 2019; Zhang *et al.*, 2019). The majority of semi-automatic methods discussed above require specialist knowledge of software or algorithm development outside the standard GIS computing environments, or require conversion between data types and are, hence, time-consuming and limited to deployment by experts.

In an effort to amalgamate data, the most recent publicly available digitised CFLs are made available on the Scientific Committee on Antarctic Research (SCAR) Antarctic Digital Database (ADD) map viewer (Fox *et al.*, 2012), with different parts of the AIS coastline being digitised by different research groups. Although this data availability is a major asset to AIS research, historical coastal datasets are only available along the AP and addition of coastal change datasets for other regions would be important additions.

2.2.4 Methods to Measure Calving Front Dynamics

To determine temporal change in CFL, change detection techniques involving the comparison of two or more geo-referenced CFLs must be undertaken. The ice-shelf terminus position is a commonly used measure of change (e.g. Frezzotti and Polizzi, 2002; Fountain *et al.*, 2017; Lovell *et al.*, 2017; Miles *et al.*, 2017), with several different techniques including the centre flow line distance, simple lines distance, box area or shelf area, being developed (Lea *et al.*, 2014). Ice-sheet, basin, or indeed entire AIS, areal change is the method favoured for large-scale analyses of coastal sections encompassing more than one ice shelf (e.g. Kim *et al.*, 2001; Liu *et al.*, 2015; Patel *et al.*, 2020) and when combined with thickness measurements, can be used to map volumetric change and mass balance (Liu *et al.*, 2015). The assumption of a temporally fixed reference point (i.e. basin boundary or GL), can be made so that areal change is an accurate proxy measure of CFL change (e.g. Frezzotti and Polizzi, 2002). An example large-scale study of ice-shelf areal change is the work of Cook *et al.* (Cook *et al.*, 2005, 2014;

Huber *et al.*, 2017), who have amalgamated CFL records along the AP from earlier studies and joined them with basin outlines to calculate basin areal change since the 1940s.

One further novel method to delineate the CFL at a high temporal resolution is the "elevation change" method developed by Wuite *et al.* (2019) using CryoSat-2 altimeter data. Promising initial results measured the calving rate of Filchner Ice Shelf to be 9 ± 1 Gt yr^{-1} between 2011 and 2018.

2.2.5 Previous Regional Calving Front Location Studies in Antarctica

Baumhoer *et al.*'s (2018) amalgamation of results showed a general trend of ice-shelf retreat to dominate around the AIS between 1972/75 and 1988/95, before switching to broadscale advances between 2000/01 and 2009/2015. Although the AIS has lost a total area of 16,000 km^2 between 1997 and 2016 (Patel *et al.*, 2020), the broadscale areal reduction trend is underlain by regional variations over different timescales. Cook *et al.* (Cook *et al.*, 2005, 2014, 2016; Cook and Vaughan, 2010; Huber *et al.*, 2017) have carried out the most comprehensive research into the collapse of ice shelves on the AP, finding 90% of glacier fronts have systematically retreated since their earliest known position, leading to a direct sea level contribution from accelerated glacier drawdown resulting from a reduction in ice-shelf buttressing, attributed to enhanced oceanic and atmospheric melt discussed above (Section 2.1.3).

CFL trends are less clear across the WAIS, where there have been spatially variable fluctuations, apparent even across single ice streams (Rignot, 2002; Pritchard *et al.*, 2012; Baumhoer *et al.*, 2018). On one hand, the increased cross continental-shelf CDW transport causes increased basal melt, resulting in ice-shelf thinning and subsequent acceleration, causing the advance of the CFLs. But, on the other hand, increased ice-shelf basal melting may weaken the rheology of the ice shelf, increasing calving and causing CFL retreat. Ultimately, either mechanism would likely result in increased calving, as thinning ice shelves are subject to weakening. The Landsat imagery timeseries does reveal the retreat of some major glacier fronts including Pine Island, Thwaites, Smith and Haynes glaciers, with for example, a portion of the Thwaites Glacier ice front retreating 26 km between 1973 and 2009, and the gradual disintegration of Crosson Ice Shelf since 1984 (MacGregor *et al.*, 2012).

Cyclic calving behaviour of EAIS ice shelves and tongues has been identified on decadal timescales (Kim *et al.*, 2001; Frezzotti and Polizzi, 2002; Miles, 2013; Miles *et al.*, 2016), with a retreating trend between 1972/75 and 1988/95, but with 65% of EAIS glacier fronts advancing at a median rate of 17.9 m yr-1 between 2000 and 2012. Some evidence exists to link these changes to atmospheric and sea-ice conditions (Miles *et al.*, 2016, 2017). However, this is not the case for all EAIS regions, with (Fountain *et al.*, 2017), for example, finding no significant trend in CFLs in Victoria Land between 1955 and 2015, and (Baumhoer *et al.*, 2018) noting explicit exceptions to the overall trend in Victoria Land, Wilkes Land and the northernmost part of Dronning Maud Land. (Lovell *et al.*, 2017)

did find decadal calving trends across Victoria Land, George V Land and Oates Land, but showed that there was no apparent regional spatial trend in CFL change between 1972 and 2013. They did, however, determine that terrestrial-terminating glaciers showed less variation that marine-terminating glaciers, emphasising the importance of the individual glacier response to different climatic, oceanic or ice-dynamical drivers, given their unique geographical setting and conditions (Carr *et al.*, 2013; Lovell *et al.*, 2017). This is illustrated by localised studies of individual calving events, such as (Miles *et al.*, 2017), who attributed two large calving events of Porpoises Bay glaciers, in 2007 and 2016, to the localised breakup and disintegration of multi-year landfast sea ice, driven by anomalous

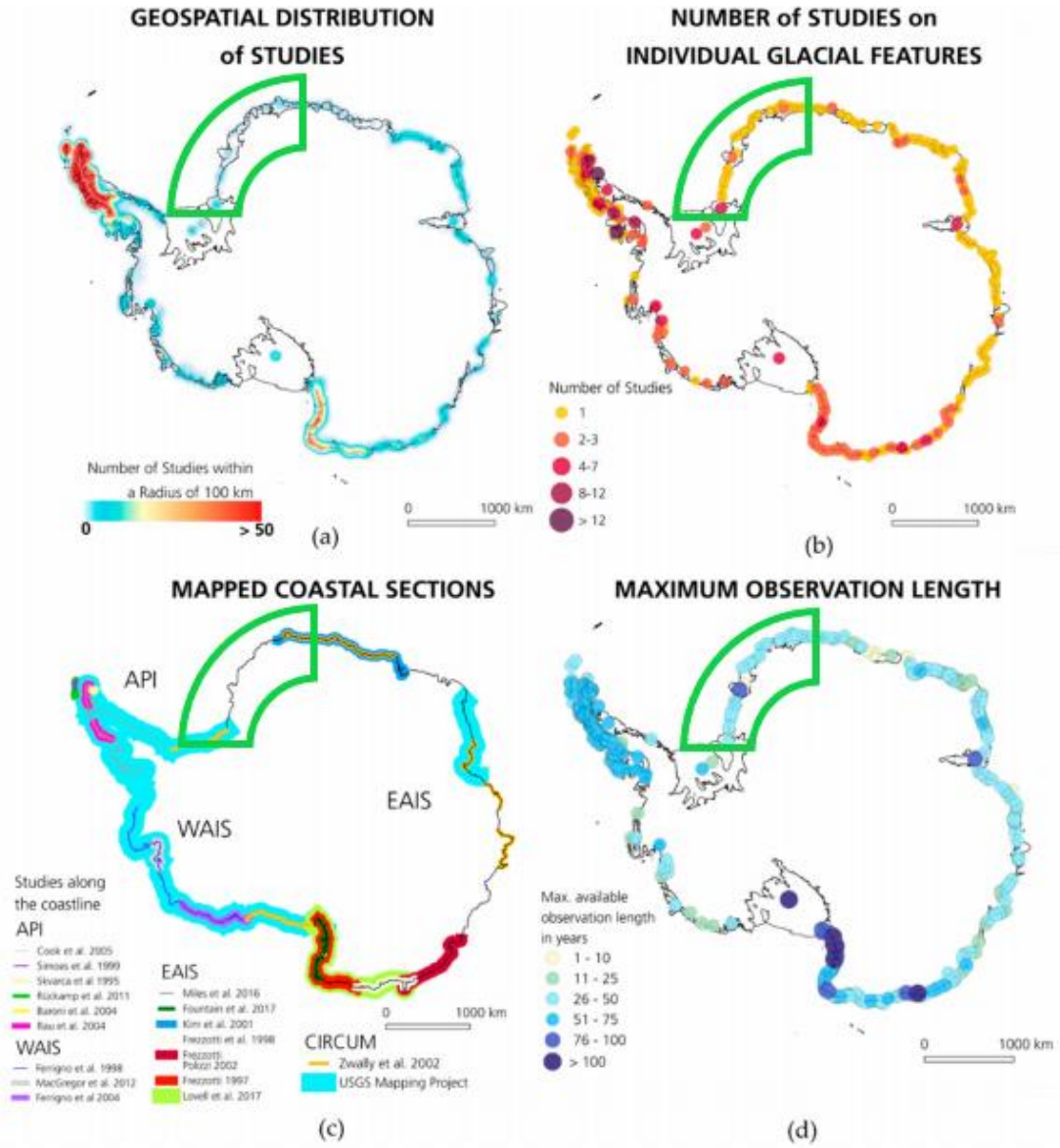

Figure 2.1: Calving front location mapping studies around the Antarctic Ice Sheet, found by a review of the literature by Baumhoer et al. (2018). Maps show (a) the distribution of studies around the AIS, within a 100 km radius; (b) the number of studies on individual glacial features; (c) the coastal sections that have been mapped to date, including the authors; and (d) the maximum observation length in years. The area highlighted in green is the focus of this study (the Eastern Weddell Sea Sector), note that by all measures this region is under-studied compared to other regions, with the only complete mapping of the section by Miles et al. (2016).

API = Antarctic Peninsula Ice Shelves; WAIS = West Antarctic Ice Sheet; EAIS = East Antarctic Ice Sheet.

atmospheric circulation. An early SAR study by Kim *et al.* (2001) found generally retreating CFLs between 1963 and 1975 along the Dronning Maud Land Coast, and circum-Antarctic mapping showing a general trend of advance since then (Patel *et al.*, 2020). Importantly to this thesis, (Baumhoer *et al.*, 2018) noted that the eastern Weddell Sea Sector is amongst the least studied of all the AIS regions, in terms of CFL research (**Error! Not a valid bookmark self-reference.**Figure 2.1).

2.3 Study Location

The geographical focus of this study is an area encompassing the eastern part of the Weddell Sea Sector of the AIS, stretching along the coastline eastwards from the intersection of Ronne Ice Shelf

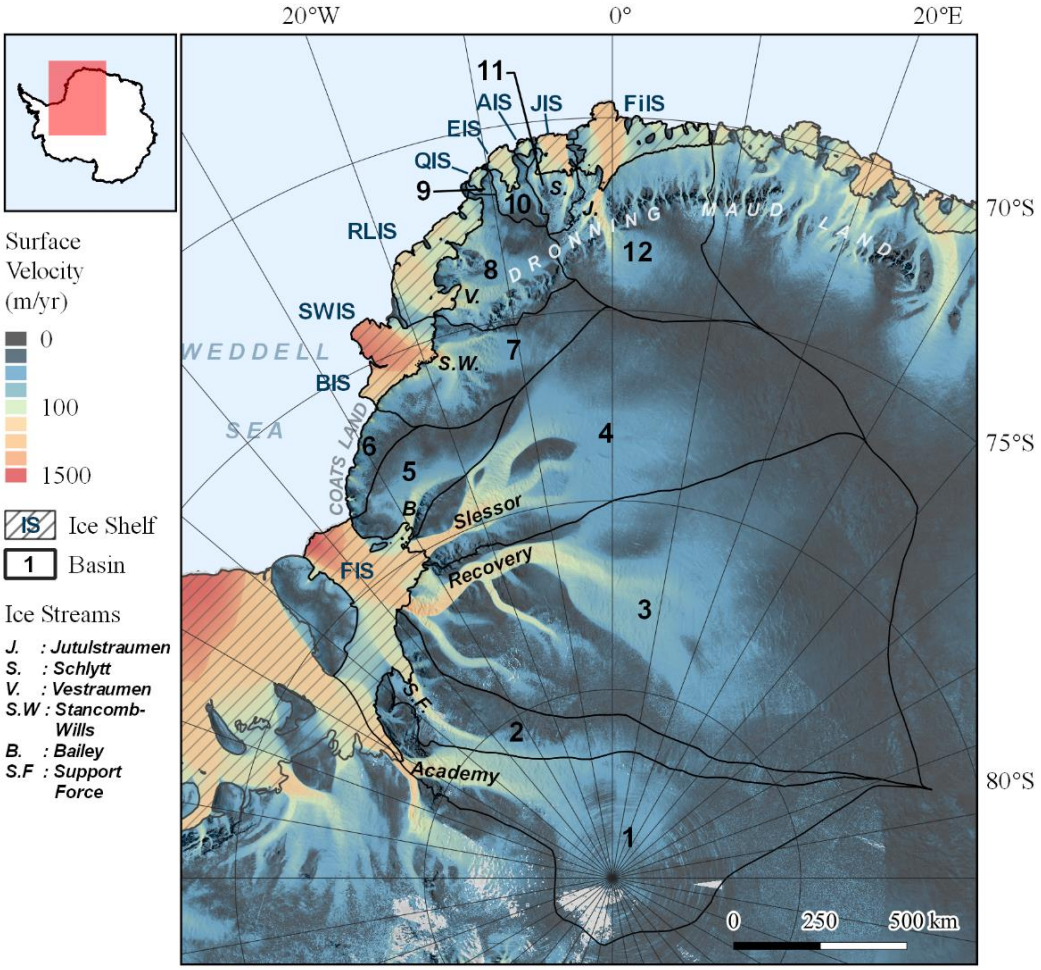

Figure 2.2: The ice shelves (hashed areas) which are the focus of this study and the catchment basins (black lines) from which ice drains through them. Basins 1 to 5 drain through Filchner Ice Shelf (FIS), basin 6 through Coats Land glaciers, basin 7 through Brunt (BIS) and Stancomb-Wills (SWIS) ice shelves, basin 8 through Riiser-Larsen Ice Shelf (RLIS), basin 9 through Quar Ice Shelf, basin 10 through Ekstrøm Ice Shelf (EIS), basin 11 through Jelbart Ice Shelf (JIS) and basin 12 through Fimbul Ice Shelf (FiIS). A minor basin, largely consisting the ice shelf itself, is drained through Atka Ice Shelf (AIS). The ice-sheet surface velocity reveals the network of ice-streams through which ice drains, at speeds of up to 1500 m yr^{-1}, including (north-south) Jutulstraumen Glacier (J.), Schlytt Glacier (S.), Vestraumen Glacier (V.), Stancomb-Wills Glacier (S.W.), Bailey Ice Stream (B.), Slessor Glacier, Recovery Ice Stream, Support Force Glacier (S.F.) and Academy Glacier.

Data Sources: Rignot et al. (2017); SCAR (1992); Zwally et al. (2012).

with Berkner Island (47.7 °W, 77.8 °S), through Coats Land and a portion of Dronning Maud Land to the eastern end of Fimbul Ice Shelf (7.4 °E, 70.3 °S) (Figures 1.1 and 2.2), a distance of approximately 6,000 km. Major ice shelves along this coastline include four out of the ten largest ice shelves in Antarctica, the Filchner, Riiser-Larsen, Fimbul and Brunt/Stancomb-Wills, as well as other major ice shelves (Quar, Ekstrøm, Atka and Jelbart), and several small tongues and ice shelves of marine-terminating glaciers along the Coats Land coastline between the Filchner and Brunt ice shelves (Figure 2.2). These ice shelves have a combined surface area of c. 247,300 km^2, representing c. 37% (16%) of total EAIS (AIS) ice-shelf area (Rignot *et al.*, 2013). Through these ice shelves flow several major ice streams at variable speeds, including the Academy, Support Force, Slessor, Stancomb-Wills, Vestraumen, Schytt and Jutulstraumen Glaciers, and the Foundation, Recovery and Bailey Ice Streams (Figure 2.2), draining a total basin area of c. 2,765,000 km^2, an area c. 27.5% (23%) of the EAIS (AIS) (Zwally *et al.*, 2012).

Ice flows towards the Weddell Sea from the inland, high-elevation regions including the Pensacola Mountains in the hinterland of Filchner Ice Shelf, the Shackleton Range and Theron Mountains in Coats Land and Maudheimvidda and Fimbulheimen in western Dronning Maud Land (Figures 2.2 and 2.3). Nevertheless, c. 36% of the grounded ice within the study area is grounded below sea level, with some stretches of the GL currently sitting on retrograde bed slopes, mainly in the basins

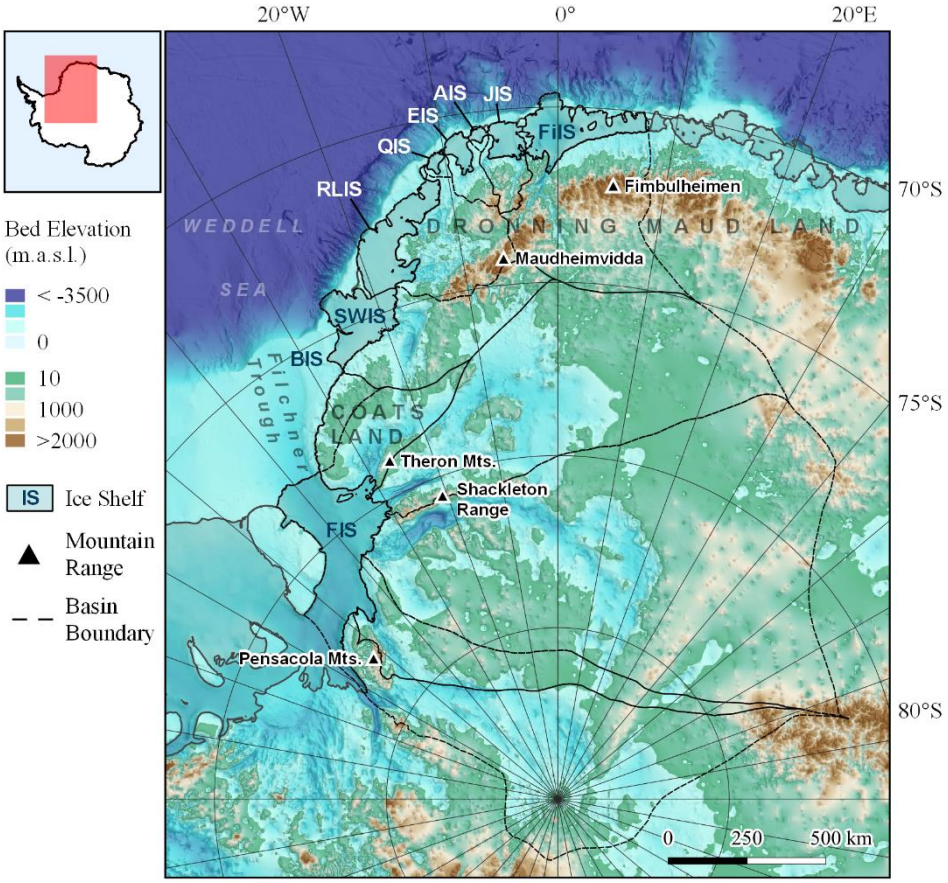

Figure 2.3: The bed elevation of the study region, including major ocean troughs, mountain ranges and the continental shelf. Note the width of the continental shelf in front of the Filchner Ice Shelf (FIS) and other Eastern Weddell Sea ice shelves, as well as the substantial area of the FIS, SWIS and RLIS catchments which lie below present-day sea level.

Data sources: Morlighem et al. (2020); SCAR (1992).

draining into the Filchner Ice Shelf (Zwally *et al.*, 2012; Morlighem *et al.*, 2020), where the GL is as deep as -1,400 m.a.s.l. (Lambrecht *et al.*, 2007). Filchner Ice Shelf's thickness averages 700 m, but is as much as 1800 m at these locations at the deepest GLs (Lambrecht *et al.*, 2007). The continental shelf north of Filchner Ice shelf is c. 450 km wide and on average c. 400 – 500 m deep, with the large cross-shelf bathymetric Filchner Trough stretching from the shelf edge, far into the sub-ice-shelf cavity (Figure 2.3). Along the remaining continental shelf from c. 25°W to c. 0°W, the distance between the ice-shelf front and continental shelf break varies between 0 and 80 km, with sea depths ranging from c. 300 to 400 m.

Within the Weddell Sea, ocean circulation is largely governed by a cyclonic (clockwise) gyre, spanning from the AP at around 40 °E, to Dronning Maud Land (Figure 1.1) in the west (Nicholls *et al.*, 2009). CDW enters the gyre at the northern and eastern edges and is converted to slightly cooler and fresher Warm Deep Water (WDW) as it traverses the continental shelf towards the Fimbul Ice Shelf front (and GL) within the gyre (*ibid*). Therefore, a current of relatively warm, fresh, water flows as a coastal current along the study coastline and continental-shelf break in a broadly north-south direction.

2.4 Glaciological Change in the Eastern Weddell Sea

Ice-sheet reconstructions since the Last Glacial Maximum (LGM) are limited by a lack of marine and terrestrial sedimentary, geological and bathymetric data, when compared to other regions of the AIS (Hillenbrand *et al.*, 2014; Siegert *et al.*, 2019). However, marine-geological evidence that meltwater pulses of a few meters originated here since the LGM, indicate that the scale of glacial change in the region has been relatively large during, and since, the LGM (Bentley *et al.*, 2010; Hillenbrand *et al.*, 2012, 2014). This is in agreement with terrestrial surface exposure-age dating which infers limited ice-sheet thickening of 230 – 480 m above present day in the Ellsworth Mountains in Ellsworth Land (Figure 1.1) and near-zero thickening in the Shackleton Range (Figure 2.3) during the LGM (Bentley *et al.*, 2010; Le Brocq *et al.*, 2011). Since the LGM, glacial areal extent has episodically decreased, although there is disagreement as to the exact rate and regime of retreat. Marine evidence for GL locations in close proximity to the continental shelf edge, up to c. 300 km north of the contemporary CFL at Filchner Ice Shelf (Bentley and Anderson, 1998; Bentley *et al.*, 2010), is constrained by dating uncertainties and therefore, may originate earlier in the Quaternary rather than the LGM, but studies do agree that GLs had retreated to the inner continental shelf by c. 10 – 15 cal ka BP and were close to their contemporary positions by c. 5 cal ka BP (Hillenbrand *et al.*, 2012; Larter *et al.*, 2012; Stolldorf *et al.*, 2012). Evidence indicates that retreat was diachronous (Stolldorf *et al.*, 2012; Hillenbrand *et al.*, 2014; Sørli, 2016), with more recent (since 5 cal ka BP) retreat largely governed by thinning ice shelves,

as opposed to iceberg calving, and complicated by slight re-advance of several ice shelves as they became pinned on local bed rises (Hodgson *et al.*, 2018).

Since early satellite investigations from 1963, CFLs in the study area have followed approximately the same trend as the rest of the EAIS, retreating on decadal timescales between 1963/72/75 and 1988/95, but with more variation on sub-decadal timescales (e.g. Lange and Kohnen, 1985), before switching to broadscale advances between 2000/01 and 2009/2015 (Kim *et al.*, 2001; Miles *et al.*, 2016; Baumhoer *et al.*, 2018). Satellite radar altimetry has, likewise, found ice shelves within the study region to be gaining net volume between 1994 and 2012. An example comes from the Filchner, Brunt and Fimbul ice shelves, which thickened at an average rate of 1.5 ± 0.5, 2.6 ± 1.2 and 3.2 ± 1.1 m decade^{-1}, respectively, although this trend has decelerated since 2000 (Paolo *et al.*, 2015). Only insignificant (<10 m yr^{-1}) advance or retreat of study-area GLs have been reported over the last few decades (Konrad *et al.*, 2018) and, in contrast to other regions of the AIS, glaciers are in approximate mass balance (Rignot *et al.*, 2019). A recent unusual net mass gain across Dronning Maud Land between 2011 and 2014 was found to be due to an anomalous large-scale accumulation event (Helm *et al.*, 2014). The majority of mass loss from ice shelves in the study region is due to calving (c. 154 Gt yr^{-1}) as opposed to basal melt (c. 79 Gt yr^{-1}), with surface melt, as with the majority of EAIS ice shelves, practically non-existent (Rignot *et al.*, 2013). In fact, basal melt rates were modelled at just 0.67 – 1.67 m yr^{-1} at Brunt and Riiser-Larsen ice shelves (Thoma *et al.*, 2006) and basal marine-ice accretion is occurring beneath much of Filchner Ice Shelf, away from the ice front (Oerter *et al.*, 1992; Joughin and Padman, 2003).

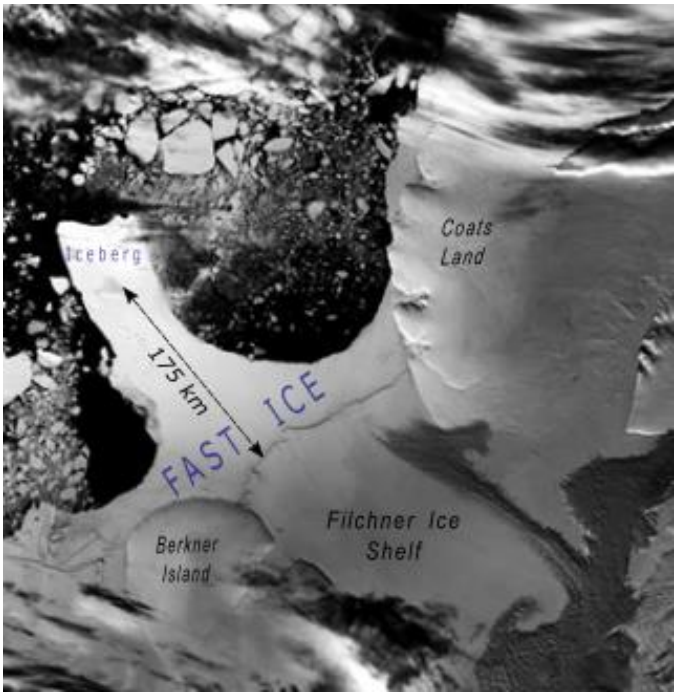

Figure 2.4: Advanced Very-High-Resolution Radiometer (AVHRR) visible image of the Filchner Ice Shelf front on the 13th December 2000. Landfast sea ice (fast ice) can be seen connecting the ice-shelf front and coasts of Berkner Island and Coats Land to a large iceberg which became grounded on the continental shelf, c. 175 km in front of Filchner calving ice front.

Adapted from Scambos (1996).

Iceberg calving is a particularly significant process at Filchner and the other giant, 'cold water' ice shelves (Ross and Ronne), as they only account for 15% of total AIS basal melting but occupy two-thirds of the AIS ice-shelf area. (Wuite *et al.*, 2019) quantified the calving rate as Filchner Ice Shelf at 9 ± 1 Gt yr^{-1} between 2011 and 2017, which equates to 10% of the steady-state calving flux,

demonstrating the importance of major calving events in regulating the CFL and calving flux of Filchner Ice Shelf. Major calving events at Filchner Ice Shelf have in the past led to the stabilisation and build-up of multiyear fast ice at the ice front, which some have argued increases the stability of the ice front (e.g. Khazendar *et al.*, 2009; Massom *et al.*, 2010) (Figure 2.4). For example, a major calving event in 1986 left three icebergs grounded at Berkner Bank, resulting in an accumulation of fast ice stretching back to the CFL (Nicholls *et al.*, 2009). (Rignot and MacAyeal, 1998) theorise that climate change could lead to a weakening of fast ice and, therefore, Filchner Ice Shelf could release widespread tabular icebergs over annual to decadal timescales, leading to possible disintegration. At present, the Filchner ice front is advancing (Patel *et al.*, 2020) and monitoring for the next major calving event should be prioritised.

The Brunt/Stancomb-Wills ice shelf system is similarly in a state of advance (Miles *et al.*, 2016; Patel *et al.*, 2020). What is particularly interesting about this ice shelf is its unique rheological composition which consists of the Brunt and Stancomb-Wills ice shelves connected by a visible expanse of ice melange, comprising 20 – 30% of the area of the system (Thomas, 1973; Hulbe *et al.*, 2005; Khazendar *et al.*, 2009). Due to the process of formation of this ice melange, which is composed of marine ice, sea ice, ice-shelf debris and firn, the Brunt/Stancomb-Will Ice shelf system is particularly vulnerable to relatively small warm anomalies in ocean temperatures. This is further accentuated because its unique composition includes marine ice which is porous up to c. 100m from its base and thus, more susceptible to oceanic basal melting (Craven *et al.*, 2005; Khazendar *et al.*, 2009). It is hypothesised that acceleration of the system in the 1970s was due to a weakening in the ice melange, probably as a result of oceanic convection or changing oceanic circulation bringing deep water to the surface (Holland, 2001; Khazendar *et al.*, 2009; Nicholls *et al.*, 2009).

The last major recorded calving event at Brunt Ice Shelf was in 1971, with previous calving at some point between 1915 and 1955, denoting that the contemporary ice front is now advanced beyond its maximum extent prior to previous calving, as is the Stancomb-Wills ice front (from mapping by Worsely, 1921) (Anderson *et al.*, 2014). However, contemporary ice-shelf collapse, similar to that seen along the AP, seems unlikely at Brunt Ice Shelf given its unique rheology and the fact that there is minimal surface melt in this part of the AIS (Anderson *et al.*, 2014). Nonetheless, the Brunt/Stancomb-Wills system may be subject to an imminent major calving event given that a significant (c. 70 km in 2019) rift has opened up between the two ice shelves, likely to eventually lead to decoupling of their flow regimes (Khazendar *et al.*, 2009; Anderson *et al.*, 2014). In fact, recent rifting since 2012 and the threat of calving at Brunt Ice Shelf has meant that the British Antarctic Survey has stopped overwintering at the Halley Research Station since 2017 (De Rydt *et al.*, 2018, 2019; Rose,

2019) and it is possible that a calving event at Stancomb-Wills Ice Shelf could directly lead to instability at Brunt Ice Shelf by iceberg collision (Anderson *et al.*, 2014).

Because the flow of the almost-stagnant neighbouring Riiser-Larsen Ice Shelf is subject to the "pull" of Stancomb-Wills through mechanical coupling of their flow, any changes to the flow of the Brunt/Stancomb-Wills system could propagate hundreds of kilometres along the coast (Khazendar *et al.*, 2009). Further north, the Fimbul Ice Shelf is characterised by the Jutulstraumen glacier tongue which extends for c. 50 km (2019) in front of the rest of the ice front. A major calving of this ice tongue in 1967 yielded a single iceberg "Trolltunga" with dimensions 53 by 104 km, which would have taken a minimum estimated time of 100 years to form (Swithinbank, 1988).

Ocean modelling has identified how the ice-shelves north of Brunt Ice Shelf may be more vulnerable to basal oceanic melt, due to the relatively narrow continental shelf (Figure 2.3) which warmers waters can more rapidly traverse, compared to Filchner where the front is c. 400km from the continental shelf break and the GL up to c. 500 km beyond that; it therefore, only has relatively cold waters accessing the ice front and GL (Nicholls *et al.*, 2009). However, bathymetric research at Ekstrøm, Atka, Jelbart and Fimbul ice shelves has revealed how their fronts are pinned on local bed rises and, thus, access for relatively warm water to the GLs is limited and restricted to basal melting near the ice CFL. Overall, the highest ice-shelf basal melt rates are likely to occur near the ice fronts, fundamentally altering their mechanical strengths and thus possibly increasing calving (Thoma *et al.*, 2006), but with some basal melt expected at the GLs where bed morphology is more favourable, such as at the GLs of Stancomb-Wills and Vestraumen glaciers. Because of the oceanographic significance of ice shelves in driving the Weddell Sea Gyre by the modification of water masses due to the input of relatively cool freshwater, modelling indicates that if the Brunt/Stancomb-Wills/Riisner-Larsen Ice Shelf system were removed, basal melting at the Fichner-Ronne Ice Shelf would increase by c. 7% (Thoma *et al.*, 2006). Whilst this is an unlikely scenario, it does reemphasise the importance of ice-ocean-atmosphere interactions in glaciological change in the region.

3 Methods

A c. 6000 km (5750 to 6400 km between 2009 and 2019) coastline stretch consisting of calving fronts and island coastlines, in the Eastern Weddell Sea Sector, was delineated for several years between 2009 and 2019 by the batch processing of 269 georeferenced optical (182) and radar (87) satellite images and the use of manual and semi-automatic GIS techniques, as outlined below (Figure 3.1). Additional datasets have been used to extend the CFL and ice-shelf area timeseries back beyond 2009, facilitating analysis of the ice-ocean-atmosphere interactions driving CFL change in the region.

3.1 Datasets

Radar and optical satellite imagery acquired during austral summer for the years[1] 2009, 2011, 2013, 2015, 2017 and 2019 was downloaded and processed so that ice fronts could be manually or semi-automatically delineated. Previously published CFL datasets were used to extend the timeseries of temporal ice-shelf area change back into the 1960s (Miles *et al.*, 2016); Haran, 2018, 2005). This section summarises the datasets used.

3.1.1 Radar Instruments

ESA's Sentinel-1A and Sentinel-1B, launched in 2014 and 2016, respectively, are satellite platforms for C-band (5.4 GHz/5.6 cm) synthetic aperture radar (SAR) instruments (Torres *et al.*, 2012). Because they are placed on the same orbit, 6 days apart, the mission has a scene revisit time of 6 days, allowing for, in glaciological terms, high-temporal resolution imagery. Image acquisition is either in the Interferometric Wide Swath (IW) or Extra Wide Swath (EW) mode, with single HH polarization, using the Progressive Scans SAR (TOPSAR) technique. IW imagery has a 250 km swath at a 10 m spatial resolution, compared to EW imagery which has a 410 km swath and 40 m spatial resolution.

Sentinel-1 data were selected for use in this CFL mapping study due to the open-access data availability, their medium spatial and temporal resolution imagery which is suitable for the scale of ice shelves being studied, and because acquisitions are not affected by cloud cover or darkness. Furthermore, the fact that radar data offer higher contrast between snow, glacial ice and sea ice than optical imagery makes it easier to correctly identify the CFLs, as discussed in sections 2.2.1. and 2.2.2. Nonetheless, Sentinel-1 image availability is limited to 40 m-resolution EW scenes for the study area between 2014 and 2016 and, clearly, given the satellite launch dates, Sentinel-1 data is not available prior to 2014. Therefore, Sentinel-1 Ground Range Detected (GRD) Level-1 radar imagery was

[1] Unless otherwise stated, data relates to the austral summer that consists the start of the stated year and the end of the preceding year. E.g. "2009" denotes austral summer 2008/09.

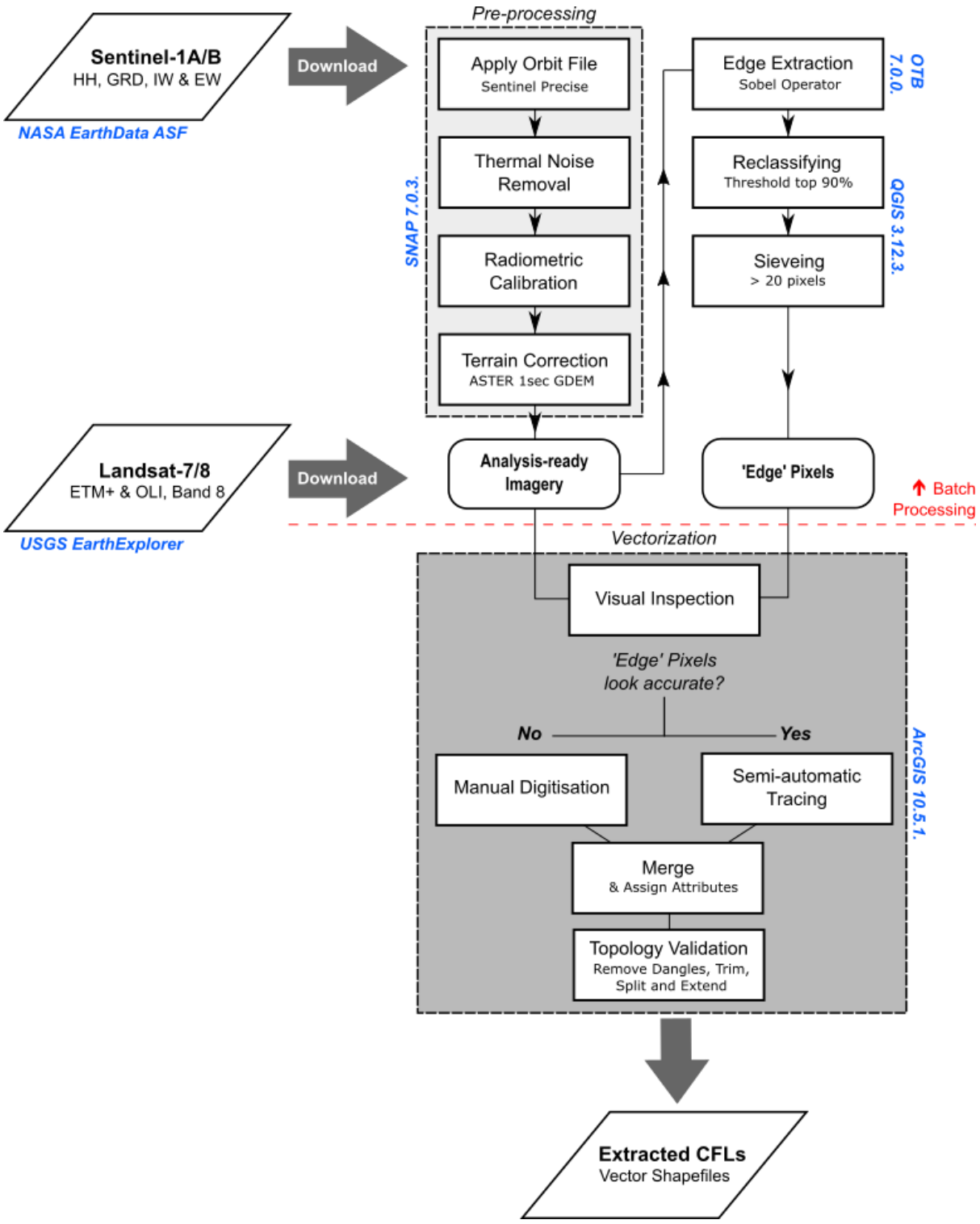

Figure 3.1: The CFL mapping methodology, from download through to finished CFL vector shapefile product. Items highlighted in blue show the data source or software used in a given step. NASA EarthData ASF = NASA Alaska Satellite Facility, SNAP = Sentinel Application Toolbox, OTB = Orfeo Toolbox (Grizonnet et al., 2017), QGIS = Quantum GIS, ArcGIS = ESRI ArcMAP. All processing above the red line was undertaken using batch processing scripts.

downloaded from the NASA Alaska Satellite Facility (Copernicus Sentinel data, 2020), for the years 2015, 2017 and 2019 only, with preference for IW scenes where available, due to the higher spatial resolution. Raw multi-look intensity data scenes were pre-processed using standard techniques involving the application of the Sentinel Precise Orbit file, thermal noise removal, radiometric

calibration and terrain correction (Lu and Veci, 2016) using the European Space Agency's (ESA) Sentinel Application Toolbox (SNAP) software (v.7.0.3.) ("Pre-processing" in Figure 3.1). The ASTER 1sec GDEM was used to perform terrain correction, which is applied to remove geometric distortions due to the SAR side-looking geometry and terrain.

3.1.2 Optical Instruments

The Landsat-7 and Landsat-8 satellites were launched in 1999 and 2013, respectively, continuing the USGS/NASA Landsat series of satellites which have been in orbit since 1972. The Landsat satellite mission was chosen for inclusion in this CFL study due to its openly accessible medium-resolution imagery, captured on a 16-day repeat cycle at a medium scene-size of 185 km by 180 km, although preference was towards using Sentinel-1 data when available (post-2014) due to the better differentiation between surfaces (sea ice/ice shelf) and because persistent cloud-cover is common over the EWS ice shelves. Enhanced Thematic Mapper Plus (ETM+; Landsat-7) and Operational Land Imager (OLI; Landsat-8) optical satellite imagery captured during austral summer was downloaded from the US Geological Survey Earth Explorer (USGS, 2020) for the entire study area for 2009, 2011 and 2013 (Landsat-7), and for lengths of the coast not covered by Sentinel-1 radar data in the years 2015, 2017 and 2019 (Landsat-8), or where uncertainties in distinguishing the CFL from Sentinel-1 data existed. Where possible, scenes with the lowest percentage cloud-cover were selected and when a choice of cloud-free imagery was available, the image acquired closest to mid-January was used to minimise the effects of seasonal calving cycles on the annual data. Band 8 (panchromatic) images, spanning wavelengths of 0.52 to 0.90 µm (Landsat-7) and 0.50 – 0.68 µm (Landsat-8), were utilised for coastline delineation due to their higher spatial resolution when compared to other bands, at 15 m by 15 m. This product is provided geocoded by the USGS in Polar Stereographic coordinates.

Where possible, only the centre portions of Landsat 7 scenes were used, due to the approximate 22% data loss towards the scene edges caused by the failure of the Scan Line Corrector in 2003 (Chen *et al.*, 2011). Where this was not possible, neighbouring scenes were used to interpolate across the data gaps (c. 90% of data gaps), with linear interpolation across any remaining data gaps (c. 10%). The method used for each scene is marked in the accompanying notes in the shapefile metadata and the maximum interpolation over any one data gap was c. 350 m.

The Declassified Intelligence Satellite Photographs (DISP), used here to extend the CFL and ice-shelf area timeseries back to the 1963, were taken by a series of polar-orbiting reconnaissance satellites launched in the early 1960s, called Corona, Lanyard and Argon. The Antarctic data imagery was collected as part of the Argon program, which was operational from 1961 to 1964 and mosaiced into an Antarctic coastline product for the year 1963 by Kim *et al.* (2007). This imagery was captured

using the single, vertically oriented, panchromatic frame camera at a focal length of 76.2 mm, resulting in comparatively low spatial resolution imagery, at a pixel-equivalent resolution of 140 m.

3.1.3 Previously Delineated Calving Front Locations

Previous coastline datasets for the years 1974, 1990, 2000, 2012 (Miles *et al.*, 2013, 2016), 2004 (Haran, 2005) and 2014 (Haran, 2018) have been used to extend the CFL and ice-shelf area measurements back in time.

The CLFs digitised by Miles *et al.* (Miles *et al.*, 2013, 2016) are from Landsat imagery and are therefore subject to similar manual CFL delineation methods and uncertainty as discussed herein, specifically the 2000 and 2012 datasets which were digitised from Landsat 7 (ETM+) imagery. Landsat-4 and Landsat-5 Thematic Mapper (TM) imagery was used for mapping the 1990 CFLs and the Multispectral Scanner (MSS) instrument was used for 1974 mapping. It should be noted that the satellite imagery used was acquired across a number of years due to cloud-cover in some scenes. Specifically, the 1974 CFLs were digitised from imagery acquired between 1972 and 1975, 1990 CFLs from 1988 to 1991, 2000 CFLs from 1999 to 2002 and 2010 CFLs from 2009 to 2012. Due to the varying spatial resolution of the sensors used, (Miles *et al.*, 2013) estimate that maximum errors associated with their measurements (Table 3.1), which are used in this study when making comparisons against these data.

CFL/coastline dataset	Digitised from	Estimated error (m)
1974	Landsat MSS	± 210
1990	Landsat TM	± 185
2000	Landsat ETM+	± 75
2004	MODIS	± 250
2012	Landsat ETM+	± 75
2014	MODIS	± 250

Table 3.1: The existing CFL/coastline datasets used to extend the timeseries backwards, the satellite/sensors used to create the product and the estimated error. The 1974, 1990, 2000 and 2012 products were produced by Miles et al. (2013) and the 2004 and 2014 products produced by Haran et al. (2005; 2018).

The 2004 and 2014 CFLs were extracted from circum-Antarctic coastline maps delineated from digital image mosaics acquired by the MODerate-resolution Imaging Spectroradiometer (MODIS) satellite, between November and March in 2003/04 and 2013/14, respectively. MODIS imagery has a comparatively coarse spatial resolution of 250 m. Therefore, the estimated error of the coastline products used is stated by their authors to be 250 m (Haran, 2005, 2012) (Table 3.1). However, due to the relatively coarse spatial resolution, the ice shelf areas calculated for 2004 and 2014 are likely to be an overrepresentation of the actual area compared to those presented in this study, as rifts, crevasses and other coastal details will inevitably have been omitted. This is also likely true for the

1974, 1990, 2000 and 2012 coastlines, as they were also mapped at a coarser viewing scale than the 1:30,000 used in this study, although to a lesser extent due to the higher resolution of Landsat imagery when compared to MODIS imagery.

3.2 Coastline Delineation

A combination of manual and semi-automatic techniques were used to digitise CFLs and associated edges from satellite imagery, which were extracted using a modified edge extraction algorithm (Figures 3.1 and 3.2). In total, 269 georeferenced Landsat-7 ETM+ (147), Landsat-8 OLI (35), Sentinel-1 IW (54) and Sentinel-1 EW (33) images were used to delineate the CFLs and coastline (Table 3.2).

Year	Landsat-7 ETM+	Landsat-8 OLI	Sentinel-1 EW	Sentinel-1 IW
2009	15.9%			
2011	16.0%			
2013	16.4%			
2015		6.6%	10.1%	
2017		5.2%		12.1%
2019		5.4%		12.4%
Total	48.4%	18.77%	10.1%	24.5%

Table 3.2: The percentage of the length of CFLs/coastline delineated from each sensor/satellite type, for each year.

A Sobel edge extraction algorithm was used to detect edges in all satellite imagery, both optical and pre-processed SAR, using the opensource Orfeo Toolbox software package (v.7.0.0.) (Grizonnet *et al.*, 2017), which was developed by the French Space Agency for the analysis of satellite imagery and is available as a QGIS plugin. The Sobel operator estimates the derivative of brightness changes over horizontal space by convolving a 3 by 3 pixel kernel with the image and then a threshold is used to classify pixels as "edge" pixels (Seal *et al.*, 2011). Here, additional steps were applied in a modified Sobel-operator method, to remove misclassified edges and noise, and to make the data suitable for vectorising using the ArcMap Trace tool: (1) Since this algorithm assigns identified "edge" pixels a value based on the probability of being an edge, pixels output from this algorithm with a value in the lowest 10^{th} percentile were removed, and all remaining pixels reclassified as 1 (i.e. 1 = "Edge", 0 = "Not Edge") ("Reclassifying" in Figure 3.1; Step 2 in Figure 3.2); and (2) Because edges in images are manifested as lines of connected "edge" pixels (i.e . "edge" pixel islands of a given area), a sieving algorithm was used to remove "edge" pixel clusters of less than 20 pixels in area ("Sieving" in Figure 3.1; Step 3 in Figure 3.2). Both thresholds were selected based on trial runs using five of each image type (Landsat optical, Sentinel-1 IW and Sentinel-1 EW) which produced adequate edges to be clearly visible to the naked eye (Figures 3.2 and 3.3). Although a sensor-specific and locally-adaptive thresholding method may have yielded more precise results, the development of such an algorithm

would have been time expensive, particularly given that the vectorization stage was subject to manual checks on the identified edges, regardless.

The resulting Edge Extracted images were used in conjunction with the processed satellite imagery, during manual delineation of ice fronts, so that manual decisions could be made as to the accuracy of the edge detection output along each section of coastline ("Vectorization" stage in Figure 3.1; Figure 3.3). For instance, edges may have been correctly identified, but may in fact be the edge of the sea ice (i.e. the boundary between sea ice and ocean surface), as opposed to the CFL. In this way, areas where the "edge" pixels were deemed to have been accurately identified as the ice front/coastline from visual inspection, the ESRI ArcMap (v.10.5.1.) ArcScan Trace tool was used to

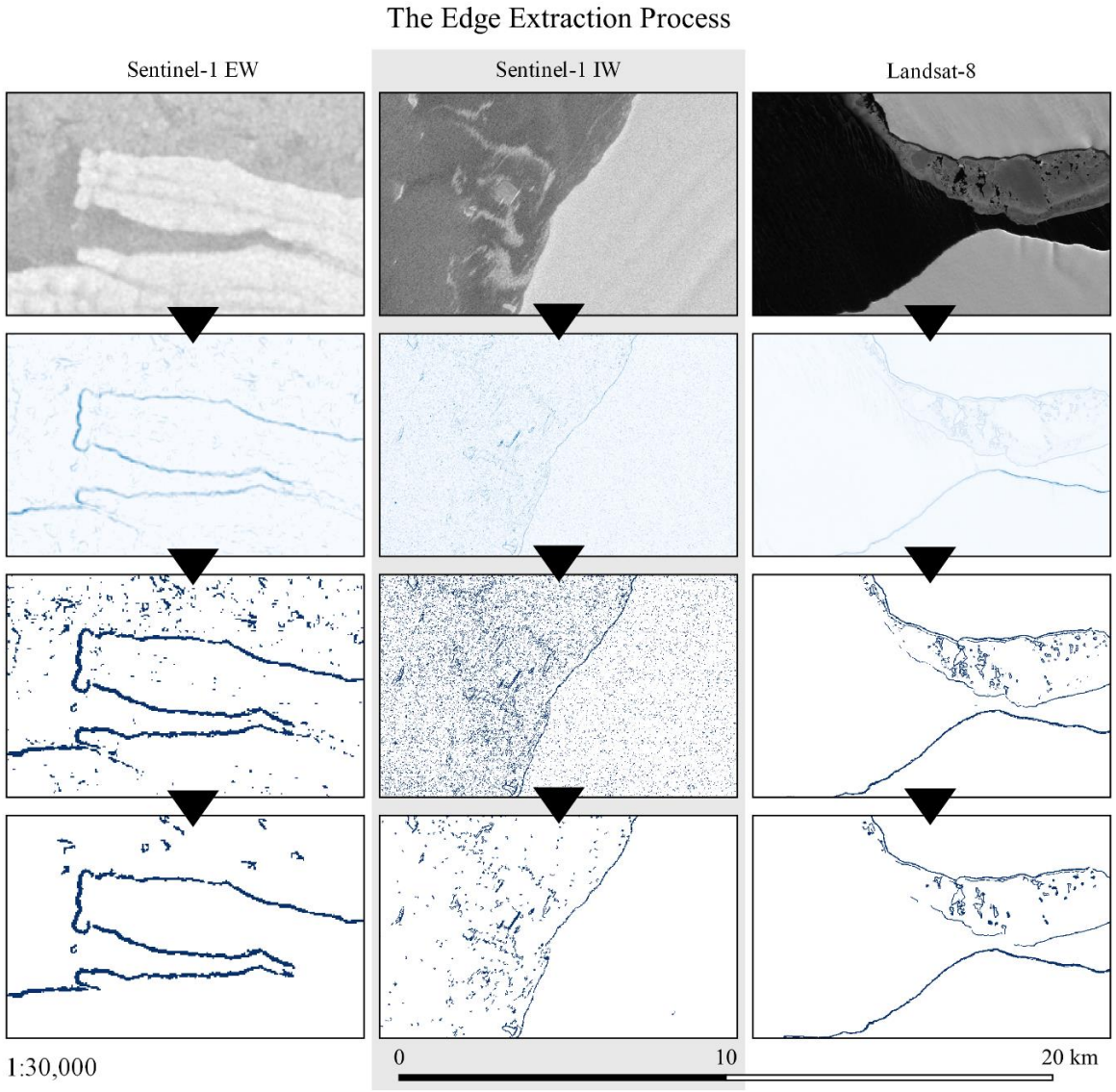

Figure 3.2: Example runs of the modified Sobel edge detection operator (Step 1), followed by reclassifying of pixels outside 90th percentile (Step 2) and sieving pixel clusters of less than 20 pixels (Step 3). The end result, irrespective of the source satellite/sensor is a continuous row of "edge" pixels which, under manual supervision, can be digitised at the CFL. Images are shown at the minimum scale used whilst digitising (1:30,000) to give an idea of what edge extracted layers looked like during the vectorization stage.

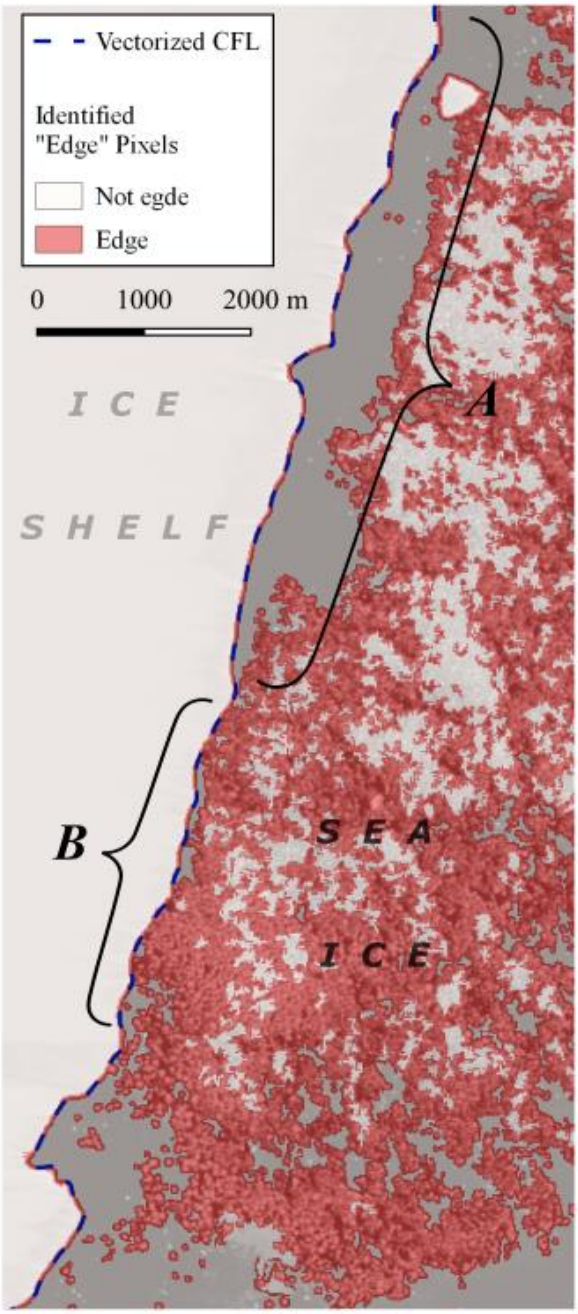

Figure 3.3: Example of the hybrid CFL vectorization method from a Landsat-8 OLI image. The output of the edge extraction algorithm (after thresholding and sieving) is superimposed on the original satellite image, so that a decision as to the accuracy of the algorithm could be made. In areas where "edge" pixels appear to be accurate (A), they were mapped using ArcMap Trace Tool, whereas in areas where the edge detection algorithm was unable to classify the edge (B), manual delineation was used. In this example, an area of sea ice caused the edge extraction algorithm to cluster a large group of pixels together, falsely identifying them as "edge" pixels. Because it is simple to toggle between manual and semi-automatic tracing, a combination of both techniques was used in parallel to vectorize the CFLs. Imagery date: 24/01/2017; path: 170; frame:110; courtesy of the USGS.

quickly and efficiently vectorize the coastline, snapping to the centre of the raster line pixels using manually optimised parameters (Appendix VII).

All other lengths of coastline were digitised manually using the ArcMap vector editing tools in stream mode and toggling between "edge" pixel tracing and manual delineation in areas where identified edges were discontinuous (Figure 3.3). Since toggling between manual digitising and tracing of "edge" pixels is used, the overall digitising strategy can be considered a hybrid, or "manual plus", approach which is both quicker and more accurate than exclusively manual mapping (see Section 2.2.3.). Of the scenes where the edge extraction algorithm was deployed about 48% of mapped CFLs were identified using tracing of "edge" pixels and about 52% were mapped using exclusively manual techniques.

All digitising, whether exclusively manual, or semi-automatic, was undertaken at a viewing scale of 1:30,000 or higher and traditional image manipulation techniques such as brightness, contrast, and histogram adjustments were used to decrease the digitising uncertainty where necessary. As discussed in Section 2.2., even with image manipulation techniques, CFL delineation can nevertheless be subjective, and, as such, in areas of uncertainty, the previous CFL/coastline data products in Table 3.1, from Antarctic Digital Database and satellite imagery from Google Earth were consulted to validate and constrain CFLs. Even so, some areas

of uncertainty remain, such as at the shear margins of Stancomb-Wills Ice Shelf for example, and therefore, a qualitative quality flag between 1 and 3 was assigned to each digitised line segment (Table 3.3), with a total 61.8%, 37.1% and 1.1% of the total length of digitised CFLs being flagged *1*, *2* and *3*, respectively, where *1* is the highest quality. Digitised coastlines were checked for topological errors and cleaned using a combination of Snap, Extend and Trim tools in ArcMap to remove line dangles, intersects and overlaps, and to ensure the topological integrity of the data ("Topology Validation" in Figure 3.1). Snapping tolerances of these tools was set to no greater than the source-image spatial resolution, to avoid introducing additional error. Once data cleaning was complete, attribute tables were finalised to ensure each line segment contained the appropriate metadata so that the lines may be used in future glaciological or cartographical research (Table 3.4 and Appendix I).

Quality Flag	Description	Length of digitised CFLs
1	*CFL is clear to distinguish in the satellite image, which is at a high resolution (i.e. Landsat-8 Band 8 or Sentinel-1 IW). No, or very minimal cloud cover which does not obscure the view of the CFL. The ice shelf is clearly not sea ice.*	61.8% (22,323 km)
2	*CFL may be subjective, or digitised from lower resolution imagery (i.e. Sentinel-1 EW). Scene may have some cloud cover which obscures short lengths of the coastline or makes it difficult to distinguish between sea ice and ice shelf. Crevassing and/or rifting may cause some uncertainty, particularly around ice-shelf edges and shear margins.*	37.1% (13,397 km)
3	*Moderate lengths of the digitised CFL are uncertain and likely to be subject to higher error. This may be due to cloud cover, where no other satellite imagery was available to cross-check, or uncertainty distinguishing ice shelf from sea ice because of, for example, snow-cover (Landsat) or similar intensity returns (Sentinel).*	1.1% (4,030 km)
Not Digitised	*Significant lengths of CFL cannot be distinguished in all available datasets and therefore, cannot be digitised.*	N/A

Table 3.3 : The quality flag assigned to digitised CFL/coastline sections and the percentage (length) of the total length of digitised CFLs which were assigned each quality flag.

The 1963 CFLs were manually delineated from the DISP mosaic in much the same way as for manually delineated sections of the 2009 to 2019 datasets; however, this was limited by the relatively low spatial resolution of the imagery and by the high proportion of cloud cover. Digitisation for this dataset was at a viewing scale of approximately 1:200,000 and was undertaken in collaboration with colleagues at the Scott Polar Research Institute. Cloud cover proved prohibitive to delineating the CFLs of Brunt and Stancomb-Wills Ice Shelves, as well as several smaller Coats Land coast glacier tongues. Moreover, thick cloud cover in the DISP image mosaic over c. 1200 km^2 of the Jultulstraumen ice

tongue in the central Fimbul Ice Shelf, and c. 25% of the CFL at the eastern end of the Filchner Ice Shelf, meant that these areas could not be mapped to a high level of certainty. Instead, to extract the approximate CFLs, upper and lower bound "best guess" CFLs were delineated, constrained by what was visible through the cloud, and in the case of the Jutulstraumen Ice Tongue, by published literature on the extent of the Trolltunga Ice Shelf which calved from here in 1967 (Birkenmajer *et al.*, 1980). In this way, the areas of these ice shelves are subject to relatively large uncertainty (see Section 3.6.) but are nonetheless useful in understanding the magnitude of changes which have occurred at these ice shelves.

Metadata	**Description**
Platform	*The satellite platform from which imagery was captured and the segment was digitised i.e. Landsat-7/8 or Sentinel-1a/b.*
Sensor	*The sensor which captured the imagery from which the segment was digitised i.e. OLI/ETM+.*
Qual_flag1	*Quality flag (See Table 3.3).*
AUTH_ID	*Digitiser's initials*
Sector	*The sector of coastline to which the line segment belongs e.g. 'Fimbul Ice Shelf' or 'Berkner Island'.*
Notes	*Any note about the digitising process which are relevant to using the product e.g. if there were any areas of uncertainty due to cloud or snow cover, or if semi-automatic edge detection processes were used to digitise that given line segment.*
Year	*Year that the CFL was in the digitised position.*
Descrip.	*This contains the Landsat/Sentinal imagery filename from which the CFL was digitised. Includes the absolute satellite path and frame of the satellite image and the datetime that it was captured.*

Table 3.4: Metadata recorded in the attribute table of the digitised CFLs (Appendix I).

3.3 Ice Shelf Areas

Ice shelf names and dividing boundaries in the study region (if different from the GL) were identified from the SCAR Gazetteer (SCAR Secretariat, 1992) and the NSIDC MEaSUREs Antarctic Boundaries dataset (Mouginot *et al.*, 2017), respectively. For one small (< 3 km^2) identified ice tongue at 76.5°S, 29.5°W, no name was recorded in the SCAR Gazetteer and it has therefore been named "Glacier 1" for the purposes of this study. The delineated coastlines from this study, and the existing CFL data products, were joined with the Scripps Institute of Oceanography GL (Depoorter *et al.*, 2013a) and NSIDC ice-shelf boundaries (Mouginot *et al.*, 2017), to produce ice-shelf polygons for each of the years where data exists (1963 – 2019), similar to the method of Cook and Vaughan (2010). The point at which CFLs and GLs were joined was taken to be their innermost crossing point (i.e. the first crossing

point when travelling from the centre of the ice-shelf front, outwards). Ice shelf areas were then calculated in the Polar Stereographic Projection, excluding areas of grounded ice (islands and ice rises in Mouginot *et al.*, 2017) that fall within the ice-shelf area. Where CFLs were incomplete for a given ice shelf, ice shelf polygons were not created and, therefore, measurements of these ice-shelf areas do not exist. However, this is the case for only a limited number of ice shelves in 1963 and 1974 (Appendix II), and the sections of coastline which have been mapped for these areas are nonetheless useful for making qualitative comparisons and are thus included in the produced maps.

Whilst the GL locations will have undoubtedly changed during the study period, use of a fixed GL allows the ice shelf area to be used as a direct proxy for CFL change, thus facilitating CFL change quantification. Therefore, although the ice-shelf areas presented here may not represent the exact area of floating ice, this study is mainly concerned with area trends and the underlying drivers acting to change the CFLs. Additionally, the Brunt/Stancomb-Wills ice shelf system was separated into the separate Brunt and Stancomb-Wills ice shelves for analysis, by visual inspection of the NASA ITS_LIVE surface velocity map (Gardner, 2019), as these ice shelves show signs of having distinct flow regimes and dynamics, although physically linked (Anderson *et al.*, 2014).

3.4 Time Series Generation

It was possible to map the entire coastline, including all ice shelves and glacier ice tongues for the years 2009 to 2019, and all ice shelves have area measurements extending back to at least 1990. However, for most ice shelves, the area timeseries was extended back to 1974 and, were DISP data quality allowed it, back to 1963. For the ice shelves where area measurements could not be established due to insufficient satellite data quality (i.e. due to cloud cover), data was omitted from the timeseries. The resultant ice shelf areas were plotted through time to analyse the overall trends in CFL migration and calving behaviour, initially considered as a whole-sector floating ice metric and then as individual ice shelves. In both cases, area changes were also calculated as a percentage of the previous ice shelf area and as a percentage of their glacial system, that is to say ice-shelf area plus drainage basin area quantified from MEaSUREs Antarctic Boundaries dataset (Mouginot, 2017). When making comparisons to data from prior to 1990, whole-sector changes are only considered relative to the previous measurement, as missing ice-shelf data mean that absolute comparisons cannot be made. Still, absolute area comparisons can be made with these dates at individual ice shelves where data exists. Area changes were subsequently converted into annually-averaged rates of change, by assuming change occurred equally within years. Clearly, in the case of large, tabular iceberg calving, this would not be the case; however, rates of change are used only to understand broadscale trends in ice-shelf area change.

Changes were considered primarily over the whole period 1974 to 2019 and then between individual epochs 1963 to 1974 (Ep.1), 1974 to 1990 (Ep.2), 1990 to 2000 (Ep.3), 2000 to 2009 (Ep.4) and 2009 to 2019 (Ep.5) to analyse approximately decadal trends. Clearly, the new data from this study allow for sub-decadal change analysis and, hence, some sub-decadal trends for the period 2009 and 2019 are also discussed.

3.5 Meteorological and Sea Ice Data

To investigate possible causes of trends in ice-shelf area change, meteorological and sea-ice concentration data were analysed on a decadal basis, to align approximately with the epochs of glacial change outlined in Section 3.4, not including 1963 to 1974. Due to a lack of meteorological monitoring stations in the region, meteorological data comes from the ERA5 reanalysis dataset which assimilates upper air and near surface observations into an atmospheric model, coupled with a land surface and wave model, to give meteorological conditions on a 30 km spatial grid resolution, back to 1979 (Copernicus Climate Change Service, 2017). Monthly- and annually-averaged surface air temperature (2 m), together with wind speed (10 m) anomalies were analysed in the region in each decade from 1979 to 2019. These datasets are discussed in the context of the overall ice-shelf area trends, but mapping of these anomalies also allows for some consideration of influences on the geographical variations in ice-shelf change.

Similar analyses are made comparing CFL trends with monthly- and annually-averaged sea-ice anomalies in the region (Fetterer *et al.*, 2017). Additional consideration was given to local sea-ice anomalies at each ice-shelf front, to investigate possible localised influences on CFL change. Spatially averaged sea-ice concentrations for the areas immediately (< c. 150 km) in front of the CFLs were plotted in timeseries and compared to the trends in CFLs. The sea-ice concentrations used in this analysis were derived from passive microwave remote sensing observations from the SMMR, SSM/I and SSMIS sensors, extending back to 1979 and are provided at a 25 km spatial grid resolution (NOAA/NSIDC Sea Ice Index v3; Fetterer *et al.*, 2017).

3.6 Error Estimation

Errors in the delineated coastlines can be categorised into two groups: (1) co-registration error and (2) digitisation error. The estimated error in the newly digitised CFLs arising from each of these types of error is summarised below.

3.6.1 Co-registration Error

Co-registration error arises as a result of satellite imagery being misaligned and so it is important that imagery is georeferenced in the same projection to be directly compared. Sentinel-1 data were projected during pre-processing, whereas Landsat imagery is provided already transformed into a projected product and, thus, the largest co-registration uncertainty is likely to exist between imagery from different satellites or sensors (e.g. Seale *et al.*, 2011). In the context of both the wide spatial extent of the area studied (10^3 km coastal length) and the very large amount of data processed in this dissertation, it was decided that Landsat imagery would be used as provided by the USGS and that the Sentinel data pre-processing and co-registration errors would be quantified and reported.

To estimate the co-registration error between images, easily recognisable locations across the study area, such as nunataks, were digitised as points from a variety of satellite scenes. The nature of the EWS Sector, with minimal fixed-position reference points on the ice-sheet surface, meant that co-registration points were limited to 14 (Appendix III). Satellite scenes acquired by Landsat-7 (ETM+) in 2009 were used as a base layer and digitised points from this imagery were used as ground control points. The average distance of points digitised from imagery acquired by other satellite sensors, or other ETM+ scenes, away from these control points was taken to be the error for the given satellite platform sensor type, in a similar manner to (Lovell *et al.*, 2017). The median was used given the small number of control points, to avoid biasing the error in favour of exceptionally large or small distances, which were particularly prominent in the mountainous regions towards the edge of Sentinel-1 EW scenes. Nonetheless, manual sense-checking of these co-registration errors found values at the CFLs to be considerably less than the co-registration exercise would suggest, indicating that the largest co-registration errors were indeed likely to be in the mountainous regions, away from the CFLs.

The distance between points digitised from different sensors and the control points was comparatively large for Sentinel-1 EW scenes, at an average ± 1365 m, but less for other sensor types (Table 3.5). Although these distances were lower between scenes acquired by the same satellite sensor, at ± 322 m (EW), ± 19 m (IW), ± 78 m (ETM+) and ± 41 m (OLI), because a variety of satellite imagery from various instruments, was used in this dissertation to make interannual comparisons, the estimated error in digitised CFLs includes the between-sensor error. Because the focus of this study is on large temporal- and spatial-scale advances or calving activity, absolute CFL position is deemed less important than the identification of broadscale trends in CFL fluctuations.

Median (Maximum) Co-registration Error (m)	
Platform	**Error**
Sentinal-1 EW	± 1365 (4496)
Sentinel-1 IW	± 760 (2581)
Landsat-8 OLI	± 44 (355)
Landsat-7 ETM+	± 78 (756)
1963_Argon	± 436 (1410)

Table 3.5: The estimated co-registration error in CFLs digitised from each satellite/sensor type.

3.6.2 Digitisation Error

Digitisation error is resultant of mouse variation or unintended mouse movement, plus the uncertainty caused by the subjectivity in CFL identification in satellite imagery, discussed in Section 2.2.3. The digitisation error was therefore estimated by repeatedly digitising sections of coastline of at least 150 km in length. Eight satellite image scenes were selected, two for each EW, IW, OLI and ETM+, to include a mix of open ocean, sea ice, crevassed ice, rifts and snow cover, so as to be representative of the entire EWS coastline. Manual delineation was carried out for CFL sections of between 150 and 350 km, ten times for four of the selected satellite scenes, and edge-detected delineation was carried out five times for each of the remaining four scenes. Delineated lines were converted into points at 10 m spacing and k nearest neighbour analysis was carried out to calculate the mean distance between the lines. The resulting mean digitisation errors are shown in Table 3.6, with a measure of error for CFLs digitised from each type of satellite sensor and digitising method.

Mean error was used as opposed to the maximum error because the maximum measurements (± 3331.3 m) originate in areas where there was disagreement between digitisations in the inland extent of rifts and, thus, were extremely localised and not representative of the error in longer sections of CFL measurements. Such errors, therefore, will have minimal overall effect on the calculation of ice-shelf areas. Moreover, the maximum digitisation error has been found to be not usually representative of manually digitised datasets; instead the mean is a more accurate measure of digitisation error (Frith, 1997).

Mean error in the edge-extracted digitisation method was found to be less than the 10 m spacing of points along digitised lines and the 15 m maximum resolution of the satellite imagery and, thus, the digitisation error in CFLs mapped using exclusively edge-detection is limited to the spatial resolution of the satellite imagery (Appendix II). Furthermore, whilst the Sobel operator does occasionally miss-classify CFLs in areas where other edges are present (e.g. sea-ice/ocean-surface

boundary) the digitisation error still reduced compared to that from manual digitisation alone, due to the "snapping" nature of the ArcMap Vector Trace Tool combined with visual checks.

However, since CFLs were mapped using a combination of manual and semi-automatic edge-detection, a weighted-average error was calculated for each section of coastline, based on the satellite and sensor which acquired the image used for CFL delineation and the proportion of CFL delineated using manual methods versus edge-extracted methods, shown in Table 3.6. Because much of the CFL vectorization used a "hybrid" approach described in Section 3.2., individually tagging CFL segments as manually- or semi-automatically mapped was not considered practical and therefore, the following assumptions were made, based on notes recorded during digitising (as tagged in the attribute table): 50% manual delineation, 50% edge-extracted delineation, where segment notes read "Some use of Edge Extraction", or similar; 25% manual delineation, 75% edge-extracted delineation where notes recorded "Extensive use of Edge Extraction", or similar; and 100% edge-extracted delineation where notes read "Exclusive use of Edge Extraction".

Mean (Maximum; Median) Digitising Error (m)		
Platform	**Manual**	**Edge Extracted**
Sentinal-1 EW	± 102.7 (3331.3; 51.3)	± 2.1 (76.5; 1.4)
Sentinel-1 IW	± 62.9 (1875.6; 30.6)	± 5.3 (122.2; 2.9)
Landsat-8 OLI	± 34.8 (1411.0; 24.7)	± 2.6 (62.6; 2.4)
Landsat-7 ETM+	± 34.8 (1411.0)	± 2.6 (62.6; 2.4)
1963_Argon	± 106.0 (963.7)	N/A

Table 3.6: The estimated digitising error for CFLs digitised from each sensor/satellite type and using each technique: manual or semi-automatic edge-extraction.

3.6.3 Total Error

The total coastline error for each segment of coastline (Table 3.7) was calculated by summing together the co-registration and digitisation errors, based on the satellite sensor type and digitisation technique used for digitisation. The overall mean error in these digitised CFL sections is ± 373 m, but 70% of delineated CFLs have an error < ± 120 m and 90% have an error < ± 850 m. This figure compares to the 85% of CFL measurements with error < ±180 m along the Antarctic Peninsula (Cook and Vaughan, 2005). The largest error is associated with the 2015 CFLs, and related change detection, as many of these were digitised from Sentinel-1 EW scenes, which are subject to the largest co-registration error. The maximum error in any given CFL section is estimated to be ± 1467 m for the coastline of Berkner Island in 2015, which was exclusively manually delineated from Sentinel-1 EW imagery.

Overall Error (m)		
Platform	**Manual**	**Edge Extracted**
Sentinal-1 EW	± 1,467	± 1,367
Sentinel-1 IW	± 823	± 766
Landsat-8 OLI	± 79	± 47
Landsat-7 ETM+	± 112.7	± 81
1963_Argon	± 541	N/A

Table 3.7: The estimated total error in CFLs digitised from each satellite/sensor type using each digitising technique: manual or semi-automatic edge extraction.

Like the digitising error calculation strategy used for newly digitised CFLs in the years 2009 to 2019, repeated delineation of the CFL at Filchner Ice Shelf was used to quantify the digitising error of the DISP (1963) imagery, which was found to have a mean digitising error of ± 106 m. This was combined with the mean co-registration error of ± 436 m, computed from the distance between points in this image and the 1990 ETM+ control points, to give an overall error in the 1963 CFLs of ± 541 m.

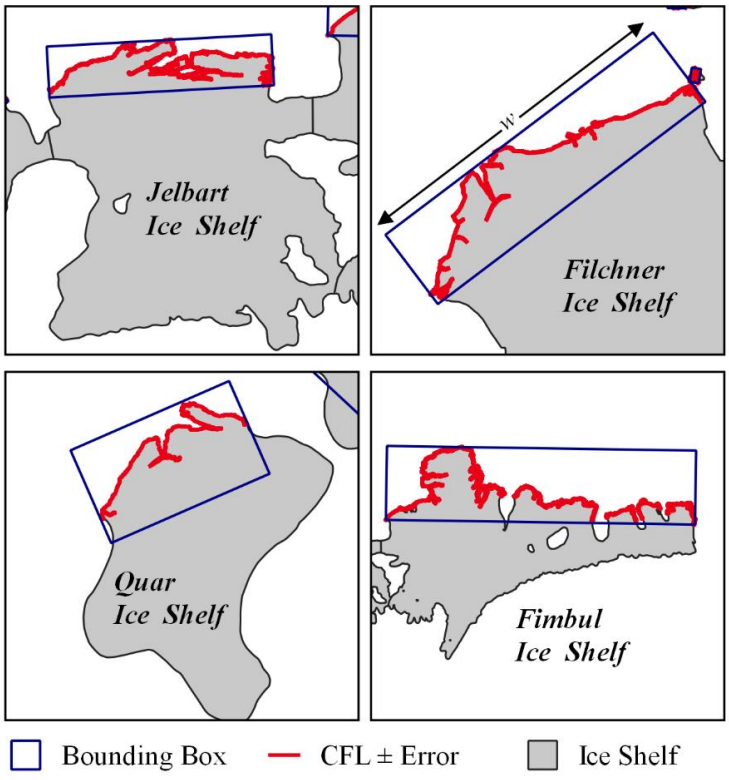

Figure 3.4: Example oriented minimum bounding boxes used to covert error in CFLs to error in ice-shelf areas. The thickness of the red line represents the uncertainty (d_{err}), which is multiplied by the bounding box width (shown as w) to calculate an approximate error in area (A_{err}) i.e. $A_{err} = d_{err} \cdot w$.

Ice-shelf area error (A_{err}) was calculated using the width (w) of an oriented minimum box enclosing the calving front (Appendix V), multiplied by the error in the CFL (Figure 3.4 and **Error! Reference source not found.**Table 3.7) (or the error in depth (d_{err})) for each given ice-shelf as shown in Figure 3.4; an approach similar to the "box method" described by Lea *et al.* (2014) to calculate CFL fluctuations. The average ice-shelf area error for ice shelves with CFLs digitised in this study is estimated to be ± 40 km^2, with a maximum estimated error of ± 505 km^2 for the Riiser-Larsen Ice Shelf in 2015. Proportionally, the large ice shelves of the region were subject to lower areal error at a mean ± 0.58%, compared to the Coats Land glacier tongues which have mean area errors of ± 15%. The regions of the 1963 DISP mosaic where cloud cover prohibited CFL delineation,

but manual upper and lower CFL bounds were approximated (Filchner Ice Shelf and Fimbul Ice Shelf), these bounds were added to the digitising error to quantify maximum and minimum ice-shelf areas (+ 203 km^2, - 513 km^2 and + 583 km^2, - 464 km^2, respectively).

Error in measurements of change was calculated by summing the calculated errors associated with each datapoint. Illustratively, an area change in ice-shelf *X* (δA*X*) has error in ice-shelf area at time *a* (AX_{err} a), plus the error in ice-shelf are at time *b* (AX_{err} b) and, hence, the error represents the maximum areal change given the estimated errors at each timepoint. Similarly, average estimated error in rates of areal change were calculated by dividing the summed error by the number of years over which the rate is calculated (δA/yrs).

4 Results

4.1 The Eastern Weddell Sea Coastline and Calving Fronts

The total length of the EWS coastline stretching from the eastern edge of Ronne Ice Shelf to the eastern end of Fimbul Ice Shelf was quantified at 5,756 km in 2009 and 6,403 km in 2019, as mapped at the 1:30,000 viewing scale (Table 4.1). This extension of the total coastline was largely a result of CFL advance at the large (>1000 km^2, Table 4.2) ice shelves in the region, with the island and ice-rise coastline sections fluctuating very little between years and comparatively modest, in absolute terms, areal changes to floating glacier tongues along the Coats Land coast.

Year	Total coast length (km)	Large Ice Shelf CFLs (km)	Island/Peninsula Coastline and Glacier Tongues (km)
2009	5,756	4,829	927
2011	5,776	4,857	921
2013	5,933	4,989	944
2015	6,016	5,079	937
2017	6,237	5,277	961
2019	6,403	5,408	996

Table 4.1: The total length of CFL/coastline delineated for each year. Large ice shelf CFLs include the calving fronts and sides of the large ice shelves >1000 km^2 shown in Table 2. The island/peninsula coastline and glacier tongues include the glaciers draining from the Coats Land coast.

4.2 Total Area of Floating Ice

Ice Shelf	2019 Area (km^2)
Filchner	97,136 ± 290
Riiser-Larsen	43,455 ± 346
Fimbul	41,260 ± 530
Stancomb-Wills	30,160 ± 109
Jelbart	11,207 ± 85
Brunt	7,913 ± 108
Ekstrøm	6,948 ± 74
Quar	2,190 ± 35
Atka	1857 ± 50
Coats Land glaciers	255 ± 54
Total	242,381 ± 827

Table 4.2: The areas of digitised ice shelves in 2019.

The majority of contemporary floating ice in ice shelves and glacier tongues in the region is found in the large Filchner, Riiser-Larsen, Fimbul and Stancomb-Wills ice shelves (Table 4.2). In contrast to what has been observed at ice shelves along the AP, CFLs in the EWS region have broadly been synchronously advancing over the past two decades at least, resulting in a total increase in the area of floating ice by 6.2%, from c. 228,215 ± 274 km^2 in 1990 to 242,381 ± 827 km^2 in 2019 (Figure 4.1), as measured from delineated CFLs and created ice-shelf polygons. Despite areal measurements of some ice shelves in the region not being available for earlier dates, analysis of the available ice-shelf polygons suggests that the area of floating ice was greater than at present by 3 – 4% in 1963 and by 1 – 2% in 1974. For instance, whilst the Stancomb-Wills Ice Shelf area could not be quantified for 1963, due to cloud cover in the 1963 DISP imagery, the section of the CFL which is visible was approximately c. 60 – 70 km behind the current (2019) CFL position (Figure 4.2e). Thus, the

data presented here indicate a continuation of the broadscale trends identified by Miles *et al.* (2016), who found CFLs in the region to generally be retreating during the period 1974 to 1990 but advancing since then, up until 2012.

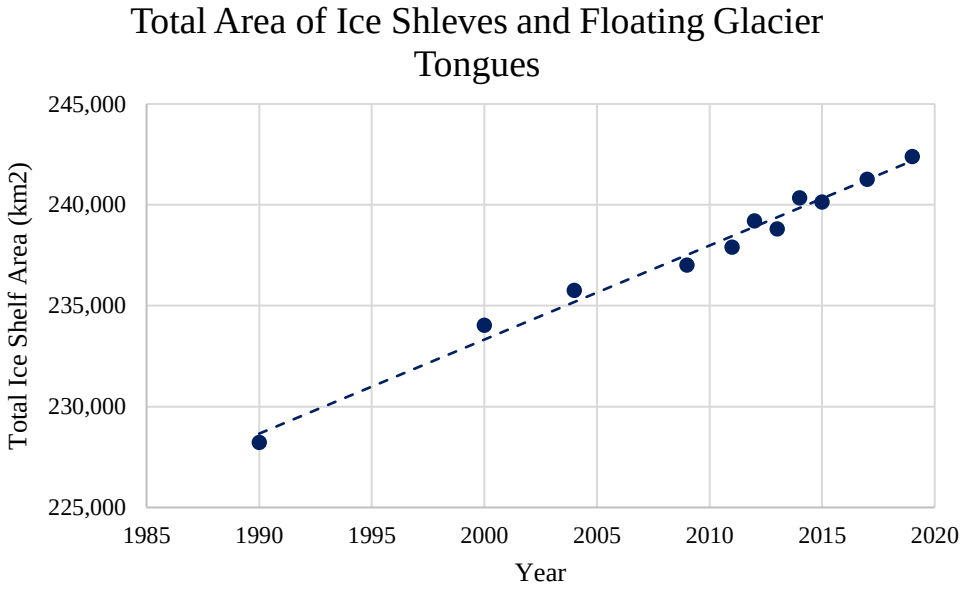

Figure 4.1: Total area of ice shelves and ice tongues in the EWS region. Applying a linear trendline shows the total ice shelf area to be increasing by an average 466 km^2 yr^{-1} since 1990.

However, whilst rates of areal expansion have remained relatively high since 1990, fluctuating around a linear trend of +466 km^2 yr^{-1} (trendline in Figure 4.1), evidence indicates that rates of advance have accelerated since the 2000 – 2010 epoch, to highs occurring over the past five to seven years, most recently increasing at an average rate of c. +550 km^2 yr^{-1} between 2015 and 2019 compared with c. +340 m^2 yr^{-1} for 2000 - 2010 (Figure 4.3). Although the highest average rates of areal expansion in any time period were found to be between 2013 and 2015, at +663 ± 1615 km^2 yr^{-1}, the comparatively high uncertainty in this figure should be noted due to the relatively high co-registration error associated with Sentinel-1 EW data and, therefore, the averages across several years shown in Figure 4.3 are likely a better representation of the true values. Furthermore, higher than average ice-shelf area increases to 2004 and 2014 are likely to be as a result of the coarser digitisation scale of these datasets digitised from MODIS imagery, whereby significant glacial rifts were not included in their CFLs. Regardless of these error quantities, it is clear that ice shelves in the region were at their maximum known area in 1963, and that CFL retreat dominated in the 1974 – 1990 epoch (Figure 4.3). Since that time, broadscale ice-shelf areal advance has been occurring at rates equivalent to c. 0.2% of the total floating ice area per year since at least 1990 (Figure 4.3).

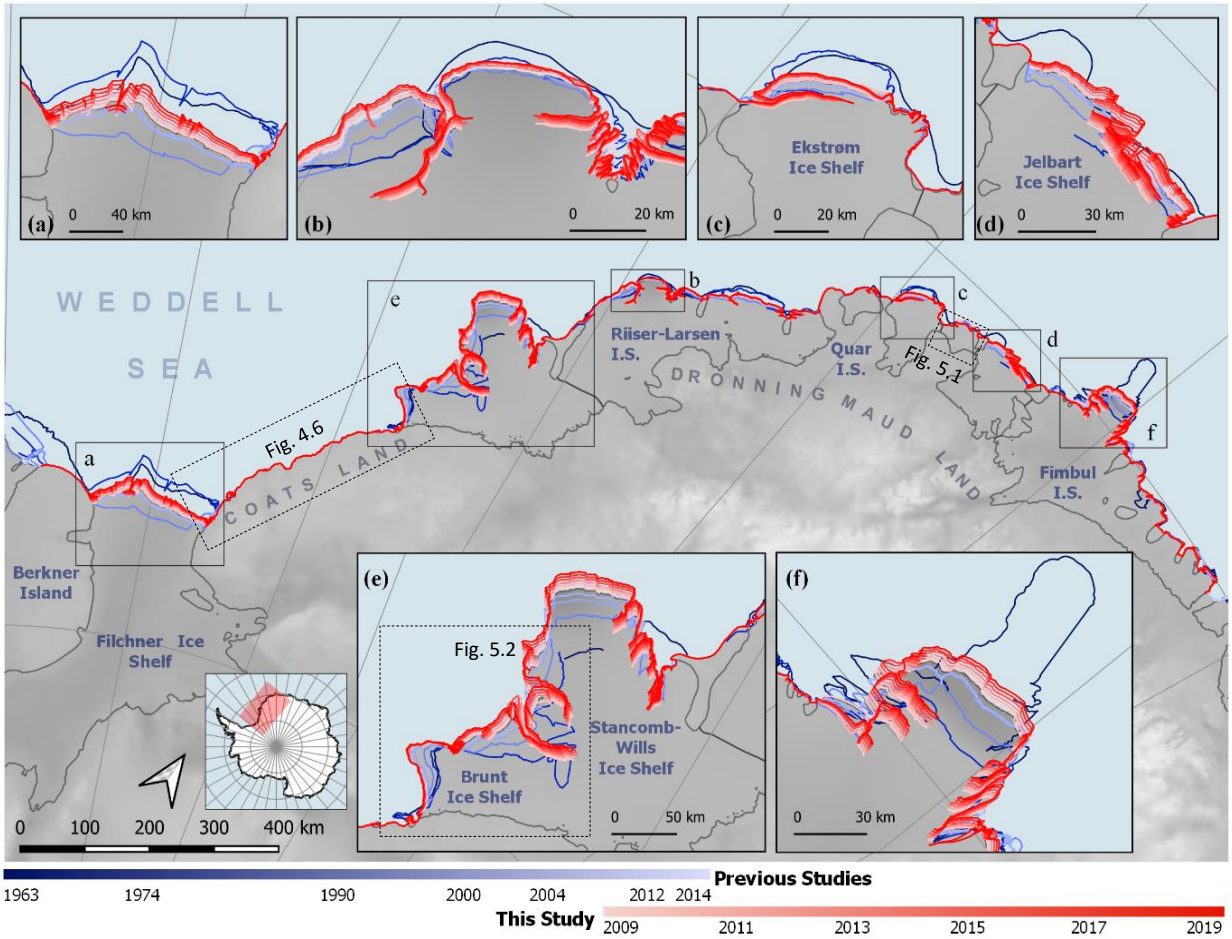

Figure 4.2: The mapped CFLs and coastlines. Blue lines are from pre-existing datasets, 1974 (dark) to 2014 (light) as well as the 1963 (darkest) dataset which has been delineated from the DISP 1963 mosaic. Red lines are the new datasets presented in this study from 2009 (lightest) to 2019 (darkest). Grey lines mark the ice shelf boundaries used to measure ice-shelf areas. Note the varying scales used in insets. Basemap shows bed elevation (Source: BEDMAP2 Fretwell, 2013).

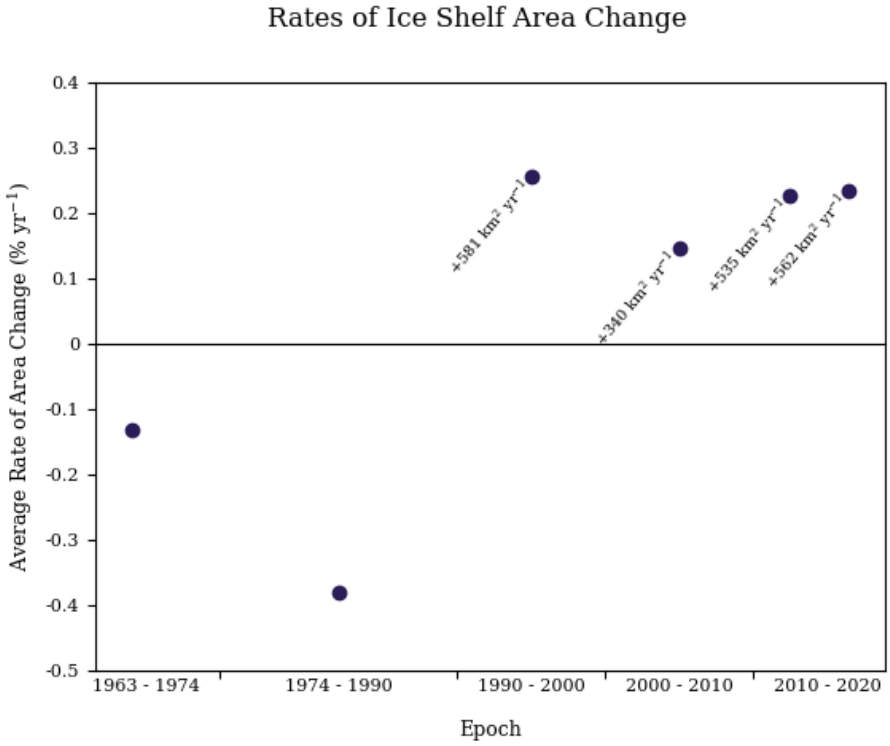

Figure 4.3: Rates of change in total ice shelf area in the EWS region, averaged during each epoch (Ep.1 – Ep. 4) and half-epoch (Ep.5), due to greater temporal resolution of data during this period.. Rates are shown as average percentage change per year, due to incomplete datasets prior to 1990, but absolute values are labelled for the values since then.

4.3 Spatial Variations in Calving Front Location Changes

4.3.1 Large Ice Shelves

When considering the cumulative loss of ice-shelf area between 1963 and 1990, spatial variations in CFL change reveal how individual calving events can dominate the net ice-shelf area loss from the region (Figures 4.4 and 4.5). For example, of the 1.44% reduction in mapped EWS floating ice during Ep.1, the calving of the 53 by 104 km "Trolltunga" iceberg from the outlet of Jutulstraumen Ice Stream on the Fimbul Ice Shelf, accounted for a 1.89% reduction in the overall floating ice area, implying that other ice shelves actually advanced on average during the period. Similarly, the breakup of the Filchner Ice Shelf Front north of the 115 km by 11 km "Grand Chasm" in 1986 (Swithinbank, 1988); red line in Figure 4.4a) contributed 5.2% of the overall 6.1% area decrease of mapped ice shelves. However, while there were also significant contributing areal reductions from Ekstrøm (694 ± 32 km^2) and Riiser-Larsen (1673 ± 141 km^2) ice shelves during this period, the magnitude of the Filchner Ice Shelf areal reduction dwarfs the combined total EWS ice-shelf areal change over any other time period considered (Figure 4.5).

The more recent broadscale trend of synchronous CFL advance since at least 1990, recorded by the new data presented here, has been relatively uniform across the study region, particularly amongst the large ice shelves > 1000 km^2 in Table 4.2 (Figure 4.4). Perhaps unsurprisingly, the greatest rates of contemporary CFL advance are occurring at the floating ice tongues of the great ice streams draining from the inner ice sheet, including the Filchner Ice Shelf, Stancomb-Wills Ice Shelf and at the outlet of the Jutulstraumen Ice Stream on Fimbul Ice Shelf, where average ice-shelf areal expansion has measured 2174 ± 416 km^2 (5443 ± 290 km^2), 1368 ± 186 km^2 (3502 ± 180 km^2) and 479 ± 786 km^2 (1085 ± 530 km^2), respectively, between 2009 (1990) and 2019. Nonetheless, average rates of areal expansion were not insignificant over this same period (Ep.5) at other ice shelves in the region, including at the Riiser-Larsen (57 ± 30 km^2 yr^{-1}), Jelbart (33 ± 9 km^2 yr^{-1}) and Brunt (42 ± 10 km^2 yr^{-1}) ice shelves (Figures 4.4 and 4.5a).

In fact, when considering areal changes relative to the total glacial system size (i.e. drainage basin + ice shelf), it is clear that areal fluctuations of other, smaller ice shelves have been proportionally significant (Figure 4.5b). For example, Atka Ice Shelf lost c. 6.3% of its area, or c. 3.6% of its combined glacial system size, between 2009 and 2019, due to a calving event of an iceberg at least 145 ± 10 km^2 which occurred at some point between 14th March and 20th November 2009, judging by Landsat-7 ETM+ acquisitions on these dates. Furthermore, the Brunt/Stancomb-Wills ice shelf system stands out due to its areal expansion rate relative its size since at least 1990 (Figure 4.5b), with for instance, Brunt Ice Shelf increased in size by c. 20% during Ep.4, albeit slowing to a c. 5.5 %

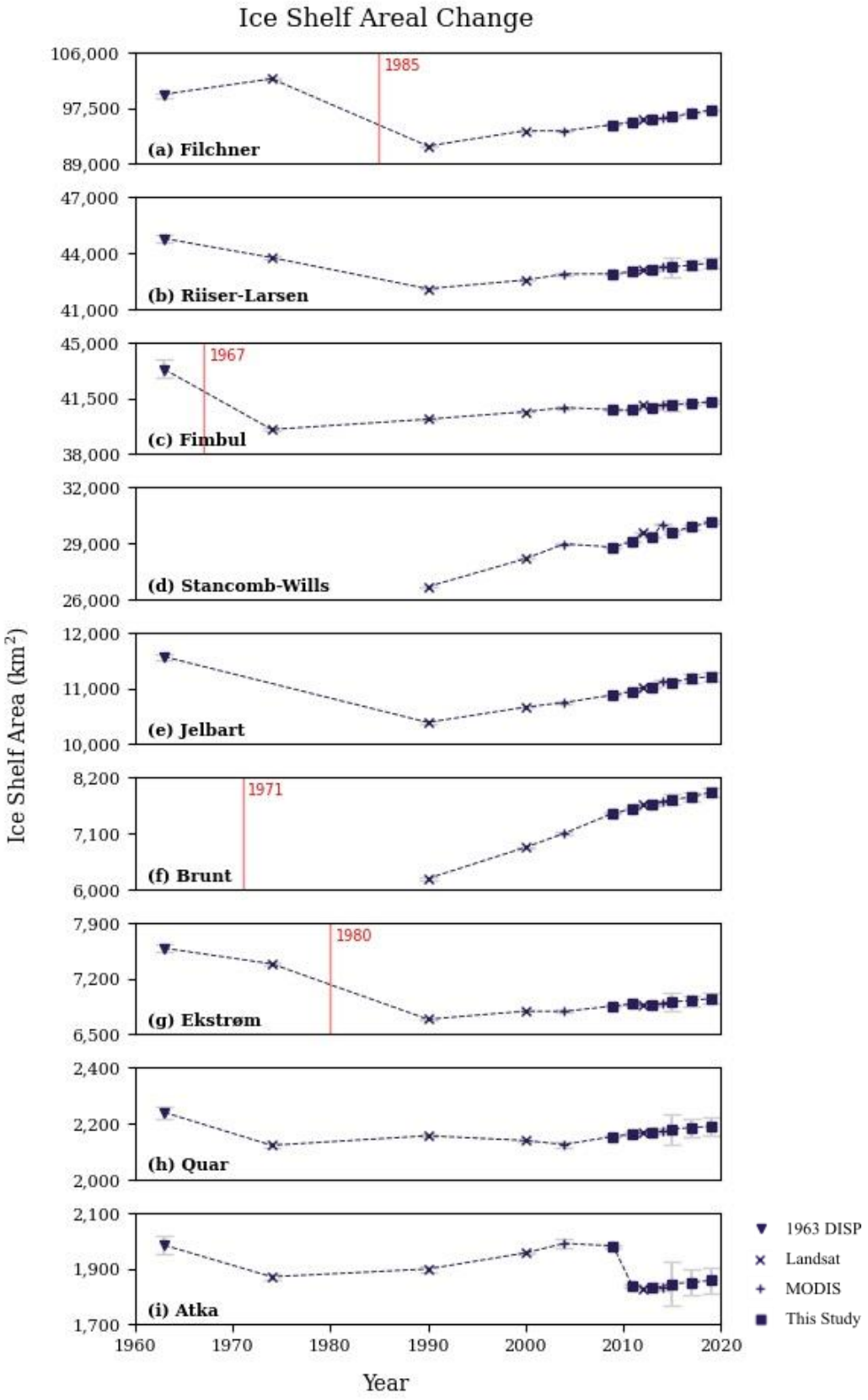

Figure 4.4: The changing areas of the significant ice shelves in the EWS region, since 1963. Ice Shelves are listed largest to smallest, so note the changing (decreasing) y-axis scales from top to bottom. Areas calculated from CFLs delineated from 1963 DISP imagery are plotted as triangles, delineated by Miles et al. (2013) from Landsat imagery as X's, delineated by Haran et al. (2005; 2018) from MODIS imagery as +'s and delineated in this study as squares. Grey bars show estimated error. Red lines show the last recorded significant calving event found by a review of the relevant literature.

increase in Ep.5. This is equivalent to an increase in glacier-system area by more than 2% decade^{-1} during Ep.3 and Ep.4, and more than 1% decade^{-1} during Ep.5 (Figure 4.5b).

Aside from calving of Atka Ice Shelf in 2009 (Figure 4.4i), however, there have been no significant calving events resulting in CFL retreat since at least 1990 (Figure 4.4). In fact, a review of relevant literature has found the last major documented calving event in the study area is that of the Filchner ice front in 1986 (Swithinbank, 1988) and, prior to that, at Ekstrøm ice front in 1980 (Lange and Kohnen, 1985). The significant calving events identified in the literature are shown as red lines in Figure 4.4, but additionally, Stancomb-Wills Ice Shelf has not undergone any substantial calving since at least 1955, but did lose significant area sometime after 1915 (Thomas, 1973).

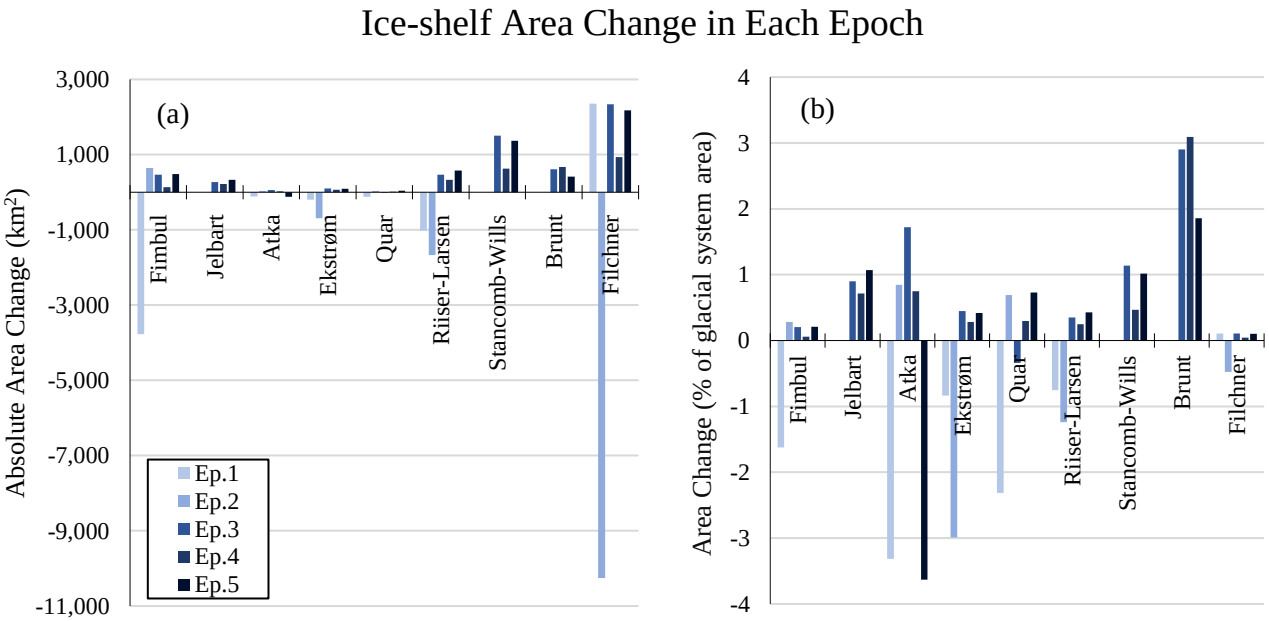

Figure 4.5: Individual ice-shelf area changes during each of the epochs studied as (a) absolute measurements and (b) percentage of glacial-system size (i.e. ice-shelf + glacier drainage basin size).

Ep.1 = 1963 – 1974, Ep.2 = 1974 – 1990, Ep.3 = 1990 – 2000, Ep.4 = 2000 – 2009, Ep.5 = 2009 – 2019.

4.3.2 Coats Land Glacier Tongues

In contrast to the recent synchronous advance of the large ice shelf fronts, the relatively small ice tongues extending from the glaciers of the Coats Land coast have displayed more variable behaviour (Figures 4.6 and 4.7). For example, Schweitzer and Dawson-Lambton glaciers CFL advance has resulted in areal expansions of 50 ± 6 km^2 and 20 ± 4 km^2, respectively, since 1990 (Figures 4.6f and 4.6e, 4.7a and 4.7c), but Wiedenmanngletscher CFL retreat over the same period has resulted in a 80 ± 4 km^2 loss of area, 55 ± 1 km^2 of which occurred between 2000 and 2009 (Figures 4.6g and 4.7b).

Over the longer term, Schweitzer Ice Shelf has advanced 68 ± 9 km^2, to 165 ± 7 km^2, since the first calculated area in 1974 (Figure 4.7a). This is in contrast to both the next two largest ice tongues,

of Dawson-Lambton and Wiedenmannglетscher, which have both retreated (Figure 4.7c and 4.7b). Fundamentally though, Wiedenmannglетscher flowed into Filchner Ice Shelf prior to its significant 1986 calving and Dawson-Lambton Ice Shelf appears to have been attached to Brunt Ice Shelf in 1968

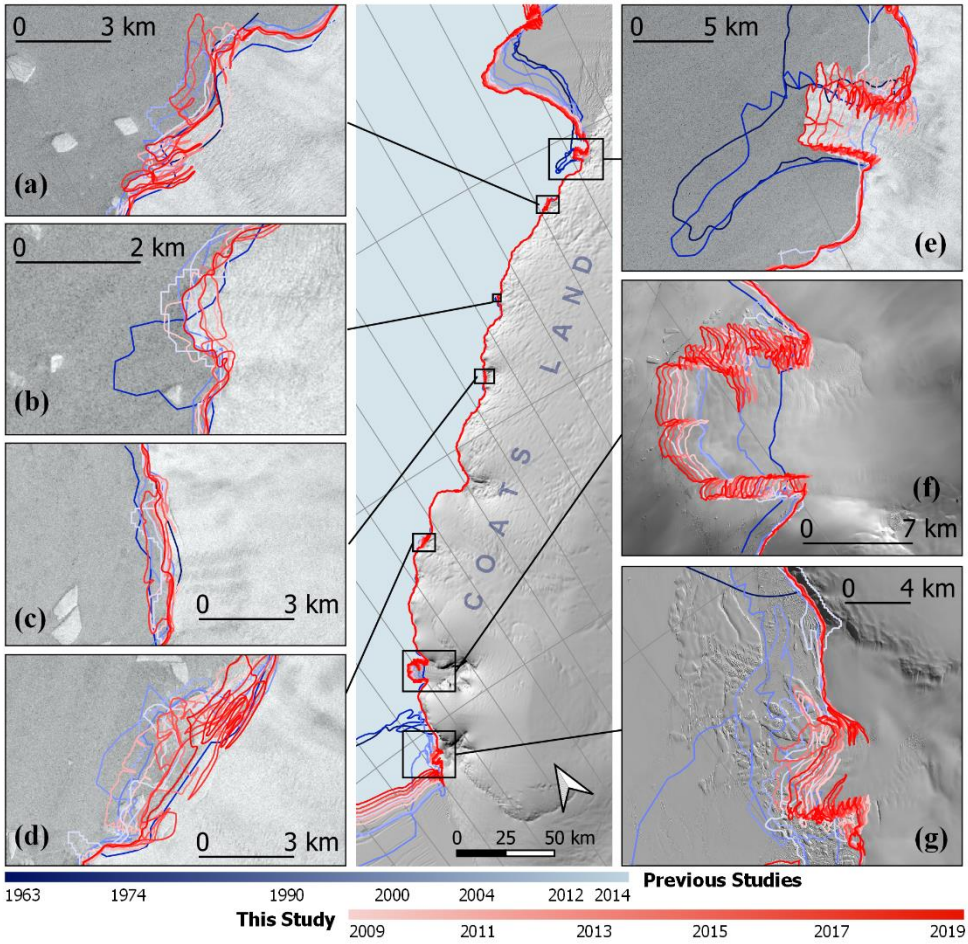

Figure 4.6: The mapped CFLs and coastlines along the Coats Land coast (Labelled Fig.7 in Figure 2). Insets show location of Hayes (a), Glacier 1 (b), Mann (c), Mosley (d), Dawson-Lambton (e), Schweitzer (f) and Wiedenmannglетscher (g) CFLs in Sentinel-1 IW (a – e) and Landsat-8 OLI (f & g) imagery. Note the varying scales used. Blue lines are from pre-existing datasets, 1974 (dark) to 2014 (light), as well as the 1963 (darkest) dataset which has been delineated from the DISP 1963 mosaic. Red lines are the new datasets presented in this study from 2009 (lightest) to 2019 (darkest). See Figure 4.2 for location.

and 1974(?) by land-fast sea ice. Therefore, areal changes in these ice tongues should not be considered independently of their significantly larger ice-shelf neighbours.

More recent (since 2009) fluctuations in CFL positions at Mosley, Hayes, Mann glacier tongues are largely within the margin of error, however, it is clear that there has been no overall trend in the CFLs of these glaciers towards advance or retreat since 1990 (Figures 4.6 (a – d) and 4.7 (d – g)). An exception might be at Glacier 1, where the terminus has advanced since at least 2015 (Figures 4.6b and 4.7g), albeit that the absolute scale of change here is insignificant when compared to the larger ice tongues. Indeed, the modest overall areal change of floating ice along the Coats Land coast, at -44 ± 4 km^2 between 1990 and 2011, is largely a result of Wiedermannglетscher CFL retreat. Moreover,

the subsequent areal increase of +15 ± 84 km^2 between 2011 and 2019 reflects the synchronous advance of Schweitzer and Dawson-Lambton CFLs.

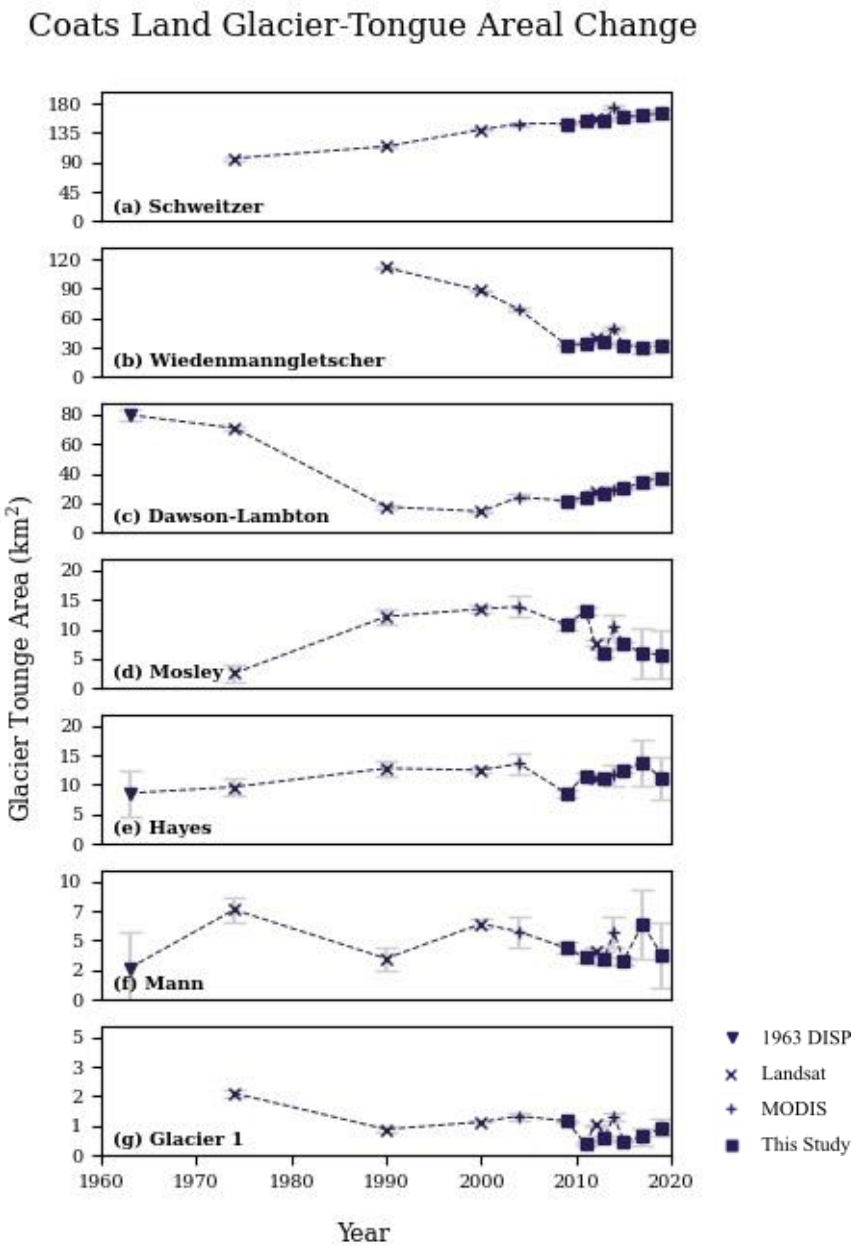

Figure 4.7: The changing areas of the ice shelves along the Coats Lands coast, since 1963. Ice Shelves are listed largest to smallest, so note the changing (decreasing) y-axis scales from top to bottom. Areas calculated from CFLs delineated from 1963 DISP imagery are plotted as triangles, delineated by Miles et al. (2013) from Landsat imagery as X's, delineated by Haran et al. (2005; 2018) from MODIS imagery as +'s and delineated in this study as squares. Grey bars show estimated error.

4.4 Metrological and Sea Ice Conditions over the Eastern Weddell Sea

Analysis of the meteorological and sea-ice data reveal that, similar to other regions in Antarctica, surface air temperatures have been increasing at the vast majority of the Filchner, Riiser-Larsen, Ekstrøm, Jelbart and Fimbul ice shelf surfaces since 1979 (Figure 4.8), at average rates > 0.06 °C yr^{-1},

concurrent with the broadscale advance of CFLs in the region. Nevertheless, monthly-averaged surface (2 m) air temperatures rarely reach above freezing over these ice shelves, with significantly lower average surface temperatures inland, over the ice sheet interior (Appendix VIII). However, there is no significant warming trend over the surface of the Weddell Sea beyond the coast according to ERA5 reanalysis data.

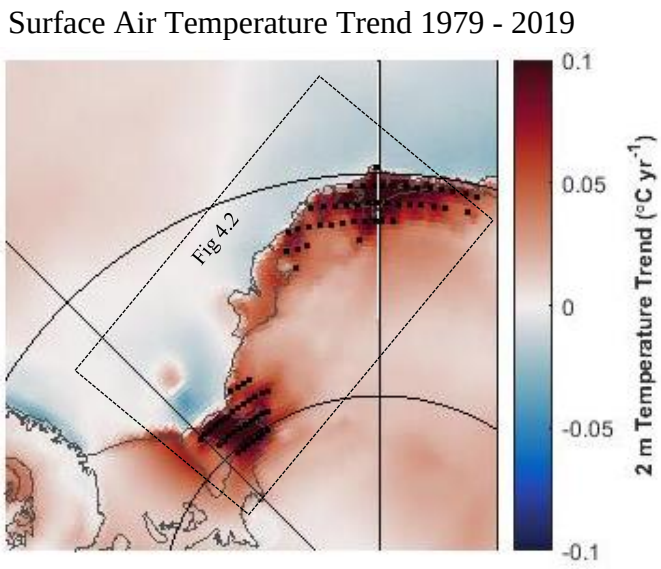

Figure 4.8: Trend in surface (2 m) air temperatures 1979 – 2019, from the ERA5 dataset (discussed in text), over the EWS region. Black dots denote significance to the p=0.05 level. Mapped using Antarctic Mapping Tools (Greene et al., 2017).

Like air temperatures, wind speed anomalies, in a southerly direction along the EWS coastline, have been increasing since 1979, particularly over the last decade, when monthly-averaged anomalies in the 10 m wind speed have averaged > 0.1 m/s to the south (Figure 4.9b). This is, in fact, a reversal of the wind-speed anomalies between 1979 and 1990, when anomalous average wind speeds were in a northerly direction along the EWS coastline (4.9a).

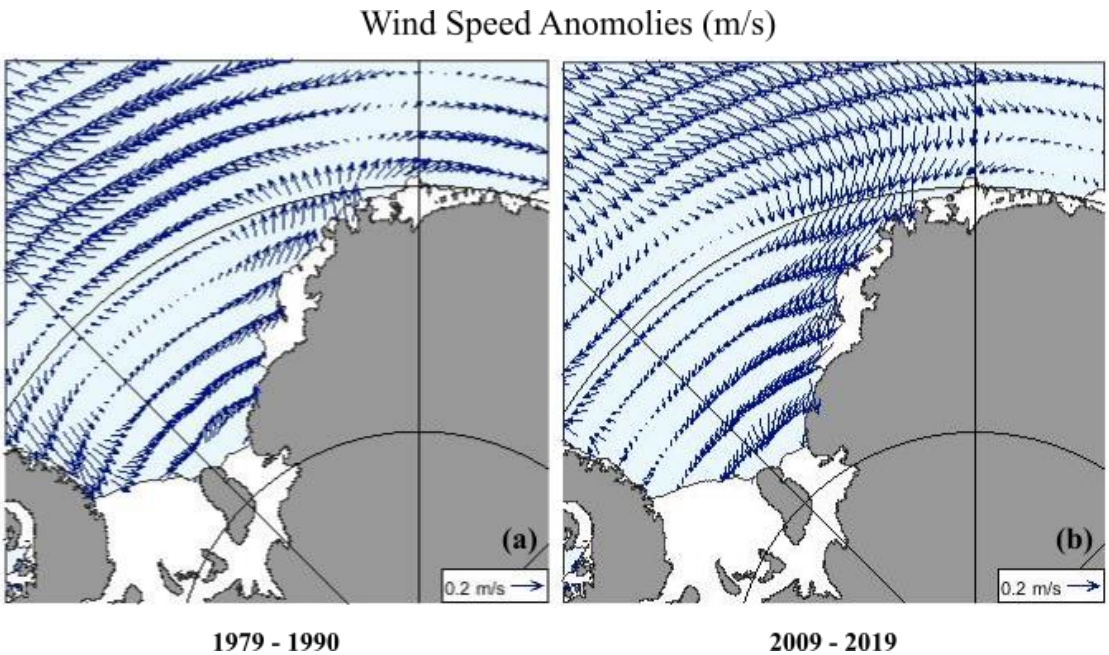

Figure 4.9: Average 10 m wind speed anomalies in the epochs 1979 – 1990 (a) and 2009 – 2019 (b), compared to the long-term (1979 – 2019) average. Arrow size signifies the scale of the anomaly. Data source: ERA5 dataset discussed in text.

Anomalously high sea-ice concentrations > 5% higher than the long-term (1979 – 2019) average persisted at the margins of the southern ice shelves from Filchner to Riiser-Larsen CFLs during the 1990s and 2000s (Figure 4.10b and 4.10c). This has changed over the past decade, however, where

anomalously low sea-ice concentrations > 2% less than the long-term average have been recorded in front of Brunt and Stancomb-Wills ice shelves and at the northern Coats Land coast (black circle in Figure 4.10d). In contrast, sea-ice concentrations beyond the northern ice shelves, from Fimbul to Quar, were around the long-term average during the 1990s, but have since increased to monthly average concentrations > 3% above the long-term average, during the 2010s (Figure 4.10d). Despite the recent spatial variations, sea-ice concentrations across the whole region where low prior to 1990, compared to the long-term average (Figure 4.10a). Thus, the overall trend in sea-ice concentrations in the EWS region between 1979 and 2019 can be summarised as broadscale increasing concentrations, but with anomalously low concentrations in the southern part of the study area during the past decade.

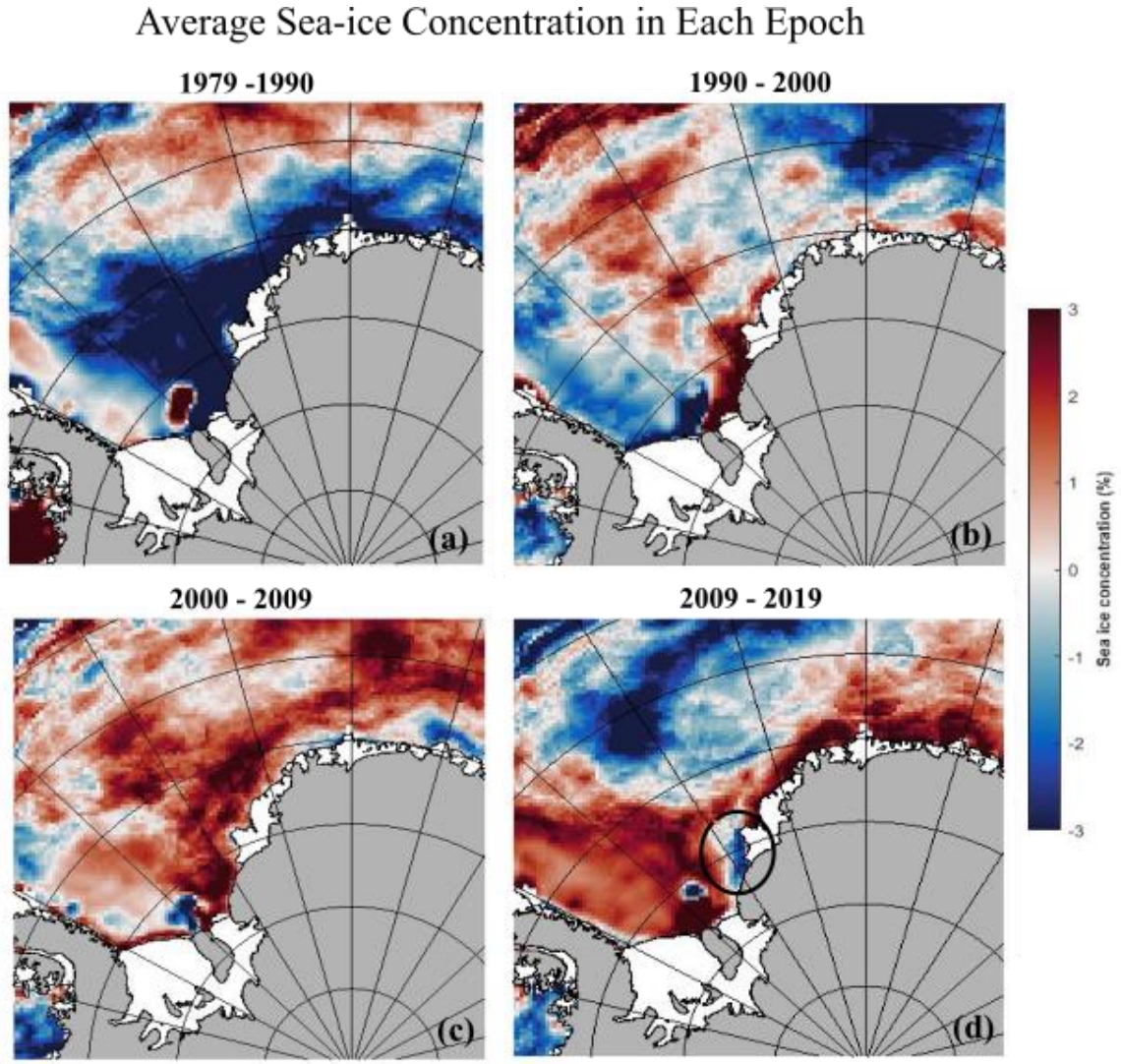

Figure 4.10: Sea-ice concentration anomalies from the long-term (1979 – 2019) average, in the southern and eastern Weddell Sea, during the epochs 1979 – 1990 (a), 1990 – 2000 (b), 2000 – 2009 (c) and 2009 – 2019 (d). Data source: ERA5 data discussed in text.

Investigating more localised sea-ice conditions at individual ice-shelf fronts has shown how the calving event of Atka Ice Shelf in 2009 was preceded by four years of anomalously low annually averaged sea-ice concentrations (Figure 4.11). Although sea-ice concentrations had returned to levels

approximately equal to the long-term average by early in that year, April sea-ice concentrations were c. 20% below the long-term average. Furthermore, sea-ice concentrations at Filchner Ice Shelf were similarly between 5% and 20% lower than the long-term average for at least four years prior to the 1985/86 calving event (Figure 4.12). At the margins of other ice-shelves in the region, no specific localised trends, different to the overall regional trends outlined above, where identified.

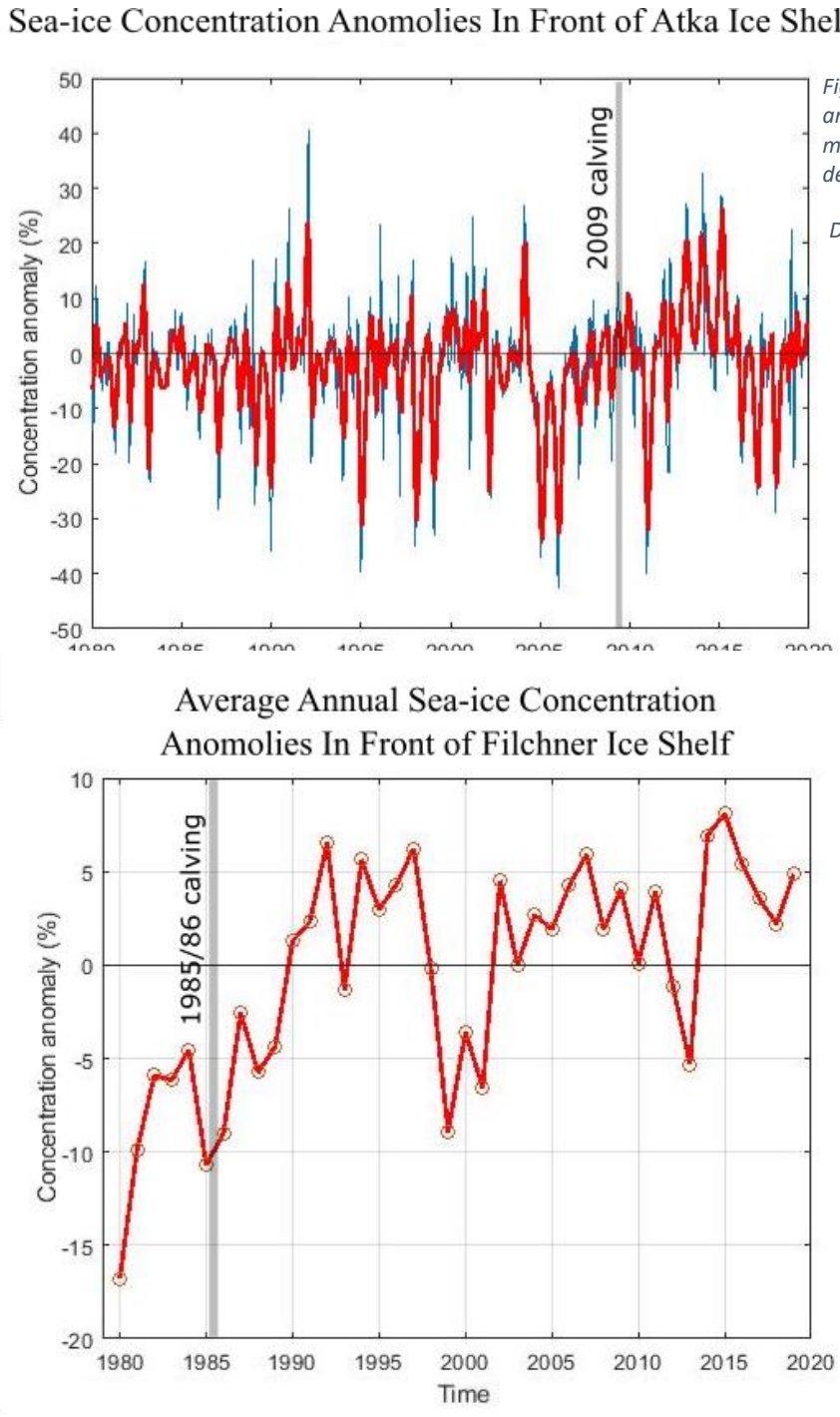

Figure 4.12: Annually-averaged sea-ice anomalies from the long-term (1979 – 2019) mean, at the forefront of Filchner Ice Shelf, derived from microwave remote sensors.

Data source: ERA5 data discussed in text.

5 Discussion

Despite four of the ten largest ice shelves in Antarctica being located in the EWS region, ice-shelf area change is in complete contrast to recent changes at the AP ice shelves, where over 28,000 km^2 of ice-shelf area has been lost in the five decades up to 2010 (Cook and Vaughan, 2010). Across the EWS region, where ice-shelf mass loss is known to be dominated by iceberg calving (Rignot *et al.*, 2013), the presented CFL fluctuations reveal that there has been relatively little iceberg calving activity on sub-decadal timescales, since at least 1963. Instead, the synchronous, multidecadal sustained advance of CFLs across the region is interrupted only occasionally by the detachment of large, tabular icebergs, which again is in stark contrast to the spatially extensive ice-shelf disintegration calving behaviour witnessed at the AP. Over the past decade, of all the large EWS ice shelves only Atka Ice Shelf has decreased in area, due to relatively significant calving in 2009.

5.1 Significant Calving Front Retreat and Iceberg Calving

Analysis of CFLs prior to 1990 reemphasise the importance of significant tabular iceberg calving to the overall ice-shelf mass loss of the region, particularly at the giant Filchner Ice Shelf, which drains a total area of the EAIS measuring c. 2.25 million km^2. Illustratively, during the period 1974 to 1990, total ice-shelf area loss from the region was almost entirely governed by the single calving event of the Filchner ice front in 1985/86, in which approximately 10,250 km^2 of the ice shelf calved. Assuming the average Filchner Ice Shelf thickness of 700 m (Lambrecht *et al.*, 2007), this would signify an approximate volume (mass) loss of over 7,000 km^3 (6,400 Gt) and although the ice shelf could be thinner than average close to the calving front, due to basal melt by relatively warm surface waters, this does demonstrate the significance of Filchner Ice Shelf calving to the overall EAIS mass balance. In fact, estimated ice discharge from this single calving event is over twenty times the estimated annual volume change of all Antarctic ice shelves combined between 2003 and 2012 (-310 ± 74 km^3), a time during which the breakup of ice shelves along the AP prevailed (Paolo *et al.*, 2015), and far exceeds the annual Filchner Ice Shelf calving rate of -9 ± 1 Gt yr^{-1} between 2011 and 2017 (Wuite *et al.*, 2019). Similarly, the detachment of the large (53 by 104 km), tabular, "Trolltunga" from Fimbul Ice Shelf in 1967 dominated the ice-shelf areal change in the EWS region between 1963 and 1974. Because of the magnitude of these large calving events, (Shepherd *et al.*, 2010) note the significance of discrete, tabular, iceberg detachment events on global sea level rise and therefore, highlight the importance of continued monitoring for the next significant calving event, particularly at Filchner Ice Shelf calving front.

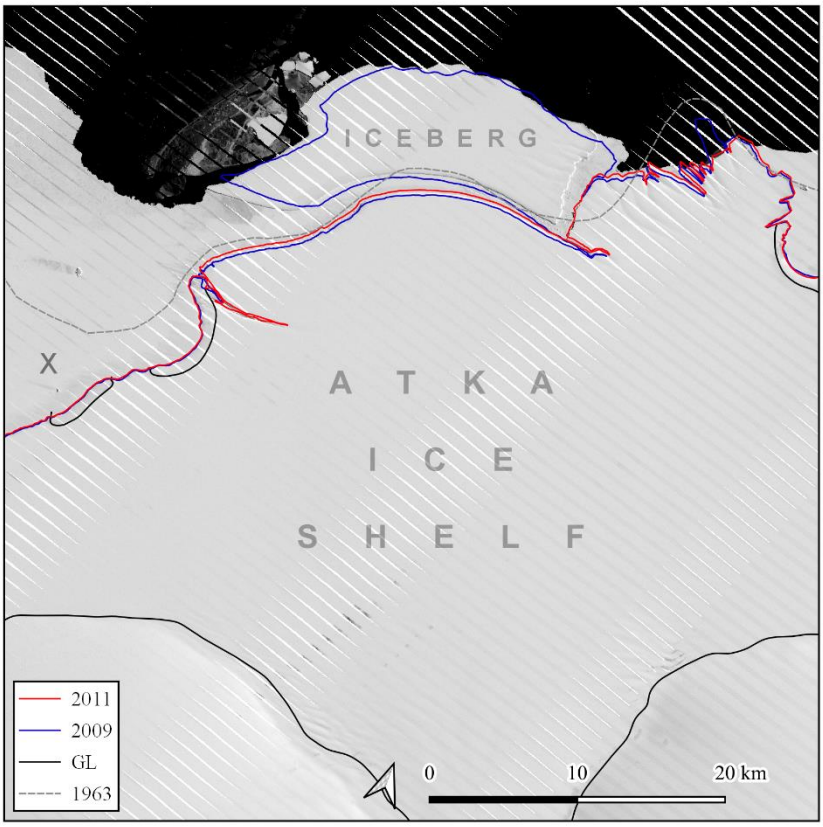

Figure 5.1: A portion of the delineated CFLs for Atka Ice Shelf in 2009 (blue) and 2011 (red) to illustrate the area of the iceberg which calved during 2009, overlaid on Landsat 7 ETM+ imagery acquired on 25th abd 27th November 2009. The dashed grey line is the CFL delineated from the 1963 DISP imagery, where "X" denotes the approximate area of ice shelf which retreated between 1963 and 1974. See Figure 4.2 for location.

Imagery courtesy of the USGS. Landsat scenes : LE07_L1GT_179110_20091125_20161217_01_T2_B8 and LE07_L1GT_177110_20091127_20161216_01_T2_B8.

However, there is so far no evidence in the CFL record to indicate that the frequency or magnitude of significant calving events may be changing in response to changing climatic, oceanic or ice-dynamical conditions. Given the multidecadal to centennial (e.g. Swithinbank, 1988) timescales over which these calving processes are occurring, it is perhaps premature to assert that there has been no change to the frequency or magnitude of iceberg calving in the EWS region. What is clear, however, is that the overall calving pattern across the region is one of cyclical detachment of large tabular icebergs, with minor seasonal and sub-annual input (e.g. Wuite *et al.*, 2019) and not one of systematic disintegration as has been recorded at the AP. This pattern of tabular iceberg calving is more often associated with ice shelves in neutral or positive mass balance regimes and therefore, the evidence from digitised CFLs indicates that unlike at the AP and coastal regions of the WAIS, this segment of the EAIS is not in negative mass balance (Liu *et al.*, 2015), which is broadly in agreement with recent mass balance studies derived using a variety of remote sensing technologies (Boening *et al.*, 2012; Shepherd *et al.*, 2018; Rignot *et al.*, 2019). Furthermore, recent hypotheses emphasising the relative importance of MICI in calculations of Antarctic mass balance (Pattyn and Morlighem, 2020) may not apply to the significant contemporary ice shelves draining EWS region. Although, clearly, given the rapidity of ice-shelf collapse along the Antarctic Peninsula, MICI could quickly become an important process under atmospheric and/or oceanic warming in the EWS region.

5.2 Ice-ocean-atmosphere Mechanisms Behind Observed CFL Migration

In the absence of regular calving of large, tabular icebergs, the steady advance of CFLs across the EWS region is a result of the continued sustaining flow of inland ice into the ice shelves and the relatively minor sub-annual calving occurring at their fronts. Therefore, varying rates of CFL advance are a result of internal ice-dynamical or external meteorological or oceanic factors, or a combination of both (Benn *et al.*, 2007; Baumhoer *et al.*, 2018). As contemporary CFLs approach, or pass their previous known maximum positions, as is the case for several of the EWS region ice shelves, the likelihood of new, tabular iceberg calving events increase, because the threshold of floating-ice area which can be maintained by ice-shelf internal strength is overcome in a stretching and thinning system (Pollard *et al.*, 2015). Rheological weakening due to external factors such as increasing atmospheric temperatures or changing sea-ice conditions will act to alter the likelihood and timing of calving (Benn *et al.*, 2007). The CFL, meteorological and sea-ice evidence for the influence of internal ice-dynamical and external ice-ocean-atmosphere interactions on the presented EWS CFLs, are discussed in this section.

5.2.1 Surface Air Temperatures

The effects of meteorological conditions on ice-shelf rheology have been unambiguously demonstrated by the hydrofracturing mechanisms associated with the collapse and retreat of AP ice shelves (Benn *et al.*, 2007; Pritchard and Vaughan, 2007; Scambos *et al.*, 2009). Analysis of the ERA5 meteorological data undertaken here indicates that the atmospheric warming which has been occurring in the EWS region since 1979 is comparable to that at the AP (Figure 4.8), where annual surface temperatures increased at an average 0.06°C yr^{-1} over the 50 years prior to 2005 (Turner *et al.*, 2005). However, unlike at the AP, monthly-averaged austral summer surface air temperatures remain well below 0°C and therefore, surface melting is likely non-existent or constrained to short-lived melting events which produce minimal volumes of surface meltwater. Thus, because sufficient volumes of meltwater required to cause surface ponding and hydrofracturing have not materialised, the rapid, systematic, ice-shelf retreat which has occurred along the margins of the AP over approximately the past three decades has not been realised in the EWS region. Similarly, there is no evidence in the presented CFL record of rapid CFL advance due to glacier velocity increases attributed to meltwater routing to glacier beds, a mechanism which has recently been observed at AP glaciers (Tuckett *et al.*, 2019).

5.2.2 Surface Winds

Surface air temperatures are to an extent governed by changes in surface wind speeds and so, whilst the general trend in surface air temperatures is one of warming, natural variability in wind speeds,

and the effects of large-scale, synoptic atmospheric processes on wind speeds, will also have an effect on ice-shelf surface melting. Trends in surface winds have been linked to changing hemispheric-wide atmospheric conditions, such as variations in the SAM and ENSO, in other regions around the AIS (Turner *et al.*, 2013). For example, recent research by Turner *et al.* (2016) found that surface air temperatures over the AP have in fact been decreasing since the 1990s, as a result of increased cold winds caused by the strengthening of the mid-latitude jet over the northern Weddell Sea. Therefore, the surface wind speed anomalies in an increasing north to south direction along the EWS coastline, identified here, will undoubtedly have had consequences for surface air-temperatures and associated surface melting. Nonetheless, average austral-summer surface air temperatures remain below 0°C and so, research into the potential for future ice-shelf retreat in the EWS region should focus on how variation in surface winds might increase, or act to proliferate otherwise increasing, surface air temperatures, and the large-scale atmospheric processes driving them.

5.2.3 Sea-ice Concentrations

The identified broadscale trend in increased north to south surface windspeed anomalies along the EWS coastline are likely to have facilitated the broadly increasing sea-ice concentrations in the EWS since 1979, because these winds fundamentally limit the export of seasonal sea ice north, away from the EWS (Nicholls *et al.*, 2009). Therefore, sea-ice concentrations are subject to the same atmospheric processes that govern surface windspeeds and related air temperatures, reemphasising the importance of further research into these atmospheric processes. For instance, near-record anonymously low sea-ice concentration observations in the Weddell Sea during 2016/17 contrast to the broadscale increasing sea-ice concentration trend identified here, and have been attributed to strong westerly winds facilitated by unusually deep storms during that year and the opening of the most significant polynya since the 1970s (Turner *et al.*, 2020).

The sea-ice concentration anomalies and CFLs presented in this thesis provide some evidence to suggest that changing sea-ice concentrations are facilitating CFL advance through the rheological strengthening of ice shelves. Recent research has shown how reductions in sea-ice facilitated the retreat of the AP ice-shelves, as sea-ice acts as a protective buffer to ice shelves, limiting ice-shelf flexture which eventually causes calving (Massom *et al.*, 2018). This mechanism of ice-shelf change is particularly relevant where multiyear fast ice is present, increasing the structural integrity of the ice-shelf system and preventing calving (Massom *et al.*, 2010, 2018). The concurrent increase in sea-ice concentrations with CFL advances over the past > 30 years in the EWS would suggest that the presence of sea ice is, at a minimum, limiting the rate of large, tabular, iceberg calving in the region. This is opposed to Rignot and MacAyeal's (1998) prediction that front calving might increase due to weakening fast ice at Filchner Ice Shelf, under increasing climate change. In fact, the sea-ice

concentration record at Filchner Ice Shelf front shows increasing sea-ice concentrations since the calving of Filchner Ice Shelf in 1985/86, a time when annually-averaged sea-ice concentrations were c. 10% below the long-term average and had been low (5% to 20 % below long-term average) for at least five years preceding that (Figure 4.12). The decadal-timescales over which these processes are occurring, paired with the relatively short sea-ice concentration record, ultimately means that no concrete assertions can be made to suggest that the rates of Filchner Ice Shelf calving or area expansion are directly linked to sea-ice concentrations. Therefore, continued monitoring for the next calving event of Filchner Ice Shelf and related sea-ice concentrations.

Localised, sustained, anomalously low sea-ice concentrations at the margin of Atka Ice Shelf prior to its calving in 2009 do provide some further evidence that reduced sea-ice concentrations have facilitated decreased ice-shelf structural integrity in the EWS region. The 2009 calving of Atka Ice Shelf appears to be approximately in line with the magnitude of previous calving in Ep.1, where calving of c. 3.3% and 3.6% of the glacier system (ice shelf plus drainage basin) occurred during Ep.1 and Ep.5, respectively, indicating that this calving event was probably a result of the natural calving cycle due to the ice-shelf yield-strength being overcome. However, the Ep.1 area reduction originated from the southwest portion of the ice shelf (marked X in Figure 5.1) and so the 2009 CFL reflects the furthest known seaward extent of Atka Ice Shelf's terminus, supporting a hypothesis that the presence of sea ice facilitated the maintenance of Atka Ice Shelf's structural integrity, until the sustained sea-ice reduction in the years preceding the 2009 calving. This is similar to the situation at the margins of Brunt and Stancomb-Wills ice shelves, where sea-ice may have promoted CFL advance over the past 40 years at least, but increased rifting at Brunt Ice Shelf over the past decade could be a result of reduced structural integrity due to reduced sea-ice concentrations at the ice-shelf margin (De Rydt *et al.*, 2018, 2019).

5.2.4 Oceanic Properties

Although no ocean temperature or salinity data are presented here, research from other regions of the AIS, such as the recent body of work from the Amundsen and Bellingshausen Sea Sectors (e.g. Jacobs *et al.*, 1992, 2011; Wåhlin *et al.*, 2010; Christie *et al.*, 2018), allows for some inference as to what oceanic changes might be affecting CFLs and ice-shelf extents in the EWS region. Increasing transport of relatively warm CDW to the bases and GLs of ice shelves in the AP has facilitated their rapid retreat (Cook *et al.*, 2016), but despite increased CDW transport to ice-shelf bases in the WAIS, uncertainty as to the effect of this on CFLs remain (Pritchard *et al.*, 2012; Baumhoer *et al.*, 2018) (Section 2.2.5.). The relative lack of recent ice-shelf calving in the EWS region then, would on the one hand indicate that contrary to other AIS regions, ocean temperatures are not warming, or relatively warm waters are not increasingly being transported to ice-shelf locations, and therefore, ice-shelf

strength is not being undermined to the same extent as elsewhere, by increased basal melt or by reducing basal marine ice accretion (Craven *et al.*, 2005; Pritchard *et al.*, 2012; Depoorter *et al.*, 2013b). On the other hand, increased basal melting could be facilitating reduced buttressing from thinning and ungrounding ice-shelves, resulting in CFL advances due to increased ice-flow velocities (Rintoul *et al.*, 2016). The strong correlation between sea surface temperatures and CFL retreat at the AP (Cook *et al.*, 2016) would also indicate that the CFL record shoes no evidence for sea surface warming.

The broadscale bathymetry of the EWS region (Morlighem *et al.*, 2020) (Figure 2.3) suggests that any change in CDW temperature, salinity or transportation rates would propagate relatively rapidly to the CFL record, due to the coastal route that deep water takes in the region, proximal to the continental shelf break and the relatively small distances (0 – 80 km) between the continental shelf break and ice-shelf GLs, north of Brunt Ice Shelf (Nicholls *et al.*, 2009). The maximum seaward extents of the CFLs mapped in this study align approximately with the edge of the continental shelf, supporting a theory of oceanic mechanisms of ice-shelf calving as ocean properties could be causing relatively minor calving events to the calving fronts which extend out over the continental shelf break. However, the fact that there is no evidence for an increase in significant calving events in the EWS sector over at least the past 5 decades is indicative of relatively stable ice-shelves which are not subject to basal erosion by relatively warm seawater. Furthermore, recent research has found limited CDW shoaling in the EWS region, primarily due to the large-scale cyclonic wind stress over the Weddell Sea (Schmidtko *et al.*, 2014), reemphasising the need for further research into the mechanisms behind identified changes in wind speeds.

The vulnerability of the Brunt/Stancomb-Wills ice shelf system in particular, to reduced marine ice accretion, has been highlighted by previous research, because the ice melange and fast ice material which characterise these ice shelves rely on basal marine-ice accretion to remain intact and are particular vulnerable to basal melting (Craven *et al.*, 2005; Massom *et al.*, 2010). The theory of Brunt/Stancomb-Will ice shelf instability due to oceanic ice-shelf undermelt is not necessarily supported by the ice-shelf area evidence presented here, at least not in close proximity to the CFL, because these shelves have continued their progressive advance since their minimum positions prior to 1955, when calving would have been expected under significant weakening of the ice melange. Nevertheless, the slower CFL advance rates at Brunt Ice Shelf over the past decade indicate that basal

pinning (see Section 5.2.5) is exerting more of an influence on the extent of the ice shelf than the effects of basal melting or reduced sea-ice concentrations on structural integrity.

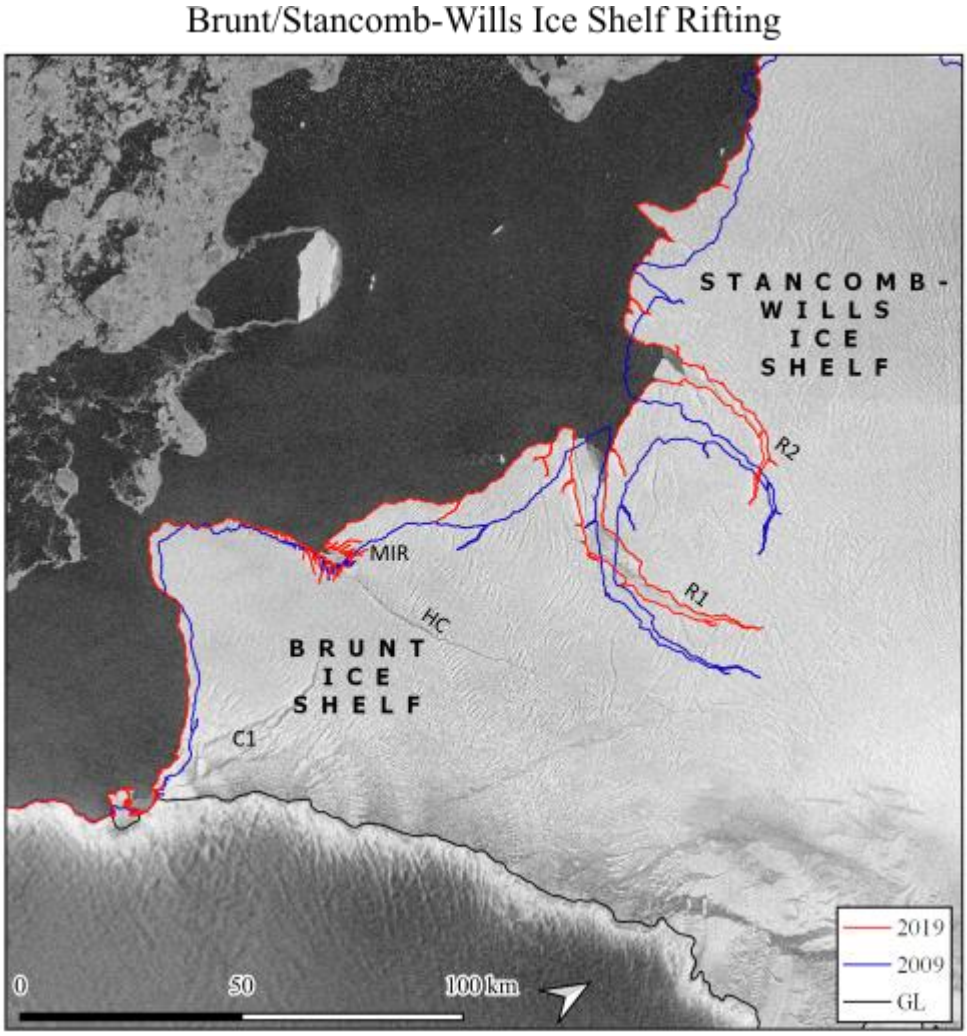

Figure 5.2: Map showing the location of two large rifts identified between Brunt and Stancomb-Wills ice shelves. Recent studies on Brunt Ice Shelf have identified rapidly extending rifts at Chasm 1 (C1) and Halloween Crack (HC). Research has found that Brunt Ice Shelf is currently pinned on a bed rise at McDonald Ice Rumples (MIR). See Figure 4.2 for location.

5.2.5 Influence of Internal Ice Dynamics and Local Bed Conditions

Beyond the available evidence for meteorological, sea-ice and oceanic drivers of ice-shelf change, there is evidence to indicate that individual ice-shelf internal dynamics, bed geometries and bed conditions are additional governing factor in CFL migration in the EWS region. For example, imminent calving has increasingly been predicted over the past decade is at Brunt and Stancomb-Will ice shelves, since their terminus positions have surpassed their previous know maximums (Anderson *et al.*, 2014; De Rydt *et al.*, 2019; Rose, 2019). However, Khazendar *et al.*'s (2009) modelling of the unique rheology of the Brunt/Stancomb-Wills ice shelf system indicates that its high stiffness means that in spite of their configurations stretching up to 250 km from the GL, rapid collapse is unlikely to occur. Furthermore, the CFL record produced here does not support Anderson *et al.*'s (2014) hypothesis of

catastrophic calving due to the rapid extension of the c. 65 km rift between the Brunt and Stancomb-Wills ice shelves (Figure 5.2). In fact, between 2009 and 2019, extension and widening of this rift was limited less than hundreds of meters. However, the anomalously high rates of CFL advance at Brunt Ice Shelf are nonetheless likely to be a result of rifting; a recent body of work highlights the novel extension of two rifts here, "Chasm 1" and "Halloween Crack" ("C1" and "HC" in Figure 5.2), since 2012 and 2016, respectively (De Rydt *et al.*, 2018, 2019; King *et al.*, 2018). Although rates of Brunt Ice Shelf CFL advance remain high when compared to other, similarly-sized ice shelves, the notable reduction in advance rate over the past decade, when compared to Ep.3 and Ep.4, is likely due to the CFL reaching a local bed pinning point of the ice front at an area known as McDonald Ice Rumples (De Rydt *et al.*, 2018; Hodgson *et al.*, 2019) ("MIR" in Figure 5.2). This example reiterates the importance of local bed topography and conditions on CFL advancement rates, in agreement with other authors who have highlighted the significance of local geometric parameters in studies of ice-shelf change (Cook and Vaughan, 2010; Lovell *et al.*, 2017; Seehaus *et al.*, 2018).

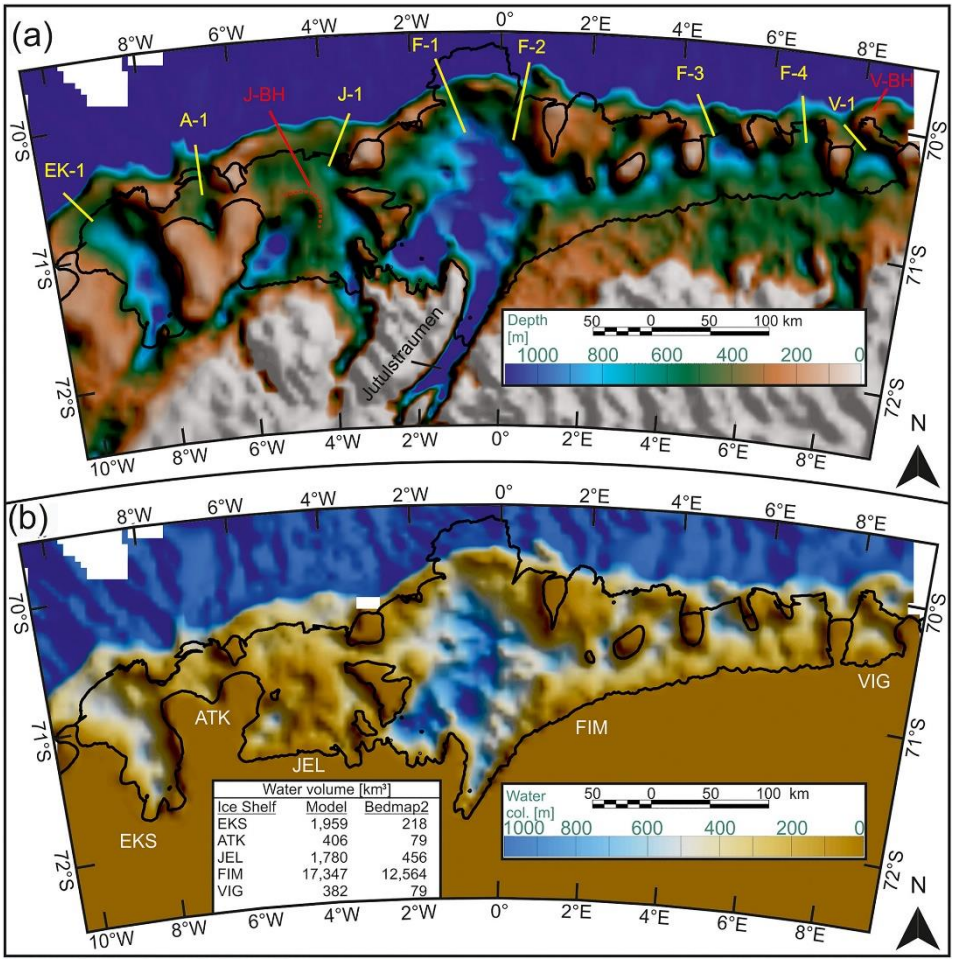

Figure 5.3: Eisermann et al.'s (2020) bathymetric modelling of the bed of the Dronninmg Maud Land ice shelves including Fimbul (FIM), Jelbart (JEL), Atka (ATK) and Ekstrom (EKS). Created using inverted gravity measurements.

Additionally, there is evidence to suggest that local bed topographical conditions exert considerable control over CFL migration at the northern EWS ice-shelves, where recent high-resolution bathymetric models produced by Eisermann *et al.* (2020) from inverted airborne gravity data, reveal a deep subglacial trough beneath Jutulstraumen Ice Stream and significant seawater cavities beneath the Fimbul, Jelbart, Atka and Ekstrøm ice shelves, bordered on the seaward (down-glacier) side by sea-bed ridges (FIGURE 5.3). One hypothesis that might explain why significant iceberg calving appears to be limited to the seaward side of the sea-bed ridges, is that the strength of these ice shelves is maintained under relatively limited basal melt due to the sea-bed ridges acting to partially block access of relatively warm CDW to the bases and GLs of these ice shelves. This mechanism of basal melt reduction has been measured at a sub-ice-shelf bed ridge beneath the much-studied Pine Island Ice Shelf in the Amundsen Sea Embayment, by an autonomous underwater vehicle (Jenkins *et al.*, 2010; Dutrieux *et al.*, 2014). The minimum mapped CFL at the Jutulstraumen Ice Stream, in 1974, the hypothesis of water-column blocking by bed-rises, as it is in approximate agreement with Eisermann *et al.*'s (2020) modelled bed-rise pinning point, suggesting that the sub-ice-shelf bathymetry may have limited the areal extent of the 1967 calving event, where the structural integrity of the ice-shelf remained high behind (landward) the ridge. This is in contrast to Filchner Ice Shelf, where the vast Filchner Trough acts as corridor for relatively warm waters to access the ice-shelf base, or even its GL some 500 km behind the calving front (Nicholls *et al.*, 2009). However, the lack of large, tabular iceberg calving from Filchner Ice Shelf over the past 35 years implies that CDW has not melted the ice-shelf base sufficiently to overcome its internal strength, albeit the natural calving cycle of Filchner Ice Shelf likely occurs over longer timescales and therefore CDW basal melt would have to be significant to cause calving at this stage in the natural calving cycle. Similar bathymetry modelling at Brunt and Stancomb-Wills Ice shelves has revealed that they are also pinned close to their termini, which may be another stabilising factor, postponing significant calving events (Hodgson *et al.*, 2019). In fact, a lack of bed pinning points in front of the Coats Land coast is probably what prevented the maintenance of a large ice-shelf in the region since the last deglaciation (Hodgson *et al.*, 2018), leaving only the relatively small glacier tongues discussed in this study.

5.2.6 Interactions Between Ice, Oceanic and Atmospheric Processes

Analysis of the available CFL, meteorological, sea-ice, oceanic, ice dynamical and bed geometry evidence discussed above indicates that ice-shelf extents and CFLs are governed by a combination of factors and interactions between them. For example, anomalous north to south wind speeds, possibly driven by changes to synoptic hemisphere-wide scale atmospheric circulation, are "trapping" sea ice in the Weddell Sea, which has limited ice-shelf calving in the region by strengthening of the ice-shelf systems (e.g. Massom *et al.*, 2010; Robel, 2017). Nonetheless, increasing sea ice in the region could

have unforeseen consequences on ice-shelf extents through other ice-ocean interactions, such as enhancing ice-shelf basal melting by increased CDW advection by Ekman transport, because sea-ice formation is a fundamental driver behind this process (Nicholls, 1997; Nicholls *et al.*, 2009). Indeed, this mechanism of ice-shelf change could be contributing to, or could in the future contribute to, GL retreat and thinning at the Brunt/Stancomb-Wills ice shelf system. If this is the case for these ice shelves and the system is in an unstable balance of thinning and weakening, ultimately rapid and/or extensive calving might be expected. However, bed geometry is an important stabilising factor through the pinning of ice-shelf fronts or bases, or by limiting CDW access to their bases and thus retarding basal melting.

Whilst this is not an exhaustive description of the processes affecting the EWS ice shelves, it does illustrate the complexities of attributing CFL migration to any one cause. Ultimately, in contrast to the AP and WAIS ice shelves, there is minimal evidence in the presented CFL record that the EWS ice shelves are behaving outwith their expected behaviour within their natural calving cycles. This is in agreement with (De Rydt *et al.*, 2019), for example, who argue that changes to the Brunt Ice Shelf are entirely being driven by ice dynamical changes, due to the relative continuity in stable meteorological conditions and theorised lack of CDW transport to this ice shelf over the past 50 years. Fundamentally, one of the main limitations of studying CFLs in isolation of dynamic GLs, thickness measurements or *in situ* sub-ice-shelf oceanic measurements, is that ice-shelf changes are a result of numerous interacting mechanisms, of which internal ice-dynamical factors can propagate up-glacier, far into the ice-sheet interior. Nevertheless, it is hoped that the datasets produced here may be used in conjunction with additional GL, sea-ice concentration, meteorological or ocean datasets in the future to draw more robust conclusions as to the causes of measured CFL advance and facilitate in wider Antarctic glaciological study.

6 Conclusion

The AIS is losing mass in increasing quantities, fuelling predictions of the potential for meter-scale contributions to global sea level rise from the ice sheet over the coming centuries, under different climate change scenarios. The most rapid and greatest-magnitude changes have so far occurred at the dynamically thinning marine-terminating glaciers and ice streams of the AP and marine-based WAIS. Uncertainties around the future contribution of mass loss from the EAIS remain, due to its significant size and the relatively modest changes which have occurred to the ice sheet despite the known atmospheric and oceanic changes occurring. Because ice shelves exert considerable control over the flow of inland ice into the ocean, studying their extents can be beneficial as an important measure of the stability of the ice sheet. Indeed, some of the greatest-magnitude contemporary changes to the AIS have been the rapid collapse of ice shelves along the AP, which have been observed over the past > 3 decades using spaceborne remote sensing instruments.

This study has applied an adapted semi-automatic digitisation method to the delineation of new coastal maps and calving front locations across the eastern Weddell Sea Sector, by passing a variety of radar and optical remotely sensed imagery through a Sobel edge extraction algorithm. These new datasets have revealed the synchronous, sustained multidecadal advance of the CFLs of the significant ice shelves which extend from the ice streams in the region, draining approximately 23% of the AIS. Where ice shelves have not expanded on annual to decadal timescales, it is due to the detachment of large, tabular icebergs; in some cases calving areas an order of magnitude larger than what has been observed at the AP or WAIS. This type of cyclical iceberg calving, which occurs over decadal timescales, is indicative of a region of ice sheet in approximate mass balance and calving from this part of the EAIS is part of the natural calving cycle. This is in stark contrast to the ongoing rapid, multidecadal retreat of ice shelves witnessed along the AP, which has unequivocally been linked to anthropogenic-caused atmospheric warming. However, the multidecadal to centennial timescales over which the calving processes in the EWS are occurring mean that any changes resulting from external forcings may take decades to show in the CFL record.

Indeed, the research presented here has found no evidence for observed atmospheric warming causing changes to ice-shelf extents, most likely because even under atmospheric warming, austral summer surface air temperatures have so far remained below 0°C. However, trends in EWS sea-ice concentrations, which are likely being driven by changes to surface winds, do indicate that sea-ice acts as important control in maintaining the structural integrity of ice shelves and therefore, reducing calving activity. If this hypothesis is correct, a continuing trend of increasing sea-ice concentrations will act to limit calving activity as the ice shelves extend towards, or beyond, their previously known maximum extents.

At Brunt and Stancomb-Wills ice shelves, where contemporary CFLs are at (Stancomb-Wills), or surpassed (Brunt) their previous know maximum positions, significant calving events are now deemed likely, especially given the anomalously low sea-ice concentrations at the margins of these ice shelves during the past decade, in contrast to the overall regional trend. Indeed, recent work has highlighted recent (since 2012) surface rifting as facilitating an imminent calving event at Brunt Ice Shelf, but the CFLs presented here show no evidence of increased surface rifting at Stancomb-Wills over the past decade. The CFL record further indicates that bed geometries are a fundamental governing factor over ice-shelf extents in the EWS region, as local bed rises can act to limit basal melting and thus, iceberg calving, through impeding the flow of CDW, or can act as pinning points, slowing ice-shelf expansion but increasing the likelihood of rifting and eventual calving due to a build-up of stress.

Ultimately, in contrast to the AP and WAIS ice shelves, no evidence is found that the EWS ice shelves are behaving outwith the expected behaviour within their natural calving cycles. Continued monitoring is required to establish whether this will remain the case under increasing air- and ocean-temperatures, changing wind patterns and varying sea-ice concentrations as a result of climate change. Furthermore, given the multidecadal timescales over which calving processes are occurring at the significant EWS region ice shelves, more robust analyses as to the drivers of ice-shelf area change, including statistical analyses, require more data points and therefore, continues CFL monitoring should remain a priority. A lack of oceanic temperature and salinity data, as well as high-resolution bathymetric studies in the region means that uncertainties remain as to the sub-ice-shelf processes occurring and how they might too change, and over what timescales, under a warming climate.

References

Alley, R.B., 2007. Effect of sedimentation on ice-sheet grounding-line stability. Science 315, 1838–1841.

Anderson, R., 2014. Halley Research Station, Antarctica: calving risks and monitoring strategies. Natural Hazards and Earth System Sciences 14, 917–927.

Assmann, K.M., 2019. Warm Circumpolar Deep Water at the Western Getz Ice Shelf Front, Antarctica. Geophysical Research Letters 46, 870–878. https://doi.org/10.1029/2018GL081354

Åström, J.A., 2014. Termini of calving glaciers as self-organized critical systems. Nature Geoscience 7, 874–878.

Bamber, J.L., 2004. Mass balance of the cryosphere. Observations and modelling contemporary and future changes. Cambridge.

Bassis, J.N., 2013. Diverse calving patterns linked to glacier geometry. Nature Geoscience 6, 833–836.

Baumhoer, C.A., 2019. Automated Extraction of Antarctic Glacier and Ice Shelf Fronts from Sentinel-1 Imagery Using Deep Learning. Remote Sensing 11, 2529.

Baumhoer, C.A., 2018. Remote Sensing of Antarctic Glacier and Ice-Shelf Front Dynamics—A Review. Remote Sensing 10, 1445.

Benn, D.I., 2007. Calving processes and the dynamics of calving glaciers. Earth-Science Reviews 82, 143–179.

Bentley, M.J., 2010. Deglacial history of the West Antarctic Ice Sheet in the Weddell Sea embayment: Constraints on past Ice volume change. Geology 38, 411–414. https://doi.org/10.1130/G30754.1

Bentley, M.J., 1998. Glacial and marine geological evidence for the ice sheet configuration in the Weddell Sea–Antarctic Peninsula region during the Last Glacial Maximum. Antarctic Science 10, 309–325. https://doi.org/10.1017/S0954102098000388

Birkenmajer, K., 1980. The last stages of Trolltunga drift in the Weddell Sea, Antarctica. Polish Polar Research 335–337.

Boening, C., 2012. Snowfall-driven mass change on the East Antarctic ice sheet. Geophysical Research Letters 39. https://doi.org/10.1029/2012GL053316

Carr, J.R., 2013. Recent progress in understanding marine-terminating Arctic outlet glacier response to climatic and oceanic forcing: Twenty years of rapid change. Progress in Physical Geography 37, 436–467.

Chen, J., 2011. A simple and effective method for filling gaps in Landsat ETM+ SLC-off images. Remote sensing of environment 115, 1053–1064.

Christie, F.D.W., 2018. Glacier change along West Antarctica's Marie Byrd Land Sector and links to inter-decadal atmosphere–ocean variability. The Cryosphere 12, 2461–2479.

Christie, F.D.W., 2016. Four-decade record of pervasive grounding line retreat along the Bellingshausen margin of West Antarctica. Geophysical Research Letters 43, 5741–5749. https://doi.org/10.1002/2016GL068972

Cook, A., 2005. Retreating glacier fronts on the Antarctic Peninsula over the past half-century. Science 308, 541–544.

Cook, A.J., 2016. Ocean forcing of glacier retreat in the western Antarctic Peninsula. Science 353, 283–286.

Cook, A.J., 2014. A new Antarctic Peninsula glacier basin inventory and observed area changes since the 1940s. Antarctic Science 26, 614–624.

Cook, A.J., 2010. Overview of areal changes of the ice shelves on the Antarctic Peninsula over the Past 50 years. The Cryosphere. 4, 77–98.

Cook, C.P., 2013. Dynamic behaviour of the East Antarctic ice sheet during Pliocene warmth. Nature Geoscience 6, 765–769.

Copernicus Climate Change Service (C3S), 2017. ERA5: Fifth generation of ECMWF atmospheric reanalyses of the global climate. Copernicus Climate Change Service Climate Data Store (CDS). https://cds.climate.copernicus.eu/cdsapp#!/home
Copernicus Sentinel data, 2020 [years: 2015, 2017 & 2019]. Retrieved from ASF DAAC. Available at: https://search.asf.alaska.edu/ [Accessed February 2020], processed by ESA.
Cornford, S.L., 2015. Century-scale simulations of the response of the West Antarctic Ice Sheet to a warming climate.
Craven, M., 2005. Borehole imagery of meteoric and marine ice layers in the Amery Ice Shelf, East Antarctica. Journal of Glaciology 51, 75–84.
Davies, B., 2012. Variable glacier response to atmospheric warming, northern Antarctic Peninsula, 1988–2009. Cryosphere 6, 1031–1048.
De Rydt, J., 2019. Calving cycle of the Brunt Ice Shelf, Antarctica, driven by changes in ice-shelf geometry. The Cryosphere 13, 2771–2787.
De Rydt, J., 2018. Recent rift formation and impact on the structural integrity of the Brunt Ice Shelf, East Antarctica. The Cryosphere 12, 505–520.
De Rydt, J., 2015. Modeling the instantaneous response of glaciers after the collapse of the Larsen B Ice Shelf. Geophysical Research Letters 42, 5355–5363.
Deb, P., 2018. Summer Drivers of Atmospheric Variability Affecting Ice Shelf Thinning in the Amundsen Sea Embayment, West Antarctica. Geophysical Research Letters 45, 4124–4133. https://doi.org/10.1029/2018GL077092
DeConto, R.M., 2016. Contribution of Antarctica to past and future sea-level rise. Nature 531, 591–597. https://doi.org/10.1038/nature17145
Depoorter, M.A., 2013a. Antarctic grounding line. In supplement to: Depoorter, MA *et al.* (2013): Calving fluxes and basal melt rates of Antarctic ice shelves. Nature, 502, 89-92, https://doi.org/10.1038/nature12567. https://doi.org/10.1594/PANGAEA.819150
Depoorter, M.A., 2013b. Calving fluxes and basal melt rates of Antarctic ice shelves. Nature 502, 89–92. https://doi.org/10.1038/nature12567
Dupont, T., 2005. Assessment of the importance of ice-shelf buttressing to ice-sheet flow. Geophysical Research Letters 32(4).
Dutrieux, P., 2014. Strong Sensitivity of Pine Island Ice-Shelf Melting to Climatic Variability. Science 343, 174–178. https://doi.org/10.1126/science.1244341
Eisermann, H., 2020. Bathymetry Beneath Ice Shelves of Western Dronning Maud Land, East Antarctica, and Implications on Ice Shelf Stability. Geophysical Research Letters 47, e2019GL086724. https://doi.org/10.1029/2019GL086724
Feldmann, J., 2015. Collapse of the West Antarctic Ice Sheet after local destabilization of the Amundsen Basin. Proceedings of the National Academy of Sciences 112, 14191–14196.
Fetterer, F., K. Knowles, W. N. Meier, M. Savoie, and A. K. Windnagel. 2017, updated daily. Sea Ice Index, Version 3. Boulder, Colorado USA. NSIDC: National Snow and Ice Data Center. doi: https://doi.org/10.7265/N5K072F8
Fountain, A.G., 2017. The changing extent of the glaciers along the western Ross Sea, Antarctica. Geology 45, 927–930.
Fox, A., 2012. SCAR Antarctic Digital Database V 6.0.
Fretwell, P., 2013. Bedmap2: improved ice bed, surface and thickness datasets for Antarctica. The Cryosphere 7, 375–393.
Frezzotti, M., 2002. 50 years of ice-front changes between the Adélie and Banzare Coasts, East Antarctica. Annals of Glaciology 34, 235–240. https://doi.org/10.3189/172756402781817897
Gardner, A. S., 2019. ITS_LIVE Regional Glacier and Ice Sheet Surface Velocities. Data archived at National Snow and Ice Data Center. [Accessed 01/06/2020] doi:10.5067/6II6VW8LLWJ7
Gardner, A.S., 2018. Increased West Antarctic and unchanged East Antarctic ice discharge over the last 7 years. The Cryosphere 12, 521–547. https://doi.org/10.5194/tc-12-521-2018

Goldberg, D., 2009. Grounding line movement and ice shelf buttressing in marine ice sheets. Journal of Geophysical Research: Earth Surface 114.
Golledge, N.R., 2015. The multi-millennial Antarctic commitment to future sea-level rise. Nature 526, 421–425.
Greene, Chad A., *et al.* "Antarctic Mapping Tools for Matlab." Computers & Geosciences, vol. 104, Elsevier BV, July 2017, pp. 151–57, doi:10.1016/j.cageo.2016.08.003.
Grizonnet, M., 2017. Orfeo ToolBox: open source processing of remote sensing images. Open Geospatial Data, Software and Standards 2, 15. https://doi.org/10.1186/s40965-017-0031-6
Gudmundsson, G.H., 2019. Instantaneous Antarctic ice-sheet mass loss driven by thinning ice shelves. Geophysical Research Letters.
Haran, T., 2018 updated 2019. MEaSUREs MODIS Mosaic of Antarctica 2013-2014 (MOA2014) Image Map, Version 1. Coastline product. Boulder, Colorado USA. NASA National Snow and Ice Data Center Distributed Active Archive Center. doi: https://doi.org/10.5067/RNF17BP824UM.
Haran, T., 2005, updated 2019. MODIS Mosaic of Antarctica 2003-2004 (MOA2004) Image Map, Version 1. Coastline product. Boulder, Colorado USA. NASA National Snow and Ice Data Center Distributed Active Archive Center. doi: https://doi.org/10.7265/N5ZK5DM5.
Helm, V., 2014. Elevation and elevation change of Greenland and Antarctica derived from CryoSat-2. The Cryosphere 8, 1539–1559.
Hillenbrand, C.-D., 2014. Reconstruction of changes in the Weddell Sea sector of the Antarctic Ice Sheet since the Last Glacial Maximum. Quaternary Science Reviews 100, 111–136.
Hillenbrand, C.-D., 2012. Marine geological constraints for the grounding-line position of the Antarctic Ice Sheet on the southern Weddell Sea shelf at the Last Glacial Maximum. Quaternary Science Reviews 32, 25–47. https://doi.org/10.1016/j.quascirev.2011.11.017
Hodgson, D.A., 2019. Past and future dynamics of the Brunt Ice Shelf from seabed bathymetry and ice shelf geometry. The Cryosphere 13, 545–556.
Hodgson, D.A., 2018. Deglaciation and future stability of the Coats Land ice margin, Antarctica. The Cryosphere 12, 2383–2399.
Holland, D., 2001. Explaining the Weddell Polynya--a large ocean eddy shed at Maud Rise. Science 292, 1697–1700.
Holland, P.R., 2010. Ice and ocean processes in the Bellingshausen Sea, Antarctica. Journal of Geophysical Research: Oceans 115. https://doi.org/10.1029/2008JC005219
Huber, J., 2017. A complete glacier inventory of the Antarctic Peninsula based on Landsat 7 images from 2000 to 2002 and other preexisting data sets. Earth system science data. 9, 115–131. https://doi.org/10.5194/essd-9-115-2017
Hughes, T., 1996. Can Ice Sheets Trigger Abrupt Climatic Change? Arctic and Alpine Research 28, 448–465. https://doi.org/10.1080/00040851.1996.12003198
Hulbe, C.L., 2005. Marine ice modification of fringing ice shelf flow. Arctic, Antarctic, and Alpine Research 37, 323–330.
Jacobs, S., 1992. Melting of ice shelves and the mass balance of Antarctica. Journal of Glaciology 38, 375–387.
Jacobs, S.S., 2011. Stronger ocean circulation and increased melting under Pine Island Glacier ice shelf. Nature Geoscience 4, 519.
Jenkins, A., 2010. Observations beneath Pine Island Glacier in West Antarctica and implications for its retreat. Nature Geoscience 3, 468–472. https://doi.org/10.1038/ngeo890
Jezek, K.C., 2002. RADARSAT-1 Antarctic Mapping Project: change-detection and surface velocity campaign. Annals of Glaciology 34, 263–268. https://doi.org/10.3189/172756402781818030
Jezek, K.C., 1999. Glaciological properties of the Antarctic ice sheet from RADARSAT-1 synthetic aperture radar imagery. Annals of Glaciology 29, 286–290.
Joughin, I., 2011. Stability of the West Antarctic ice sheet in a warming world. Nature Geoscience 4, 506.

Joughin, I., 2003. Melting and freezing beneath Filchner-Ronne Ice Shelf, Antarctica. Geophysical Research Letters 30. https://doi.org/10.1029/2003GL016941
Khazendar, A., 2009. Roles of marine ice, rheology, and fracture in the flow and stability of the Brunt/Stancomb-Wills Ice Shelf. Journal of Geophysical Research: Earth Surface 114.
Khazendar, A., 2007. Larsen B Ice Shelf rheology preceding its disintegration inferred by a control method. Geophysical Research Letters 34. https://doi.org/10.1029/2007GL030980
Kim, K., 2007. Orthorectified image mosaic of Antarctica from 1963 Argon satellite photography: image processing and glaciological applications. International Journal of Remote Sensing 28, 5357–5373. https://doi.org/10.1080/01431160601105850
Kim, K.T., 2001. Ice shelf advance and retreat rates along the coast of Queen Maud Land, Antarctica. Journal of Geophysical Research: Oceans 106, 7097–7106. https://doi.org/10.1029/2000JC000317
King, E.C., 2018. The internal structure of the Brunt Ice Shelf from ice-penetrating radar analysis and implications for ice shelf fracture. The Cryosphere 12, 3361–3372.
Klinger, T., 2011. Antarctic coastline detection using snakes. Photogrammetrie-Fernerkundung-Geoinformation 2011, 421–434.
Konrad, H., 2018. Net retreat of Antarctic glacier grounding lines. Nature Geoscience 11, 258–262. https://doi.org/10.1038/s41561-018-0082-z
Krieger, L., 2017. Automatic glacier calving front delineation on terrasar-x and sentinel-1 sar imagery. Presented at the 2017 IEEE International Geoscience and Remote Sensing Symposium (IGARSS), IEEE, pp. 2817–2820.
Lambrecht, A., 2007. New ice thickness maps of Filchner–Ronne Ice Shelf, Antarctica, with specific focus on grounding lines and marine ice. Antarctic Science 19, 521–532.
Lange, M.A., 1985. Ice Front Fluctuations in the Eastern and Southern Weddell Sea. Annals of Glaciology 6, 187–191. https://doi.org/10.3189/1985AoG6-1-187-191
Larter, R.D., 2012. Late Quaternary grounded ice extent in the Filchner Trough, Weddell Sea, Antarctica: new marine geophysical evidence. Quaternary Science Reviews 53, 111–122. https://doi.org/10.1016/j.quascirev.2012.08.006
Le Brocq, A.M., 2011. Reconstructing the Last Glacial Maximum ice sheet in the Weddell Sea embayment, Antarctica, using numerical modelling constrained by field evidence. Quaternary Science Reviews 30, 2422–2432. https://doi.org/10.1016/j.quascirev.2011.05.009
Lea, J.M., 2014. Evaluation of existing and new methods of tracking glacier terminus change. Journal of Glaciology 60, 323–332.
Liu, H., 2004. A complete high-resolution coastline of Antarctica extracted from orthorectified Radarsat SAR imagery. Photogrammetric Engineering & Remote Sensing 70, 605–616.
Liu, Y., 2015. Ocean-driven thinning enhances iceberg calving and retreat of Antarctic ice shelves. PNAS 112, 3263–3268. https://doi.org/10.1073/pnas.1415137112
Lovell, A., 2017. Sub-decadal variations in outlet glacier terminus positions in Victoria Land, Oates Land and George V Land, East Antarctica (1972–2013). Antarctic Science 29, 468–483.
Ma, Y., 2019. The Effect of Submarine Melting on Calving From Marine Terminating Glaciers. Journal of Geophysical Research: Earth Surface 124, 334–346. https://doi.org/10.1029/2018JF004820
MacGregor, J.A., 2012. Widespread rifting and retreat of ice-shelf margins in the eastern Amundsen Sea Embayment between 1972 and 2011. Journal of Glaciology 58, 458–466.
Maqueda, M., 2004. Polynya dynamics: A review of observations and modeling. Reviews of Geophysics 42.
Marshall, G.J., 2006. The impact of a changing Southern Hemisphere Annular Mode on Antarctic Peninsula summer temperatures. Journal of Climate 19, 5388–5404.
Mason, D.C., 1996. Accurate and efficient determination of the shoreline in ERS-1 SAR images. IEEE Transactions on Geoscience and Remote Sensing 34, 1243–1253.

Massom, R.A., 2018. Antarctic ice shelf disintegration triggered by sea ice loss and ocean swell. Nature 558, 383–389. https://doi.org/10.1038/s41586-018-0212-1
Massom, R.A., 2015. External influences on the Mertz Glacier Tongue (East Antarctica) in the decade leading up to its calving in 2010. Journal of Geophysical Research: Earth Surface 120, 490–506.
Massom, R.A., 2010. Examining the interaction between multi-year landfast sea ice and the Mertz Glacier Tongue, East Antarctica: Another factor in ice sheet stability? Journal of Geophysical Research: Oceans 115.
McMillan, M., 2014. Increased ice losses from Antarctica detected by CryoSat-2. Geophysical Research Letters 41, 3899–3905. https://doi.org/10.1002/2014GL060111
Mercer, J.H., 1978. West Antarctic ice sheet and CO 2 greenhouse effect: a threat of disaster. Nature 271, 321–325. https://doi.org/10.1038/271321a0
Miles, B., 2013. Synchronous terminus change of East Antarctic outlet glaciers linked to climatic forcing.
Miles, B.W., 2017. Simultaneous disintegration of outlet glaciers in Porpoise Bay (Wilkes Land), East Antarctica, driven by sea ice break-up. The Cryosphere. 11, 427–442.
Miles, B.W.J., 2016. Pan–ice-sheet glacier terminus change in East Antarctica reveals sensitivity of Wilkes Land to sea-ice changes. Science Advances 2, e1501350. https://doi.org/10.1126/sciadv.1501350
Miles, B.W.J., 2013. Rapid, climate-driven changes in outlet glaciers on the Pacific coast of East Antarctica. Nature 500, 563–566. https://doi.org/10.1038/nature12382
Miller, K.G., 2012. High tide of the warm Pliocene: Implications of global sea level for Antarctic deglaciation. Geology 40, 407–410.
Modava, M., 2017. Coastline extraction from SAR images using spatial fuzzy clustering and the active contour method. International journal of remote sensing 38, 355–370.
Mohajerani, Y., 2019. Understanding Regional Ice Sheet Mass Balance: Remote Sensing, Regional Climate Models, and Deep Learning. UC Irvine.
Morlighem, M., 2020. Deep glacial troughs and stabilizing ridges unveiled beneath the margins of the Antarctic ice sheet. Nature Geoscience 13, 132–137.
Mouginot, J., B., 2017. MEaSUREs Antarctic Boundaries for IPY 2007-2009 from Satellite Radar, Version 2. Boulder, Colorado USA. NASA National Snow and Ice Data Center Distributed Active Archive Center. doi: http://dx.doi.org/10.5067/AXE4121732AD. [Downloaded 01/03/2020]. https://nsidc.org/data/nsidc-0709/versions/2
Nicholls, K., 1997. Predicted reduction in basal melt rates of an Antarctic ice shelf in a warmer climate. Nature 388, 460.
Nicholls, K.W., 2009. Ice-ocean processes over the continental shelf of the southern Weddell Sea, Antarctica: A review. Reviews of Geophysics 47.
Nicolas, J.P., 2017. January 2016 extensive summer melt in West Antarctica favoured by strong El Niño. Nature Communications 8, 1–10. https://doi.org/10.1038/ncomms15799
Norwegian Polar Institute and Contributing Partners, 2018. Quantarctica 3.1. Available at: https://https://www.npolar.no/quantarctica/ [Accessed July 2020]. Processed by the Norwegian Polar Institute.
Oerter, H., 1992. Evidence for basal marine ice in the Filchner–Ronne ice shelf. Nature 358, 399–401. https://doi.org/10.1038/358399a0
Orfeo Toolbox 7.0.0., 2020. CNES. Available at: https://www.orfeo-toolbox.org/download/
Paolo, F., 2018. Response of Pacific-sector Antarctic ice shelves to the El Niño/Southern Oscillation. Nature geoscience 11, 121.
Paolo, F.S., 2015. Volume loss from Antarctic ice shelves is accelerating. Science 348, 327–331.
Park, J.W., 2013. Sustained retreat of the Pine Island Glacier. Geophysical Research Letters 40, 2137–2142. https://doi.org/10.1002/grl.50379

Patel, S., 2020. Changes in Antarctic coastline between 1997 and 2016 using RADARSAT and MODIS data. International Journal of Remote Sensing 41, 1389–1414. https://doi.org/10.1080/01431161.2019.1667550
Pattyn, F., 2020. The uncertain future of the Antarctic Ice Sheet. Science 367, 1331–1335. https://doi.org/10.1126/science.aaz5487
Paul, F., 2010. Optical remote sensing of glacier extent. Remote Sensing of Glaciers: Techniques for Topographic, Spatial and Thematic Mapping of Glaciers. Boca Raton: Taylor & Francis Group 137–152.
Pollard, D., 2015. Potential Antarctic Ice Sheet retreat driven by hydrofracturing and ice cliff failure. Earth and Planetary Science Letters 412, 112–121.
Pritchard, Hd., 2012. Antarctic ice-sheet loss driven by basal melting of ice shelves. Nature 484, 502.
Pritchard, H.D., 2007. Widespread acceleration of tidewater glaciers on the Antarctic Peninsula. Journal of Geophysical Research: Earth Surface 112.
Rau, F., 2004. Variations of glacier frontal positions on the northern Antarctic Peninsula. Annals of Glaciology 39, 525–530. https://doi.org/10.3189/172756404781814212
Raup, B.H., 2015. Remote sensing of glaciers, in: Remote Sensing of the Cryosphere. pp. 123–56.
Rignot, E., 2019. Four decades of Antarctic Ice Sheet mass balance from 1979–2017. Proc Natl Acad Sci USA 116, 1095. https://doi.org/10.1073/pnas.1812883116
Rignot, E., 2013. Ice-Shelf Melting Around Antarctica. Science 341, 266–270. https://doi.org/10.1126/science.1235798
Rignot, E., 2011a. Acceleration of the contribution of the Greenland and Antarctic ice sheets to sea level rise. Geophysical Research Letters 38.
Rignot, E., 2011b. Ice Flow of the Antarctic Ice Sheet. Science 333, 1427–1430. https://doi.org/10.1126/science.1208336
Rignot, E., 2002. Ice-shelf changes in Pine Island Bay, Antarctica, 1947-2000. Journal of Glaciology 48, 247–256. https://doi.org/10.3189/172756502781831386
Rignot, E., 1998. Ice-shelf dynamics near the front of the Filchner—Ronne Ice Shelf, Antarctica, revealed by SAR interferometry. Journal of Glaciology 44, 405–418. https://doi.org/10.3189/S0022143000002732
Rintoul, S.R., 2016. Ocean heat drives rapid basal melt of the Totten Ice Shelf. Science Advances 2, e1601610. https://doi.org/10.1126/sciadv.1601610
Ritz, C., 2015. Potential sea-level rise from Antarctic ice-sheet instability constrained by observations. Nature 528, 115–118.
Robel, A.A., 2017. Thinning sea ice weakens buttressing force of iceberg mélange and promotes calving. Nature Communications 8, 14596. https://doi.org/10.1038/ncomms14596
Rose, M., 2019. Automating an Antarctic Research Station, or How to do Something Hard, Really Hard!
Rott, H., 2002. Northern Larsen ice shelf, Antarctica: Further retreat after collapse. Annals of Glaciology 34, 277–282.
Rovere, A., 2014. The Mid-Pliocene sea-level conundrum: Glacial isostasy, eustasy and dynamic topography. Earth and Planetary Science Letters 387, 27–33.
Scambos, T., 2009. Ice shelf disintegration by plate bending and hydro-fracture: Satellite observations and model results of the 2008 Wilkins ice shelf break-ups. Earth and Planetary Science Letters 280, 51–60.
Scambos, T., 2003. Climate-induced ice shelf disintegration in the Antarctic Peninsula. Antarctic Peninsula Climate Variability: Historical and Paleoenvironmental Perspectives, Antarct. Res. Ser 79, 79–92.
Scambos, T.A., 2007. MODIS-based Mosaic of Antarctica (MOA) data sets: Continent-wide surface morphology and snow grain size. Remote Sensing of Environment 111, 242–257.
Scambos, T.A., 2004. Glacier acceleration and thinning after ice shelf collapse in the Larsen B embayment, Antarctica. Geophysical Research Letters 31.

Scambos, T.A., 1996. Images of Antarctic Ice Shelves. AVRHH [Image captured 13/12/2000]. Boulder, Colorado USA: National Snow and Ice Data Center. http://dx.doi.org/10.7265/N5NC5Z4N. [Accessed 22/06/2020].
SCAR Secretariat (1992, updated 2014 and 2017). Composite Gazetteer of Antarctica, Scientific Committee on Antarctic Research.
SCAR (1992, updated 2014 and 2017). Composite Gazetteer of Antarctica, Scientific Committee on Antarctic Research.
Schmidtko, S., 2014. Multidecadal warming of Antarctic waters. Science 346, 1227–1231. https://doi.org/10.1126/science.1256117
Schoof, C., 2007. Ice sheet grounding line dynamics: Steady states, stability, and hysteresis. Journal of Geophysical Research: Earth Surface 112. https://doi.org/10.1029/2006JF000664
Scott, R.C., 2018. Meteorological Drivers and Large-Scale Climate Forcing of West Antarctic Surface Melt. J. Climate 32, 665–684. https://doi.org/10.1175/JCLI-D-18-0233.1
Seale, A., 2011. Ocean forcing of the Greenland Ice Sheet: Calving fronts and patterns of retreat identified by automatic satellite monitoring of eastern outlet glaciers. Journal of Geophysical Research: Earth Surface 116(F3).
Seehaus, T., 2018. Changes in glacier dynamics in the northern Antarctic Peninsula since 1985. The cryosphere. 12, 577–594.
Shepherd, A., 2019. Trends in Antarctic Ice Sheet Elevation and Mass. Geophysical Research Letters 46, 8174–8183. https://doi.org/10.1029/2019GL082182
Shepherd, A., 2018. Mass balance of the Antarctic Ice Sheet from 1992 to 2017. Nature 558, 219–222.
Shepherd, A., 2010. Recent loss of floating ice and the consequent sea level contribution. Geophysical Research Letters 37.
Shepherd, A., 2007. Recent sea-level contributions of the Antarctic and Greenland ice sheets. science 315, 1529–1532.
Siegert, M.J., 2019. Major Ice Sheet Change in the Weddell Sea Sector of West Antarctica Over the Last 5,000 Years. Reviews of Geophysics 57, 1197–1223. https://doi.org/10.1029/2019RG000651
Sohn, H.-G., 1999. Mapping ice sheet margins from ERS-1 SAR and SPOT imagery. International Journal of Remote Sensing 20, 3201–3216.
Sørli, S.H., 2016. Ice sheet dynamics in the Brunt Basin, Weddell Sea, Antarctica, since the last glacial period.
Steig, E.J., 2012. Tropical forcing of Circumpolar Deep Water Inflow and outlet glacier thinning in the Amundsen Sea Embayment, West Antarctica. Annals of Glaciology 53, 19–28. https://doi.org/10.3189/2012AoG60A110
Stocker, T.F., 2013. Climate change 2013: The physical science basis. Contribution of working group I to the fifth assessment report of the intergovernmental panel on climate change 1535.
Stolldorf, T., 2012. LGM ice sheet extent in the Weddell Sea: evidence for diachronous behavior of Antarctic Ice Sheets. Quaternary Science Reviews 48, 20–31.
Swithinbank, C., 1988. Satellite image atlas of glaciers of the world - Antarctica. Unites States Government Printing Office.
Swithinbank, C., 1986. Multispectral digital image mapping of Antarctic ice features. Annals of glaciology 8, 159–163.
Thoma, M., 2008. Modelling Circumpolar Deep Water intrusions on the Amundsen Sea continental shelf, Antarctica. Geophysical Research Letters 35. https://doi.org/10.1029/2008GL034939
Thoma, M., 2006. Impact of the Eastern Weddell Ice Shelves on water masses in the eastern Weddell Sea. Journal of Geophysical Research: Oceans 111.
Thomas, R.H., 1973. The dynamics of the Brunt Ice Shelf, Coats Land, Antarctica. British Antarctic Survey.

Torres, R., 2012. GMES Sentinel-1 mission. Remote Sensing of Environment, The Sentinel Missions - New Opportunities for Science 120, 9–24. https://doi.org/10.1016/j.rse.2011.05.028
Tuckett, P.A., 2019. Rapid accelerations of Antarctic Peninsula outlet glaciers driven by surface melt. Nature Communications 10, 4311. https://doi.org/10.1038/s41467-019-12039-2
Turner, J., 2020. Recent Decrease of Summer Sea Ice in the Weddell Sea, Antarctica. Geophysical Research Letters 47, e2020GL087127. https://doi.org/10.1029/2020GL087127
Turner, J., 2017. Atmosphere-ocean-ice interactions in the Amundsen Sea Embayment, West Antarctica. Reviews of Geophysics 55, 235–276. https://doi.org/10.1002/2016RG000532
Turner, J., 2016. Absence of 21st century warming on Antarctic Peninsula consistent with natural variability. Nature 535, 411–415. https://doi.org/10.1038/nature18645
Turner, J., 2013. The amundsen sea low. International Journal of Climatology 33, 1818–1829.
Turner, J., 2005. Antarctic climate change during the last 50 years. International Journal of Climatology 25, 279–294. https://doi.org/10.1002/joc.1130
USGS, 2020. Landsat data [years: 2009, 2011, 2013, 2015, 2017 & 2019]. Retrieved from USGS Earth Explorer. Available at: https://earthexplorer.usgs.gov/ [Accessed February 2020], processed by USGS.
Van den Broeke, M.R., 2016. On the recent contribution of the Greenland ice sheet to sea level change. The Cryosphere 10, 1933–1946.
Van der Veen, C., 2002. Calving glaciers. Progress in Physical Geography 26, 96–122.
Van Der Veen, C., 1996. Tidewater calving. Journal of Glaciology 42, 375–385.
Vaughan, D.G., 2002. Risk estimation of collapse of the West Antarctic Ice Sheet. Climatic Change 52, 65–91.
Wåhlin, A., 2010. Inflow of warm Circumpolar Deep Water in the central Amundsen shelf. Journal of Physical Oceanography 40, 1427–1434.
Walker, D.P., 2007. Oceanic heat transport onto the Amundsen Sea shelf through a submarine glacial trough. Geophysical Research Letters 34. https://doi.org/10.1029/2006GL028154
Weertman, J., 1974. Stability of the Junction of an Ice Sheet and an Ice Shelf. Journal of Glaciology 13, 3–11. https://doi.org/10.3189/S0022143000023327
Williams, R.S., 1995. Coastal-change and glaciological maps of Antarctica. Annals of Glaciology 21, 284–290. https://doi.org/10.3189/S0260305500015950
Worsely, F., 1921. Track of Endurance 1914-15 in the Weddell Sea. Sketch Survey Map C 8421.
Wu, S.Y., 2003. Towards an automated ocean feature detection, extraction and classification scheme for SAR imagery. International Journal of Remote Sensing 24, 935–951. https://doi.org/10.1080/01431160210144606
Wuite, J., 2019. Sub-Annual Calving Front Migration, Area Change and Calving Rates from Swath Mode CryoSat-2 Altimetry, on Filchner-Ronne Ice Shelf, Antarctica. Remote Sensing 11, 2761. https://doi.org/10.3390/rs11232761
Zemp, M., 2019. Global glacier mass changes and their contributions to sea-level rise from 1961 to 2016. Nature 568, 382–386.
Zhang, E., 2019. Automatically delineating the calving front of Jakobshavn Isbræ from multitemporal TerraSAR-X images: a deep learning approach. The Cryosphere 13, 1729–1741.
Zwally, H.J., 2012. Antarctic and Greenland Drainage Systems. GSFC Cryospheric Sciences Laboratory.

Appendix I: Delineated CFLs Attribute Table

ID	Platform	Sensor	Qual_flag 1	AUTH_ID	Sector	Notes	Year	Descrip	Length (m)	DigErr (m)	CoRegErr (m)	TotalErr (m)
1	Landsat 7	ETM+	1	NAH	Berkner Island	Some use of semi-automatic edge detection. Use of overlapping neighbouring scene to fill data gaps in Landsat scene	2009	LE07_L1GT_191116_20090214_20161222_01_T2_B8	64816	18.71	77.85	96.56
2	Landsat 7	ETM+	2	NAH	Filchner Ice Shelf	Some uncertainty in the area where teh ice shelf joins the island	2009	LE07_L1GT_189116_20090115_20161223_01_T2_B8	51234	34.82	77.85	112.67
3	Landsat 7	ETM+	1	NAH	Filchner Ice Shelf		2009	LE07_L1GT_188116_20090209_20161222_01_T2_B8	229268	34.82	77.85	112.67
4	Landsat 7	ETM+	1	NAH	Coats Land	Some use of semi-automatic edge detection	2009	LE07_L1GT_184116_20090128_20161222_01_T2_B8	253874	18.71	77.85	96.56
5	Landsat 7	ETM+	1	NAH	Coats Land	Some use of semi-automatic edge detection	2009	LE07_L1GT_184115_20090128_20161222_01_T2_B8	56846	18.71	77.85	96.56
6	Landsat 7	ETM+	2	NAH	Coats Land	Uncertainty over data gaps in Landsat scene	2009	LE07_L1GT_185115_20081202_20161223_01_T2_B8	16619	34.82	77.85	112.67
7	Landsat 7	ETM+	1	NAH	Coats Land	Extensive use of semi-automatic edge detection	2009	LE07_L1GT_184115_20090213_20161223_01_T2_B8	139720	10.65	77.85	88.50
8	Landsat 7	ETM+	1	NAH	Coats Land	Extensive use of semi-automatic edge detection	2009	LE07_L1GT_184114_20090213_20161222_01_T2_B8	35835	10.65	77.85	88.50
9	Landsat 7	ETM+	1	NAH	Coats Land	Extensive use of semi-automatic edge detection	2009	LE07_L1GT_183114_20090105_20161223_01_T2_B8	69788	10.65	77.85	88.50
10	Landsat 7	ETM+	1	NAH	Brunt_Stancomb Ice Shelf	Extensive use of semi-automatic edge detection	2009	LE07_L1GT_184114_20090213_20161222_01_T2_B8	178910	10.65	77.85	88.50

11	Landsat 7	ETM+	2	NAH	Brunt_Stancomb Ice Shelf	Uncertainty over data gaps in Landsat scene, unable to be cross-referenced to neighbouring scenes due to cloud cover. Also some uncertainty arouns crack/crevasses in the ice shelf due to snow cover	2009	LE07_L1GT_184113_20090213_20161222_01_T2_B8	291142	34.82	77.85	112.67
12	Landsat 7	ETM+	1	NAH	Brunt_Stancomb Ice Shelf	Extensive use of semi-automatic edge detection	2009	LE07_L1GT_184113_20090213_20161222_01_T2_B8	94349	10.65	77.85	88.50
13	Landsat 7	ETM+	1	NAH	Brunt_Stancomb Ice Shelf		2009	LE07_L1GT_185113_20081202_20161224_01_T2_B8	96068	34.82	77.85	112.67
14	Landsat 7	ETM+	2	NAH	Brunt_Stancomb Ice Shelf	Difficult to tell exact coastline in areas of heavy crevasses/melange. Data gaps in Landsat scene; linear interpolation	2009	LE07_L1GT_184113_20090213_20161222_01_T2_B8	630357	34.82	77.85	112.67
15	Landsat 7	ETM+	1	NAH	Riisner-Larsen Ice Shelf	Extensive use of semi-automatic edge detection, but with straight-line interpolation over data gaps in Landsat scene	2009	LE07_L1GT_184112_20090213_20161222_01_T2_B8	141147	10.65	77.85	88.50
16	Landsat 7	ETM+	1	NAH	Riisner-Larsen Ice Shelf		2009	LE07_L1GT_184111_20090213_20161222_01_T2_B8	129063	34.82	77.85	112.67
17	Landsat 7	ETM+	1	NAH	Riisner-Larsen Ice Shelf	Use of neighbouring/overlapping scene to interpolate over data gaps in Landsat scene	2009	LE07_L1GT_183111_20090206_20161222_01_T2_B8	361776	34.82	77.85	112.67
18	Landsat 7	ETM+	1	NAH	Riisner-Larsen Ice Shelf	Extenisve use of semi-automatic edge detection. Use of neighbouring/overlapping scene to interpolate over data gaps in Landsat scene	2009	LE07_L1GT_182111_20090215_20161222_01_T2_B8	261342	10.65	77.85	88.50
19	Landsat 7	ETM+	1	NAH	Riisner-Larsen Ice Shelf	Some use of semi-automatic edge detection	2009	LE07_L1GT_180111_20090217_20161222_01_T2_B8	121270	18.71	77.85	96.56

20	Landsat 7	ETM+	1	NAH	Cape Norvegia	Extensive use of semi-automatic edge detecion. Interpolation over data gaps in Landsat scene using neighbouring/overlapping scene	2009	LE07_L1GT_180110_20090217_20161222_01_T2_B8	48189	10.65	77.85	88.50
21	Landsat 7	ETM+	2	NAH	Quar Ice Shelf	Some minor cloud cover. Interpolation over data gaps in Landsat scene due to cloud cover in neighbouring/overlapping scenes	2009	LE07_L1GT_181110_20090208_20161222_01_T2_B8	102385	34.82	77.85	112.67
22	Landsat 7	ETM+	1	NAH		Semi-automatic edge detection	2009	LE07_L1GT_180110_20090217_20161222_01_T2_B8	11164	18.71	77.85	96.56
23	Landsat 7	ETM+	2	NAH	Ekstrom Ice Shelf	Data gaps in Landsat 7 scene	2009	LE07_L1GT_181110_20090208_20161222_01_T2_B8	86487	34.82	77.85	112.67
24	Landsat 7	ETM+	1	NAH	Ekstrom Ice Shelf	Some use of semi-automatic edge detection. Data gaps in Landsat scene interpolated over using neighbouring/overlapping scene	2009	LE07_L1GT_180110_20090217_20161222_01_T2_B8	140666	18.71	77.85	96.56
25	Landsat 7	ETM+	1	NAH	Atka Ice Shelf	Some use of semi-automatic edge detection. Data gaps in Landsat scene interpolated over using neighbouring/overlapping scene	2009	LE07_L1GT_179110_20090210_20161223_01_T2_B8	39613	18.71	77.85	96.56
26	Landsat 7	ETM+	2	NAH	Jelbart Ice Shelf	Some use of semi-automatic edge detection. Data gaps in Landsat scene interpolated over using neighbouring/overlapping scene	2009	LE07_L1GT_177110_20090212_20161222_01_T2_B8	268121	18.71	77.85	96.56
27	Landsat 7	ETM+	1	NAH	Jelbart Ice Shelf	Extensive use of semi-automatic edge detection	2009	LE07_L1GT_176110_20090221_20161222_01_T2_B8	104583	10.65	77.85	88.50

28	Landsat 7	ETM+	1	NAH	Fimbul Ice Shelf	Some use of semi-automatic edge detection	2009	LE07_L1GT_169109_20090220_20161222_01_T2_B8	115577	18.71	77.85	96.56
29	Landsat 7	ETM+	1	NAH	Fimbul Ice Shelf	Extensive use of semi-automatic edge detection. Use of neighbouring/overlapping scenes to cross-check interpolation over data gaps in Landsat scene	2009	LE07_L1GT_176109_20090221_20161222_01_T2_B8	21572	10.65	77.85	88.50
30	Landsat 7	ETM+	1	NAH	Fimbul Ice Shelf	Extensive use of semi-automatic edge detection	2009	LE07_L1GT_170109_20090110_20161223_01_T2_B8	124779	10.65	77.85	88.50
31	Landsat 7	ETM+	2	NAH	Fimbul Ice Shelf	Extensive use of semi-automatic edge detection. Uncertainty over data gaps in Landsat scene as neighbouring scenes had cloud cover	2009	LE07_L1GT_172109_20090225_20161223_01_T2_B8	322931	10.65	77.85	88.50
32	Landsat 7	ETM+	2	NAH	Fimbul Ice Shelf		2009	LE07_L1GT_174109_20090311_20161221_01_T2_B8	281836	34.82	77.85	112.67
33	Landsat 7	ETM+	1	NAH	Fimbul Ice Shelf	Some use of semi-automatic edge detection. Interpolation over data gaps in landsat scene using data from neighbouring/overlapping scenes. Thin cloud cover, but not prohibitive to (semi-automatic) mapping	2009	LE07_L1GT_175109_20090113_20161223_01_T2_B8	171461	18.71	77.85	96.56
34	Landsat 7	ETM+	1	NAH	Fimbul Ice Shelf	Interpolation over data gaps in Landsat scene using neighbouring/overlapping scene	2009	LE07_L1GT_174109_20090311_20161221_01_T2_B8	54470	34.82	77.85	112.67

35	Landsat 7	ETM+	2	NAH	Fimbul Ice Shelf	Thin cloud layer over scene. Some use of semi-automatic edge detection. Interpolation over Landsat scene data gaps using neighbouring/overlapping scene	2009	LE07_L1GT_175109_20090113_20161223_01_T2_B8	161224	18.71	77.85	96.56
36	Landsat 7	ETM+	1	NAH	Blåskimen Island	Extensive use of semi-automatic edge detection	2009	LE07_L1GT_176110_20090221_20161222_01_T2_B8	39572	10.65	77.85	88.50
37	Landsat 7	ETM+	1	NAH	Fimbul Ice Shelf	Extensive use of semi-automatic edge detection	2009	LE07_L1GT_176110_20090221_20161222_01_T2_B8	3539	10.65	77.85	88.50
38	Landsat 7	ETM+	2	NAH	Unneruskollen Island	Some use of semi-automatic edge detection. Data gaps in Landsat scene interpolated over using neighbouring/overlapping scene	2009	LE07_L1GT_177110_20090212_20161222_01_T2_B8	27439	18.71	77.85	96.56
39	Landsat 7	ETM+	2	NAH	Atka Ice Shelf	Some use of semi-automatic edge detection. Data gaps in Landsat scene interpolated over using neighbouring/overlapping scene	2009	LE07_L1GT_177110_20090212_20161222_01_T2_B8	126201	18.71	77.85	96.56
40	Landsat 7	ETM+	1	NAH	Ekstrom Ice Shelf	Some use of semi-automatic edge detection. Data gaps in Landsat scene interpolated over using neighbouring/overlapping scene	2009	LE07_L1GT_179110_20090210_20161223_01_T2_B8	15779	18.71	77.85	96.56
41	Landsat 7	ETM+	2	NAH		Data gaps in Landsat 7 scene	2009	LE07_L1GT_181110_20090208_20161222_01_T2_B8	8101	34.82	77.85	112.67
42	Landsat 7	ETM+	2	NAH		Some minor cloud cover. Interpolation over data gaps in Landsat scene due to cloud cover in neighbouring/overlapping scenes	2009	LE07_L1GT_181110_20090208_20161222_01_T2_B8	1401	34.82	77.85	112.67

43	Landsat 7	ETM+	1	NAH	Cape Norvegia	Some use of semi-automatic edge detection	2009	LE07_L1GT_180111_20090217_20161222_01_T2_B8	22039	18.71	77.85	96.56
44	Landsat 7	ETM+	1	NAH	Lyddan Island	Extensive use of semi-automatic edge detection, but with straight-line interpolation over data gaps in Landsat scene	2009	LE07_L1GT_184112_20090213_20161222_01_T2_B8	86801	10.65	77.85	88.50
45	Landsat 7	ETM+	1	NAH	Brunt_Stancomb Ice Shelf	Extensive use of semi-automatic edge detection, but with straight-line interpolation over data gaps in Landsat scene	2009	LE07_L1GT_184112_20090213_20161222_01_T2_B8	6274	10.65	77.85	88.50
46	Landsat 7	ETM+	1	NAH	Brunt_Stancomb Ice Shelf	Extensive use of semi-automatic edge detection	2009	LE07_L1GT_183114_20090105_20161223_01_T2_B8	49603	10.65	77.85	88.50
47	Landsat 7	ETM+	1	NAH	Filchner Ice Shelf	Some use of semi-automatic edge detection	2009	LE07_L1GT_184116_20090128_20161222_01_T2_B8	45892	18.71	77.85	96.56
48	Landsat 7	ETM+	2	NAH	Berkner Island	Some uncertainty in the area where teh ice shelf joins the island	2009	LE07_L1GT_189116_20090115_20161223_01_T2_B8	45009	34.82	77.85	112.67
49	Landsat 7	ETM+	1	NAH	Berkner Island	Use of semi-automatic edge detection.	2011	LE07_L1GT_191116_20110220_20161211_01_T2_B8	63911	18.71	77.85	96.56
50	Landsat 7	ETM+	1	NAH	Filchner Ice Shelf	Some use of semi0automatic edge detection. Interpolation over data gaps in Landsat 8 scene using the neighbouring scene.	2011	LE07_L1GT_189116_20110206_20161210_01_T2_B8	243900	18.71	77.85	96.56
51	Landsat 7	ETM+	1	NAH	Coats Land	Some use of semi-automatic edge detection. A few small areas in shade and therefore unable to distinguish the exact loaction of ice front; uncertainty a few hundred meters.	2011	LE07_L1GT_185116_20110210_20161210_01_T2_B8	194253	18.71	77.85	96.56
52	Landsat 7	ETM+	1	NAH	Coats Land	Some use of semi-automatic edge detection. Some very small areas of thin cloud cover.	2011	LE07_L1GT_185115_20110210_20161210_01_T2_B8	87025	18.71	77.85	96.56

53	Landsat 7	ETM+	1	NAH	Coats Land	Some use of semi-automatic edge detection, especially in reas with no sea ice.	2011	LE07_L1GT_184115_20110219_20161211_01_T2_B8	147220	18.71	77.85	96.56
54	Landsat 7	ETM+	1	NAH	Coats Land	Use of semi-automatic edge detection	2011	LE07_L1GT_184114_20110219_20161210_01_T2_B8	37499	18.71	77.85	96.56
55	Landsat 7	ETM+	1	NAH	Coats Land	Use of semi-automatic edge detection	2011	LE07_L1GT_183114_20110228_20161210_01_T2_B8	99058	18.71	77.85	96.56
56	Landsat 7	ETM+	1	NAH	Brunt_Stancomb Ice Shelf	Exclusive use of semi-automatic edge detection	2011	LE07_L1GT_184114_20110219_20161210_01_T2_B8	37036	2.60	77.85	80.45
57	Landsat 7	ETM+	1	NAH	Brunt_Stancomb Ice Shelf	Overlay of neighbouring scene to interpolate over data gaps in Landsat scene	2011	LE07_L1GT_183114_20110228_20161210_01_T2_B8	29494	34.82	77.85	112.67
58	Landsat 7	ETM+	1	NAH	Brunt_Stancomb Ice Shelf	Some minor areas of thin cloud cover, but not prohibitive to mapping. Some use of semi-automatic edge detection	2011	LE07_L1GT_184114_20110219_20161210_01_T2_B8	128508	18.71	77.85	96.56
59	Landsat 7	ETM+	1	NAH	Brunt_Stancomb Ice Shelf		2011	LE07_L1GT_183114_20110228_20161210_01_T2_B8	25300	34.82	77.85	112.67
60	Landsat 7	ETM+	2	NAH	Brunt_Stancomb Ice Shelf	Since the ice shelf appears to be made up of a collection of compacted icebergs it is difficult in paces to loacte the "edge" of the crevasse/crack.	2011	LE07_L1GT_183113_20110228_20161210_01_T2_B8	114242	34.82	77.85	112.67
61	Landsat 7	ETM+	1	NAH	Brunt_Stancomb Ice Shelf	Extensive use of semi-automatic edge detection. Some small areas of thin cloud cover.	2011	LE07_L1GT_184113_20110219_20161210_01_T2_B8	69944	10.65	77.85	88.50
62	Landsat 7	ETM+	1	NAH	Brunt_Stancomb Ice Shelf	Some use of semi-automatic edge detection	2011	LE07_L1GT_184113_20110219_20161210_01_T2_B8	42799	18.71	77.85	96.56
63	Landsat 7	ETM+	2	NAH	Brunt_Stancomb Ice Shelf	Interpolation over data gaps in Landsat scene with help from neighbouring scene. Difficult to tell the exact edge of the crack in some places	2011	LE07_L1GT_183113_20110228_20161210_01_T2_B8	132492	34.82	77.85	112.67

64	Landsat 7	ETM+	1	NAH	Brunt_Stancomb Ice Shelf	Extensive use of semi-automatic edge detection.	2011	LE07_L1GT_183113_20110228_20161210_01_T2_B8	111010	10.65	77.85	88.50
65	Landsat 7	ETM+	2	NAH	Brunt_Stancomb Ice Shelf	Very difficult to distinguish between sea ice and ice shelf in this area. Some use of semi-automatic edge detection.	2011	LE07_L1GT_183113_20110228_20161210_01_T2_	267397	18.71	77.85	96.56
66	Landsat 7	ETM+	3	NAH	Brunt_Stancomb Ice Shelf	Cloud covered, but coastline mainly visible; some interpolation needed where coastline not entirely visible (max c. 2km)	2011	LE07_L1GT_185113_20110109_20161210_01_T2_B8	65779	34.82	77.85	112.67
67	Landsat 7	ETM+	1	NAH	Brunt_Stancomb Ice Shelf	Some use of semi-automatic edge detection	2011	LE07_L1GT_184113_20110219_20161210_01_T2_B8	157855	18.71	77.85	96.56
68	Landsat 7	ETM+	2	NAH	Brunt_Stancomb Ice Shelf	Interpolation over data gaps in Landsat scene cross-checked to neighbouring scene, coving the same area	2011	LE07_L1GT_183113_20110228_20161210_01_T2_B8	149979	34.82	77.85	112.67
69	Landsat 7	ETM+	1	NAH	Lyddan Island	Exclusive use of semi-automatic edge detection as very minimal sea ice	2011	LE07_L1GT_183113_20110228_20161210_01_T2_	33839	2.60	77.85	80.45
70	Landsat 7	ETM+	1	NAH	Riisner-Larsen Ice Shelf	Extensive use of semi-automatic edge detection. Use of neighbouring scene to interpolate over data gaps in Landsat scene.	2011	LE07_L1GT_183112_20110228_20161209_01_T2_B8	276641	10.65	77.85	88.50
71	Landsat 7	ETM+	1	NAH	Riisner-Larsen Ice Shelf	Extensive use of semi-automatic edge detection, especially since minimal sea ice	2011	LE07_L1GT_183111_20110228_20161209_01_T2_B8	358664	10.65	77.85	88.50
72	Landsat 7	ETM+	1	NAH	Riisner-Larsen Ice Shelf	Extensive use of semi-automatic edge detection. Some small areas of thin cloud cover.	2011	LE07_L1GT_182111_20110221_20161210_01_T2_B8	137792	10.65	77.85	88.50
73	Landsat 7	ETM+	1	NAH	Riisner-Larsen Ice Shelf	Some use of semi-automatic edge extraction	2011	LE07_L1GT_180111_20110223_20161210_01_T2_B8	144703	18.71	77.85	96.56
74	Landsat 7	ETM+	1	NAH	Riisner-Larsen Ice Shelf	Extensive use of semi-automatic edge detection.	2011	LE07_L1GT_181111_20110302_20161209_01_T2_B8	76730	10.65	77.85	88.50

75	Landsat 7	ETM+	2	NAH	Cape Norvegia	Interpolation over data gaps using neighbouring scene, which, although cloud-covered, clearly showed the coastline once the contrast was changed	2011	LE07_L1GT_179111_20110216_20161210_01_T2_B8	39984	34.82	77.85	112.67
76	Landsat 7	ETM+	1	NAH	Quar Ice Shelf	Extensive use of semi-automatic edge detection	2011	LE07_L1GT_180110_20110223_20161211_01_T2_B8	104528	10.65	77.85	88.50
77	Landsat 7	ETM+	1	NAH	Ekstrom Ice Shelf	Extensive use of semi-automatic edge detection	2011	LE07_L1GT_179110_20110115_20161211_01_T2_B8	238604	10.65	77.85	88.50
78	Landsat 7	ETM+	1	NAH	Atka Ice Shelf	Extensive use of semi-automatic edge detection	2011	LE07_L1GT_178110_20110124_20161210_01_T2_B8	110194	10.65	77.85	88.50
79	Landsat 7	ETM+	2	NAH	Jelbart Ice Shelf	Some use of semi-automatic edge detection. Snow cover making exact ice front difficult to spot.	2011	LE07_L1GT_177110_20110117_20161210_01_T2_B8	81014	18.71	77.85	96.56
80	Landsat 7	ETM+	1	NAH	Jelbart Ice Shelf	Interpolation over data gaps in Landsat scene cross-checked against neighbouring scene.	2011	LE07_L1GT_177110_20110101_20161211_01_T2_B8	221741	34.82	77.85	112.67
81	Landsat 7	ETM+	1	NAH	Jelbart Ice Shelf	Some use of semi-automatic edge detection. Some thin cloud cover, but coastline visible.	2011	LE07_L1GT_176110_20110315_20161209_01_T2_B8	98627	18.71	77.85	96.56
82	Landsat 7	ETM+	1	NAH	Fimbul Ice Shelf	Some use of semi-automatic edge detection	2011	LE07_L1GT_171109_20110123_20161211_01_T2_B8	137164	18.71	77.85	96.56
83	Landsat 7	ETM+	2	NAH	Fimbul Ice Shelf	Some cloud cover in places. Inrerpolation across landsat data gaps using neighbouring scenes to cross-check	2011	LE07_L1GT_174110_20110301_20161209_01_T2_B8	111690	34.82	77.85	112.67
84	Landsat 7	ETM+	1	NAH	Fimbul Ice Shelf	Use of neighbouring/overlapping scenes to interpolate over data gaps in Landsat scene. Some use of semi-automatic edge detection	2011	LE07_L1GT_170109_20101231_20161211_01_T2_B8	188415	18.71	77.85	96.56

85	Landsat 7	ETM+	1	NAH	Fimbul Ice Shelf	Some use of semi-automatic edge detection, where ses-ice free.	2011	LE07_L1GT_169109_20101208_20161211_01_T2_B8	82121	18.71	77.85	96.56
86	Landsat 7	ETM+	2	NAH	Fimbul Ice Shelf	Snow cover making exact ice front deliniation uncertain	2011	LE07_L1GT_172109_20110303_20161209_01_T2_B8	87513	34.82	77.85	112.67
87	Landsat 7	ETM+	1	NAH	Fimbul Ice Shelf		2011	LE07_L1GT_173109_20110105_20161210_01_T2_B8	93477	34.82	77.85	112.67
88	Landsat 7	ETM+	2	NAH	Fimbul Ice Shelf	Some cloud cover and data gaps in Landsat scene creating uncertainty.	2011	LE07_L1GT_174109_20110301_20161209_01_T2_B8	468457	34.82	77.85	112.67
89	Landsat 7	ETM+	1	NAH	Fimbul Ice Shelf		2011	LE07_L1GT_173109_20110310_20161209_01_T2_B8	67186	34.82	77.85	112.67
90	Landsat 7	ETM+	1	NAH		Extensive use of semi-automatic edge detection	2011	LE07_L1GT_180110_20110223_20161211_01_T2_B8	20559	10.65	77.85	88.50
91	Landsat 7	ETM+	1	NAH	Berkner Island	Some use of semi0automatic edge detection. Interpolation over data gaps in Landsat 8 scene using the neighbouring scene.	2011	LE07_L1GT_189116_20110206_20161210_01_T2_B8	44442	18.71	77.85	96.56
92	Landsat 7	ETM+	1	NAH	Filchner Ice Shelf	Some use of semi-automatic edge detection. A few small areas in shade and therefore unable to distinguish the exact loaction of ice front; uncertainty a few hundred meters.	2011	LE07_L1GT_185116_20110210_20161210_01_T2_B8	119095	18.71	77.85	96.56
93	Landsat 7	ETM+	1	NAH	Brunt_Stancomb Ice Shelf	Use of semi-automatic edge detection	2011	LE07_L1GT_183114_20110228_20161210_01_T2_B8	46426	18.71	77.85	96.56
94	Landsat 7	ETM+	1	NAH	Lyddan Island	Extensive use of semi-automatic edge detection. Use of neighbouring scene to interpolate over data gaps in Landsat scene.	2011	LE07_L1GT_183112_20110228_20161209_01_T2_B8	54065	10.65	77.85	88.50
95	Landsat 7	ETM+	1	NAH	Cape Norvegia	Extensive use of semi-automatic edge detection	2011	LE07_L1GT_180110_20110223_20161211_01_T2_B8	30165	10.65	77.85	88.50

96	Landsat 7	ETM+	1	NAH	Ekstrom Ice Shelf	Extensive use of semi-automatic edge detection	2011	LE07_L1GT_180110_20110223_20161211_01_T2_B8	11155	10.65	77.85	88.50
97	Landsat 7	ETM+	2	NAH	Unneruskollen Island	Some use of semi-automatic edge detection. Snow cover making exact ice front difficult to spot.	2011	LE07_L1GT_177110_20110117_20161210_01_T2_B8	28123	18.71	77.85	96.56
98	Landsat 7	ETM+	1	NAH	Blåskimen Island	Some use of semi-automatic edge detection. Some thin cloud cover, but coastline visible.	2011	LE07_L1GT_176110_20110315_20161209_01_T2_B8	40698	18.71	77.85	96.56
99	Landsat 7	ETM+	2	NAH	Riisner-Larsen Ice Shelf	Interpolation over data gaps using neighbouring scene, which, although cloud-covered, clearly showed the coastline once the contrast was changed	2011	LE07_L1GT_179111_20110216_20161210_01_T2_B8	10017	34.82	77.85	112.67
100	Landsat 7	ETM+	1	NAH	Ekstrom Ice Shelf	Extensive use of semi-automatic edge detection	2011	LE07_L1GT_178110_20110124_20161210_01_T2_B8	2025	10.65	77.85	88.50
101	Landsat 7	ETM+	2	NAH	Atka Ice Shelf	Some use of semi-automatic edge detection. Snow cover making exact ice front difficult to spot.	2011	LE07_L1GT_177110_20110117_20161210_01_T2_B8	3222	18.71	77.85	96.56
102	Landsat 7	ETM+	1	NAH	Fimbul Ice Shelf	Some use of semi-automatic edge detection. Some thin cloud cover, but coastline visible.	2011	LE07_L1GT_176110_20110315_20161209_01_T2_B8	3725	18.71	77.85	96.56
103	Landsat 7	ETM+	1	NAH	Berkner Island	Some thin cloud cover, but coastline still easily identifiable.	2013	LE07_L1GT_192116_20130216_20161126_01_T2_B8	56614	34.82	77.85	112.67
104	Landsat 7	ETM+	1	NAH	Filchner Ice Shelf	Some small areas of interpolation due to data gaps in Landsat 7 scene - but cross-checked against next scene, which includes areas in gaps. Extensive use of semi-automatic edge extraction.	2013	LE07_L1GT_189116_20130126_20161126_01_T2_B8	181973	10.65	77.85	88.50

105	Landsat 7	ETM+	1	NAH	Filchner Ice Shelf	Some small areas of interpolation due to data gaps in Landsat 7 scene - but cross-checked against next scene, which includes areas in gaps. Some use of semi-automatic edge extraction.	2013	LE07_L1GT_185116_20130215_20161126_01_T2_B8	138512	18.71	77.85	96.56
106	Landsat 7	ETM+	2	NAH	Coats Land	Some cloud cover, but not prohibitive to mapping. Some minor areas of interpretation where Landsat 7 scene data gaps. Some use of semi-automatic edge extractuion.	2013	LE07_L1GT_184116_20130123_20161126_01_T2_B8	241266	18.71	77.85	96.56
107	Landsat 7	ETM+	1	NAH	Coats Land	Extensive use of semi-automatic edge extraction.	2013	LE07_L1GT_184115_20130123_20161126_01_T2_B8	72554	10.65	77.85	88.50
108	Landsat 7	ETM+	1	NAH	Coats Land	Some thin cloud cover, but non-prohibitive to mapping. Some use of semi-automatic edge extraction.	2013	LE07_L1GT_184115_20121104_20161127_01_T2_B8	127531	18.71	77.85	96.56
109	Landsat 7	ETM+	1	NAH	Coats Land	Extensive use of semi-automatic edge detection, especially as no sea ice. Some minor interpolation, where data gaps in the Landsat 7 scene; cross-checked with neighbouring scene.	2013	LE07_L1GT_184114_20121222_20190516_01_T2_B8	129332	10.65	77.85	88.50
110	Landsat 7	ETM+	1	NAH	Brunt_Stancomb Ice Shelf	Some use of semi-automatic edge detection. Interpolation were data gaps in Landsat scene; used neighbouring scene to cross-check.	2013	LE07_L1GT_182114_20130226_20161125_01_T2_B8	62316	18.71	77.85	96.56
111	Landsat 7	ETM+	2	NAH	Brunt_Stancomb Ice Shelf	Some thin cloud cover	2013	LE07_L1GT_184114_20121222_20190516_01_T2_B8	100417	34.82	77.85	112.67
112	Landsat 7	ETM+	3	NAH	Brunt_Stancomb Ice Shelf	Data gaps in Landsat scene	2013	LE07_L1GT_182114_20130226_20161125_01_T2_B8	15350	34.82	77.85	112.67

113	Landsat 7	ETM+	2	NAH	Brunt_Stancomb Ice Shelf	Some thin cloud cover. Use of semi-automatic edge detection, especially where no sea ice	2013	LE07_L1GT_184114_20121222_20190516_01_T2_B8	30232	18.71	77.85	96.56
114	Landsat 7	ETM+	1	NAH	Brunt_Stancomb Ice Shelf	Some minor cloud cover. Use of semi-automatic edge detection to speed up digitising.	2013	LE07_L1GT_184113_20121104_20161127_01_T2_B8	98844	18.71	77.85	96.56
115	Landsat 7	ETM+	2	NAH	Brunt_Stancomb Ice Shelf	Ice shelf appears to be made up of various icebergs, therefore difficult to deliniate the exact coastline	2013	LE07_L1GT_183113_20130201_20161127_01_T2_B8	118900	34.82	77.85	112.67
116	Landsat 7	ETM+	1	NAH	Brunt_Stancomb Ice Shelf	Use of semi-automatic edge extraction	2013	LE07_L1GT_184113_20121104_20161127_01_T2_B8	56559	18.71	77.85	96.56
117	Landsat 7	ETM+	1	NAH	Brunt_Stancomb Ice Shelf	Use of semi-automatic edge extraction, especially as minimal sea ice. Some small areas of interpolation where data missing from landsat scene.	2013	LE07_L1GT_185113_20130215_20161126_01_T2_B8	220868	18.71	77.85	96.56
118	Landsat 7	ETM+	2	NAH	Brunt_Stancomb Ice Shelf	Difficult to distinguish sea ice from ice shelf in this part of the glacier. Some use of semi-automatic edge detection	2013	LE07_L1GT_183113_20130217_20161126_01_T2_B8	293030	18.71	77.85	96.56
119	Landsat 7	ETM+	2	NAH	Brunt_Stancomb Ice Shelf	Some thin cloud cover. Straight-line interpolation across Landsat scene data gaps.	2013	LE07_L1GT_185113_20121213_20161128_01_T2_B8	37150	34.82	77.85	112.67
120	Landsat 7	ETM+	2	NAH	Brunt_Stancomb Ice Shelf	Some thin cloud cover. Use of semi-automatic edge detection, but with interpolation between points where data gaps in the Landsat scene. Extents of crevasses/cracks difficult due to snow cover.	2013	LE07_L1GT_184113_20130224_20161126_01_T2_B8	332061	18.71	77.85	96.56

121	Landsat 7	ETM+	1	NAH	Lyddan Island	Extensive iuse of semi-automatic edge detection, which worked especially well in this scene which has minimal sea ice	2013	LE07_L1GT_183113_20130217_20161126_01_T2_B8	34144	10.65	77.85	88.50
122	Landsat 7	ETM+	1	NAH	Riisner-Larsen Ice Shelf	Extensive use of semi-automatic edge detection. Used neighbouring scene to cross-check interpolation across data gaps in Landsat scene.	2013	LE07_L1GT_183112_20130217_20161125_01_T2_B8	251084	10.65	77.85	88.50
123	Landsat 7	ETM+	1	NAH	Riisner-Larsen Ice Shelf	Some small areas of thin cloud cover, but not prohibitive to mapping. Some use of semi-automatic edge extraction, especially where no sea ice. Neighbouring scene used to cross-reference areas where data missing from Landsat scene.	2013	LE07_L1GT_183111_20130217_20161126_01_T2_B8	581244	18.71	77.85	96.56
124	Landsat 7	ETM+	1	NAH	Riisner-Larsen Ice Shelf	Some use of semi-autonomous edge detection. Linear interpolation between points across data gaps in Landsat scene; crioss-referenced with nieghbouring scene	2013	LE07_L1GT_180111_20130228_20161125_01_T2_B8	216571	18.71	77.85	96.56
125	Landsat 7	ETM+	1	NAH	Ekstrom Ice Shelf	Extensive use of semi-automatic edge detection. Linear interpolation between points over data gaps in the Landsat scene; cross checked against neighbouring scene from same year.	2013	LE07_L1GT_180110_20130228_20161125_01_T2_B8	252678	10.65	77.85	88.50

126	Landsat 7	ETM+	1	NAH	Atka Ice Shelf	Extensive use of semi-automatic edge detection. Linear interpolation between points over data gaps in the Landsat scene; cross checked against neighbouring scene from same year.	2013	LE07_L1GT_178110_20130302_20161126_01_T2_B8	61822	10.65	77.85	88.50
127	Landsat 7	ETM+	2	NAH	Jelbart Ice Shelf	Interpolated between points over gaps in the Landsat scene. Neighbouring scene and from different times were cloud covered. Some use of semi-automatic edge detection.	2013	LE07_L1GT_176110_20121230_20190516_01_T2_B8	420734	18.71	77.85	96.56
128	Landsat 7	ETM+	1	NAH	Fimbul Ice Shelf		2013	LE07_L1GT_170109_20121204_20161127_01_T2_B8	203720	34.82	77.85	112.67
129	Landsat 7	ETM+	1	NAH	Fimbul Ice Shelf	Some use of semi-automatic edge detection. Interpolation between points over data gaps in Landsat scene	2013	LE07_L1GT_174110_20130218_20161126_01_T2_B8	117201	18.71	77.85	96.56
130	Landsat 7	ETM+	2	NAH	Fimbul Ice Shelf	Some use of semi-automatic edge detection. Sea ice causing some minor areas of uncertainty. Interpolation between points over data gaps in Landsat scene, using neighbouring scenes to cross-check.	2013	LE07_L1GT_172109_20130220_20161125_01_T2_B8	267293	18.71	77.85	96.56
131	Landsat 7	ETM+	2	NAH	Fimbul Ice Shelf	Some use of semi-automatic edge detection, especially in areas free of sea ice. Some areas of uncertainty around cracks/crevases due to snow cover. Interpolation between points over data gaps in the Landsat scene cross checked to nieghbouring scenes	2013	LE07_L1GT_174109_20130218_20161125_01_T2_B8	664086	18.71	77.85	96.56

132	Landsat 7	ETM+	2	NAH	Coats Land		2013	LE07_L1GT_185115_20121213_20161126_01_T2_B8	18079	34.82	77.85	112.67
133	Landsat 7	ETM+	1	NAH		Extensive use of semi-automatic edge detection. Linear interpolation between points over data gaps in the Landsat scene; cross checked against neighbouring scene from same year.	2013	LE07_L1GT_180110_20130228_20161125_01_T2_B8	21158	10.65	77.85	88.50
134	Landsat 7	ETM+	2	NAH	Filchner Ice Shelf	Some cloud cover, but not prohibitive to mapping. Some minor areas of interpretation where Landsat 7 scene data gaps. Some use of semi-automatic edge extractuion.	2013	LE07_L1GT_184116_20130123_20161126_01_T2_B8	35113	18.71	77.85	96.56
135	Landsat 7	ETM+	1	NAH	Brunt_Stancomb Ice Shelf	Extensive use of semi-automatic edge detection, especially as no sea ice. Some minor interpolation, where data gaps in the Landsat 7 scene; cross-checked with neighbouring scene.	2013	LE07_L1GT_184114_20121222_20190516_01_T2_B8	39007	10.65	77.85	88.50
136	Landsat 7	ETM+	1	NAH	Lyddan Island	Extensive use of semi-automatic edge detection. Used neighbouring scene to cross-check interpolation across data gaps in Landsat scene.	2013	LE07_L1GT_183112_20130217_20161125_01_T2_B8	53673	10.65	77.85	88.50
137	Landsat 7	ETM+	1	NAH	Cape Norvegia	Some use of semi-autonomous edge detection. Linear interpolation between points across data gaps in Landsat scene; crioss-referenced with nieghbouring scene	2013	LE07_L1GT_180111_20130228_20161125_01_T2_B8	40792	18.71	77.85	96.56

138	Landsat 7	ETM+	1	NAH	Quar Ice Shelf	Extensive use of semi-automatic edge detection. Linear interpolation between points over data gaps in the Landsat scene; cross checked against neighbouring scene from same year.	2013	LE07_L1GT_180110_20130228_20161125_01_T2_B8	104342	10.65	77.85	88.50
139	Landsat 7	ETM+	1	NAH	Atka Ice Shelf	Extensive use of semi-automatic edge detection. Linear interpolation between points over data gaps in the Landsat scene; cross checked against neighbouring scene from same year.	2013	LE07_L1GT_180110_20130228_20161125_01_T2_B8	50668	10.65	77.85	88.50
140	Landsat 7	ETM+	1	NAH	Unneruskollen Island	Extensive use of semi-automatic edge detection. Linear interpolation between points over data gaps in the Landsat scene; cross checked against neighbouring scene from same year.	2013	LE07_L1GT_178110_20130302_20161126_01_T2_B8	27923	10.65	77.85	88.50
141	Landsat 7	ETM+	1	NAH	Jelbart Ice Shelf	Extensive use of semi-automatic edge detection. Linear interpolation between points over data gaps in the Landsat scene; cross checked against neighbouring scene from same year.	2013	LE07_L1GT_178110_20130302_20161126_01_T2_B8	33769	10.65	77.85	88.50
142	Landsat 7	ETM+	2	NAH	Blåskimen Island	Interpolated between points over gaps in the Landsat scene. Neighbouring scene and from different times were cloud covered. Some use of semi-automatic edge detection.	2013	LE07_L1GT_176110_20121230_20190516_01_T2_B8	39077	18.71	77.85	96.56

143	Landsat 7	ETM+	1	NAH	Berkner Island	Some small areas of interpolation due to data gaps in Landsat 7 scene - but cross-checked against next scene, which includes areas in gaps. Extensive use of semi-automatic edge extraction.	2013	LE07_L1GT_189116_20130126_20161126_01_T2_B8	51546	10.65	77.85	88.50
144	Landsat 7	ETM+	1	NAH	Cape Norvegia	Extensive use of semi-automatic edge detection. Linear interpolation between points over data gaps in the Landsat scene; cross checked against neighbouring scene from same year.	2013	LE07_L1GT_180110_20130228_20161125_01_T2_B8	29883	10.65	77.85	88.50
145	Landsat 7	ETM+	2	NAH	Fimbul Ice Shelf	Interpolated between points over gaps in the Landsat scene. Neighbouring scene and from different times were cloud covered. Some use of semi-automatic edge detection.	2013	LE07_L1GT_176110_20121230_20190516_01_T2_B8	3427	18.71	77.85	96.56
146	Sentinel-1a		2	NAH	Berkner Island	Difficult to locate exact loaction of creavsses at boundary between island and ice shelf	2015	S1A_EW_GRDM_1SSH_20150204T023024_20150204T023124_004467_0057A0_4944_Orb_NR_Cal_dB_TC	103889	102.71	1,364.46	1,467.17
147	Sentinel-1a		2	NAH	Filchner Ice Shelf		2015	S1A_EW_GRDM_1SSH_20150126T025443_20150126T025544_004336_00549F_72F6_Orb_NR_Cal_dB_TC	8469	102.71	1,364.46	1,467.17
148	Sentinel-1a		2	NAH	Filchner Ice Shelf		2015	S1A_EW_GRDM_1SSH_20150126T025339_20150126T025443_004336_00549F_10D7_Orb_NR_Cal_dB_TC	128607	102.71	1,364.46	1,467.17
149	Landsat 8	OLI	2	NAH	Filchner Ice Shelf	Thin layer of cloud covering scene	2015	LC08_L1GT_184116_20150206_20180527_01_T2_B8	41379	34.82	43.88	78.70

150	Sentinel-1a		2	NAH	Filchner Ice Shelf	Used sentinel-1 here to map the extent of the crevasse.	2015	S1A_EW_GRDM_1SSH_20150126T025339_20150126T025443_004336_00549F_10D7_Orb_NR_Cal_dB_TC	15030	102.71	1,364.46	1,467.17
151	Landsat 8	OLI	2	NAH	Filchner Ice Shelf	Thin layer of cloud covering scene. Some shadows on south-facing slopes.	2015	LC08_L1GT_184116_20150206_20180527_01_T2_B8	122761	34.82	43.88	78.70
152	Landsat 8	OLI	2	NAH	Coats Land	Thin layer of cloud covering scene. Cross-checking with Sentinel-1 EW scenes in places.	2015	LC08_L1GT_184116_20150206_20180527_01_T2_B8	90994	34.82	43.88	78.70
153	Landsat 8	OLI	1	NAH	Coats Land	Some use of semi-automatic edge detection to speed up digitising. Thin layer of cloud over scene, but coastline visible.	2015	LC08_L1GT_184116_20150206_20180527_01_T2_B8	53014	18.71	43.88	62.58
154	Landsat 8	OLI	1	NAH	Coats Land	Thin layer of cloud covering some areas, but coastline still visible. Some use of semi-automatic edge extraction, especially whwere no sea ice.	2015	LC08_L1GT_184115_20150206_20180527_01_T2_B8	218617	18.71	43.88	62.58
155	Landsat 8	OLI	1	NAH	Brunt_Stancomb Ice Shelf	Extensive use of semi-automatic edge detection due to lack of sea ice and cloud in this scene. Use of Sentinel-1 EW scenes to cross reference, especially for cracks and crevasses.	2015	LC08_L1GT_184114_20150206_20180527_01_T2_B8	294891	10.65	43.88	54.53
156	Landsat 8	OLI	1	NAH	Brunt_Stancomb Ice Shelf		2015	LC08_L1GT_184113_20150206_20180527_01_T2_B8	26566	34.82	43.88	78.70
157	Landsat 8	OLI	2	NAH	Brunt_Stancomb Ice Shelf	Difficult to pick out the exact extent of the cracks and crevasses due to snow cover. Some minor use of Sentinel-1 EW scenes to cross-check.	2015	LC08_L1GT_184113_20150206_20180527_01_T2_B8	75914	34.82	43.88	78.70
158	Landsat 8	OLI	1	NAH	Brunt_Stancomb Ice Shelf		2015	LC08_L1GT_184113_20150326_20180527_01_T2_B8	80522	34.82	43.88	78.70

159	Sentinel-1a		2	NAH	Brunt_Stancomb Ice Shelf	To cover area of cloud in Landsat imagery	2015	S1A_EW_GRDM_1SSH_20150129T230647_20150129T230751_004392_0055D2_A3FB_Orb_NR_Cal_dB_TC	8432	102.71	1,364.46	1,467.17
160	Sentinel-1a		3	NAH	Brunt_Stancomb Ice Shelf	Difficult to pick out exact coastline due to sea ice and noisy imagery. Used because of cloud cover in Landsat scene.	2015	S1A_EW_GRDM_1SSH_20150129T230647_20150129T230751_004392_0055D2_A3FB_Orb_NR_Cal_dB_TC	224780	102.71	1,364.46	1,467.17
161	Landsat 8	OLI	1	NAH	Brunt_Stancomb Ice Shelf	Some use of semi-automatic edge detection.	2015	LC08_L1GT_184113_20150206_20180527_01_T2_B8	89411	18.71	43.88	62.58
162	Sentinel-1a		2	NAH	Brunt_Stancomb Ice Shelf	Diffcult to puick out exact ice sfront locations, especially in areas with many crevasses and cracks. Some use of semi-automatic edge detection, where coastline was clear.	2015	S1A_EW_GRDM_1SSH_20150129T230647_20150129T230751_004392_0055D2_A3FB_Orb_NR_Cal_dB_TC	596109	52.40	1,364.46	1,416.86
163	Sentinel-1a		2	NAH	Riisner-Larsen Ice Shelf	Some areas difficult to pick out the coastline due to sea ice. Ssome use of semi-automatic edge detection in areas wherre no sea ice.	2015	S1A_EW_GRDM_1SSH_20150130T220957_20150130T221101_004406_005627_2CFD_Orb_NR_Cal_dB_TC	848069	52.40	1,364.46	1,416.86
164	Sentinel-1a		2	NAH	Ekstrom Ice Shelf	Some use of semi-automatic edge detection. A few areas of uncertainty where sea ice	2015	S1A_EW_GRDM_1SSH_20150205T212112_20150205T212213_004493_005832_6718_Orb_NR_Cal_dB_TC	257091	52.40	1,364.46	1,416.86
165	Landsat 8	OLI	1	NAH	Unneruskollen Island	Some use of semi-automatic edge detection	2015	LC08_L1GT_177110_20150205_20170413_01_T2_B8	24865	18.71	43.88	62.58

166	Landsat 8	OLI	1	NAH	Jelbart Ice Shelf	Use of semi-automatic edge detection. Supplimented with Sentinel-1 EW dat, especially to deliniate the extents of cracks/crevasses which cannot be seen from the optical imagery (S1A_EW_GRDM_1SSH_20150204T204009_20150204T204113_004478_0057E4_CED9)	2015	LC08_L1GT_177110_20150205_20170413_01_T2_B8	437449	18.71	43.88	62.58
167	Sentinel-1a		3	NAH	Jelbart Ice Shelf	Difficult to pick out coastline in Landsat scene due to snow cover. Still slightly unclear in Sentinel-1 imagery.	2015	S1A_EW_GRDM_1SSH_20150204T204009_20150204T204113_004478_0057E4_CED9_Orb_NR_Cal_dB_TC	19990	102.71	1,364.46	1,467.17
168	Landsat 8	OLI	2	NAH	Fimbul Ice Shelf	Some areas of snow cover/cloud cover where it is difficult to pick out coastline and crevasses. Some use of semi-automatic edge detection in areas without sea ice or cloud cover.	2015	LC08_L1GT_171109_20150126_20170413_01_T2_B8	291905	18.71	43.88	62.58
169	Sentinel-1a		2	NAH	Fimbul Ice Shelf		2015	S1A_EW_GRDM_1SSH_20150130T203155_20150130T203259_004405_00561F_33F9_Orb_NR_Cal_dB_TC	13319	102.71	1,364.46	1,467.17
170	Landsat 8	OLI	1	NAH	Fimbul Ice Shelf	Extensive use of semi-automatic edge detection.	2015	LC08_L1GT_175110_20150207_20170413_01_T2_B8	62327	10.65	43.88	54.53
171	Sentinel-1a		3	NAH	Fimbul Ice Shelf	Very difficult to pick out exact features, especially due to sea ice	2015	S1A_EW_GRDM_1SSH_20150130T203155_20150130T203259_004405_00561F_33F9_Orb_NR_Cal_dB_TC	74502	102.71	1,364.46	1,467.17
172	Landsat 8	OLI	1	NAH	Fimbul Ice Shelf	Some use of semi-automatic edge detection	2015	LC08_L1GT_172110_20150202_20170413_01_T2_B8	37371	18.71	43.88	62.58
173	Sentinel-1a		2	NAH	Fimbul Ice Shelf	Extensive use of semi-automatic edge detection	2015	S1A_EW_GRDM_1SSH_20150204T204009_20150204T204113_004478_0057E4_CED9_Orb_NR_Cal_dB_TC	48706	27.25	1,364.46	1,391.71

174	Sentinel-1a		2	NAH	Fimbul Ice Shelf	A few areas of uncertainty, particularly around large cracks/crevasses, Some use of semi-automatic edge detection where no sea ice in the scene.	2015	S1A_EW_GRDM_1SSH_20150204T204009_20150204T204113_004478_0057E4_CED9_Orb_NR_Cal_dB_TC	587456	52.40	1,364.46	1,416.86
175	Landsat 8	OLI	1	NAH	Fimbul Ice Shelf	Some use of semi-automatic edge extraction	2015	LC08_L1GT_171109_20150126_20170413_01_T2_B8	26779	18.71	43.88	62.58
176	Landsat 8	OLI	1	NAH	Fimbul Ice Shelf	Partial use of semi-automatic edge detection	2015	LC08_L1GT_171109_20150126_20170413_01_T2_B8	12980	18.71	43.88	62.58
177	Sentinel-1a		2	NAH	Fimbul Ice Shelf		2015	S1A_EW_GRDM_1SSH_20150204T204009_20150204T204113_004478_0057E4_CED9_Orb_NR_Cal_dB_TC	14511	102.71	1,364.46	1,467.17
178	Landsat 8	OLI	1	NAH	Fimbul Ice Shelf	Some thin cloud, but coastline still visible	2015	LC08_L1GT_172110_20150202_20170413_01_T2_B8	65131	34.82	43.88	78.70
179	Landsat 8	OLI	1	NAH	Fimbul Ice Shelf	Use of semi-automatic edge extraction	2015	LC08_L1GT_171109_20150126_20170413_01_T2_B8	15427	18.71	43.88	62.58
180	Sentinel-1a		2	NAH	Fimbul Ice Shelf		2015	S1A_EW_GRDM_1SSH_20150204T204009_20150204T204113_004478_0057E4_CED9_Orb_NR_Cal_dB_TC	4875	102.71	1,364.46	1,467.17
181	Sentinel-1a		2	NAH	Filchner Ice Shelf	Difficult to locate exact loaction of creavsses at boundary between island and ice shelf	2015	S1A_EW_GRDM_1SSH_20150204T023024_20150204T023124_004467_0057A0_4944_Orb_NR_Cal_dB_TC	65747	102.71	1,364.46	1,467.17
182	Landsat 8	OLI	2	NAH	Coats Land	Thin layer of cloud covering scene. Some shadows on south-facing slopes.	2015	LC08_L1GT_184116_20150206_20180527_01_T2_B8	95959	34.82	43.88	78.70
183	Landsat 8	OLI	1	NAH	Coats Land	Extensive use of semi-automatic edge detection due to lack of sea ice and cloud in this scene. Use of Sentinel-1 EW scenes to cross reference, especially for cracks and crevasses.	2015	LC08_L1GT_184114_20150206_20180527_01_T2_B8	128935	10.65	43.88	54.53

184	Sentinel-1a		2	NAH	Riisner-Larsen Ice Shelf	Diffcult to puick out exact ice sfront locations, especially in areas with many crevasses and cracks. Some use of semi-automatic edge detection, where coastline was clear.	2015	S1A_EW_GRDM_1SSH_20150129T230647_20150129T230751_004392_0055D2_A3FB_Orb_NR_Cal_dB_TC	31226	52.40	1,364.46	1,416.86
185	Sentinel-1a		2	NAH	Lyddan Island	Diffcult to puick out exact ice sfront locations, especially in areas with many crevasses and cracks. Some use of semi-automatic edge detection, where coastline was clear.	2015	S1A_EW_GRDM_1SSH_20150129T230647_20150129T230751_004392_0055D2_A3FB_Orb_NR_Cal_dB_TC	88450	52.40	1,364.46	1,416.86
186	Sentinel-1a		2	NAH	Riisner-Larsen Ice Shelf	Some use of semi-automatic edge detection. A few areas of uncertainty where sea ice	2015	S1A_EW_GRDM_1SSH_20150205T212112_20150205T212213_004493_005832_6718_Orb_NR_Cal_dB_TC	184905	52.40	1,364.46	1,416.86
187	Sentinel-1a		2	NAH	Cape Norvegia	Some use of semi-automatic edge detection. A few areas of uncertainty where sea ice	2015	S1A_EW_GRDM_1SSH_20150205T212112_20150205T212213_004493_005832_6718_Orb_NR_Cal_dB_TC	69685	52.40	1,364.46	1,416.86
188	Sentinel-1a		2	NAH	Quar Ice Shelf	Some use of semi-automatic edge detection. A few areas of uncertainty where sea ice	2015	S1A_EW_GRDM_1SSH_20150205T212112_20150205T212213_004493_005832_6718_Orb_NR_Cal_dB_TC	109475	52.40	1,364.46	1,416.86
189	Sentinel-1a		2	NAH		Some use of semi-automatic edge detection. A few areas of uncertainty where sea ice	2015	S1A_EW_GRDM_1SSH_20150205T212112_20150205T212213_004493_005832_6718_Orb_NR_Cal_dB_TC	21221	52.40	1,364.46	1,416.86
190	Sentinel-1a		2	NAH	Atka Ice Shelf	Some use of semi-automatic edge detection. A few areas of uncertainty where sea ice	2015	S1A_EW_GRDM_1SSH_20150205T212112_20150205T212213_004493_005832_6718_Orb_NR_Cal_dB_TC	109126	52.40	1,364.46	1,416.86
191	Landsat 8	OLI	1	NAH	Atka Ice Shelf	Some use of semi-automatic edge detection	2015	LC08_L1GT_177110_20150205_20170413_01_T2_B8	3886	18.71	43.88	62.58

192	Sentinel-1a		3	NAH	Unneruskollen Island	Difficult to pick out coastline in Landsat scene due to snow cover. Still slightly unclear in Sentinel-1 imagery.	2015	S1A_EW_GRDM_1SSH_20150204T204009_20150204T204113_004478_0057E4_CED9_Orb_NR_Cal_dB_TC	2599	102.71	1,364.46	1,467.17
193	Landsat 8	OLI	1	NAH	Blåskimen Island	Use of semi-automatic edge detection. Supplimented with Sentinel-1 EW dat, especially to deliniate the extents of cracks/crevasses which cannot be seen from the optical imagery (S1A_EW_GRDM_1SSH_20150204T204009_20150204T204113_004478_0057E4_CED9)	2015	LC08_L1GT_177110_20150205_20170413_01_T2_B8	14349	18.71	43.88	62.58
194	Landsat 8	OLI	1	NAH	Blåskimen Island	Extensive use of semi-automatic edge detection.	2015	LC08_L1GT_175110_20150207_20170413_01_T2_B8	24277	10.65	43.88	54.53
195	Landsat 8	OLI	2	NAH	Brunt_Stancomb Ice Shelf	Difficult to pick out the exact extent of the cracks and crevasses due to snow cover. Some minor use of Sentinel-1 EW scenes to cross-check.	2015	LC08_L1GT_184113_20150206_20180527_01_T2_B8	16248	34.82	43.88	78.70
196	Landsat 8	OLI	2	NAH	Brunt_Stancomb Ice Shelf	Difficult to pick out the exact extent of the cracks and crevasses due to snow cover. Some minor use of Sentinel-1 EW scenes to cross-check.	2015	LC08_L1GT_184113_20150206_20180527_01_T2_B8	16791	34.82	43.88	78.70
197	Landsat 8	OLI	2	NAH	Brunt_Stancomb Ice Shelf	Difficult to pick out the exact extent of the cracks and crevasses due to snow cover. Some minor use of Sentinel-1 EW scenes to cross-check.	2015	LC08_L1GT_184113_20150206_20180527_01_T2_B8	10939	34.82	43.88	78.70
198	Landsat 8	OLI	1	NAH	Filchner Ice Shelf	Some use of semi-automatic edge detection to speed up digitising.	2017	LC08_L1GT_192116_20170219_20180527_01_T2_B8	106549	18.71	43.88	62.58
199	Landsat 8	OLI	1	NAH	Filchner Ice Shelf	Some use of semi-automatic edge detection to speed up digitising.	2017	LC08_L1GT_190116_20170205_20170216_01_T2_B8	182415	18.71	43.88	62.58

200	Landsat 8	OLI	1	NAH	Coats Land	Some use of semi-automatic edge detection to speed up digitising. Exact loactions difficult to identify in crevassed areas where ice shelves meet grounded ice.	2017	LC08_L1GT_183116_20170220_20170301_01_T2_B8	200695	18.71	43.88	62.58
201	Sentinel-1b		2	NAH	Coats Land	Sea ice making manual delineation tricky in some ares	2017	S1B_IW_GRDH_1SSH_20170213T035006_20170213T035033_004276_0076B2_9679_Orb_NR_Cal_dB_TC	256079	62.90	760.16	823.06
202	Sentinel-1b		1	NAH	Coats Land		2017	S1B_IW_GRDH_1SSH_20170108T034942_20170108T035007_003751_00672A_3D54_Orb_NR_Cal_dB_TC	17104	62.90	760.16	823.06
203	Sentinel-1a		1	NAH	Brunt_Stancomb Ice Shelf	A few creavassed areas, particularly around glacier tounges, making exact digitising difficult. Use of semi-automatic edge-detection techniques in some areas where coastline easy to deliminate.	2017	S1A_IW_GRDH_1SSH_20170114T035020_20170114T035048_014822_01826E_FE5A_Orb_NR_Cal_dB_TC	528121	34.10	760.16	794.26
204	Sentinel-1a		1	NAH	Brunt_Stancomb Ice Shelf		2017	S1A_IW_GRDH_1SSH_20170126T034951_20170126T035020_014997_0187E1_1BDA_Orb_NR_Cal_dB_TC	61077	62.90	760.16	823.06
205	Sentinel-1a		2	NAH	Brunt_Stancomb Ice Shelf	Some areas difficult to pick out exact edges of cracks/crevasses.	2017	S1A_IW_GRDH_1SSH_20170126T034951_20170126T035020_014997_0187E1_1BDA_Orb_NR_Cal_dB_TC	111392	62.90	760.16	823.06
206	Sentinel-1a		1	NAH	Brunt_Stancomb Ice Shelf	Use of semi-autonomous edge detection for digitising in areas with no sea ice.	2017	S1A_IW_GRDH_1SSH_20170114T035020_20170114T035048_014822_01826E_FE5A_Orb_NR_Cal_dB_TC	70296	34.10	760.16	794.26
207	Landsat 8	OLI	2	NAH	Brunt_Stancomb Ice Shelf	Some use of semi-automatic edge detection. Some light cloud cover over small areas.	2017	LC08_L1GT_184113_20170110_20170311_01_T2_B8	109482	18.71	43.88	62.58

208	Sentinel-1a		1	NAH	Brunt_Stancomb Ice Shelf	Sea ice making coastline deliniation in some small areas difficult.	2017	S1A_IW_GRDH_1SSH_20170126T034951_20170126T035020_014997_0187E1_1BDA_Orb_NR_Cal_dB_TC	52792	62.90	760.16	823.06
209	Sentinel-1b		1	NAH	Riiser-Larsen Ice Shelf	Extensive use of semi-automatic edge detection along this section, due to easily identifiable coatline.	2017	S1B_IW_GRDH_1SSH_20170108T034852_20170108T034917_003751_00672A_6EAB_Orb_NR_Cal_dB_TC	108932	19.70	760.16	779.86
210	Sentinel-1b		1	NAH	Riiser-Larsen Ice Shelf		2017	S1B_IW_GRDH_1SSH_20170108T034852_20170108T034917_003751_00672A_6EAB_Orb_NR_Cal_dB_TC	88761	62.90	760.16	823.06
211	Landsat 8	OLI	1	NAH	Riiser-Larsen Ice Shelf	Extensive use of semi-automatic edge detection as there was no sea ice or cloud cover in the scene.	2017	LC08_L1GT_182112_20170317_20170328_01_T2_B8	47856	10.65	43.88	54.53
212	Landsat 8	OLI	1	NAH	Riiser-Larsen Ice Shelf	Extensive use of semi-automatic edge detection as there was no sea ice or cloud cover in the scene	2017	LC08_L1GT_182112_20170317_20170328_01_T2_B8	86072	10.65	43.88	54.53
213	Sentinel-1b		1	NAH	Riiser-Larsen Ice Shelf		2017	S1B_IW_GRDH_1SSH_20170108T034852_20170108T034917_003751_00672A_6EAB_Orb_NR_Cal_dB_TC	58607	62.90	760.16	823.06
214	Sentinel-1b		1	NAH	Riiser-Larsen Ice Shelf		2017	S1B_IW_GRDH_1SSH_20170108T034852_20170108T034917_003751_00672A_6EAB_Orb_NR_Cal_dB_TC	33164	62.90	760.16	823.06
215	Sentinel-1b		1	NAH	Riiser-Larsen Ice Shelf		2017	S1B_IW_GRDH_1SSH_20170108T034852_20170108T034917_003751_00672A_6EAB_Orb_NR_Cal_dB_TC	31929	62.90	760.16	823.06
216	Sentinel-1b		1	NAH	Riiser-Larsen Ice Shelf		2017	S1B_IW_GRDH_1SSH_20170225T034826_20170225T034851_004451_007BF3_7C17_Orb_NR_Cal_dB_TC	3774	62.90	760.16	823.06

217	Sentinel-1b		1	NAH	Quar Ice Shelf	Some use of semi-automatic edge detection along non-crevassed coastline.	2017	S1B_IW_GRDH_1SSH_20170225T034801_20170225T034826_004451_007BF3_3F14_Orb_NR_Cal_dB_TC	111525	34.10	760.16	794.26
218	Sentinel-1b		1	NAH	Ekstrom Ice Shelf	Some use of semi-automatic edge detection	2017	S1B_IW_GRDH_1SSH_20170225T034736_20170225T034801_004451_007BF3_D342_Orb_NR_Cal_dB_TC	73520	34.10	760.16	794.26
219	Sentinel-1b		1	NAH	Ekstrom Ice Shelf	Automatic edge detection, manually checked	2017	S1B_IW_GRDH_1SSH_20170225T034801_20170225T034826_004451_007BF3_3F14_Orb_NR_Cal_dB_TC	6036	62.90	760.16	823.06
220	Sentinel-1b		1	NAH	Atka Ice Shelf	Some use of semi-automatic edge detection in sea-ice free areas.	2017	S1B_IW_GRDH_1SSH_20170225T034736_20170225T034801_004451_007BF3_D342_Orb_NR_Cal_dB_TC	119744	34.10	760.16	794.26
221	Sentinel-1b		1	NAH	Jelbart Ice Shelf		2017	S1B_IW_GRDH_1SSH_20170225T034707_20170225T034736_004451_007BF3_69F7_Orb_NR_Cal_dB_TC	10354	62.90	760.16	823.06
222	Sentinel-1b		1	NAH	Jelbart Ice Shelf		2017	S1B_IW_GRDH_1SSH_20170225T034736_20170225T034801_004451_007BF3_D342_Orb_NR_Cal_dB_TC	13687	62.90	760.16	823.06
223	Sentinel-1b		1	NAH	Jelbart Ice Shelf		2017	S1B_IW_GRDH_1SSH_20170225T034736_20170225T034801_004451_007BF3_D342_Orb_NR_Cal_dB_TC	39612	62.90	760.16	823.06
224	Sentinel-1b		1	NAH	Jelbart Ice Shelf		2017	S1B_IW_GRDH_1SSH_20170225T034736_20170225T034801_004451_007BF3_D342_Orb_NR_Cal_dB_TC	4659	62.90	760.16	823.06
225	Sentinel-1b		1	NAH	Jelbart Ice Shelf		2017	S1B_IW_GRDH_1SSH_20170225T034736_20170225T034801_004451_007BF3_D342_Orb_NR_Cal_dB_TC	2505	62.90	760.16	823.06

226	Sentinel-1b		1	NAH	Jelbart Ice Shelf		2017	S1B_IW_GRDH_1SSH_20170225T034707_20170225T034736_004451_007BF3_69F7_Orb_NR_Cal_dB_TC	13666	62.90	760.16	823.06
227	Sentinel-1b		1	NAH	Jelbart Ice Shelf		2017	S1B_IW_GRDH_1SSH_20170225T034707_20170225T034736_004451_007BF3_69F7_Orb_NR_Cal_dB_TC	5700	62.90	760.16	823.06
228	Sentinel-1b		1	NAH	Jelbart Ice Shelf		2017	S1B_IW_GRDH_1SSH_20170225T034707_20170225T034736_004451_007BF3_69F7_Orb_NR_Cal_dB_TC	5466	62.90	760.16	823.06
229	Sentinel-1b		1	NAH	Jelbart Ice Shelf		2017	S1B_IW_GRDH_1SSH_20170225T034736_20170225T034801_004451_007BF3_D342_Orb_NR_Cal_dB_TC	60452	62.90	760.16	823.06
230	Sentinel-1b		1	NAH	Fimbul Ice Shelf	Some areas with sea ice.	2017	S1B_IW_GRDH_1SSH_20170225T034707_20170225T034736_004451_007BF3_69F7_Orb_NR_Cal_dB_TC	396135	62.90	760.16	823.06
231	Sentinel-1b		1	NAH	Jelbart Ice Shelf		2017	S1B_IW_GRDH_1SSH_20170225T034707_20170225T034736_004451_007BF3_69F7_Orb_NR_Cal_dB_TC	20841	62.90	760.16	823.06
232	Landsat 8	OLI	1	NAH	Fimbul Ice Shelf	A few whispy clouds, but not enough coverage to mask the coastline. A few areas of sea ice making coastline deliniation difficult, but maily over only a few pixels. Some use of semi-automatic edge detection.	2017	LC08_L1GT_171110_20170115_20170311_01_T2_B8	181567	18.71	43.88	62.58
233	Landsat 8	OLI	1	NAH	Fimbul Ice Shelf	Extensive use of semi-automatic edge detection.	2017	LC08_L1GT_170110_20170124_20170311_01_T2_B8	84727	10.65	43.88	54.53
234	Landsat 8	OLI	1	NAH	Fimbul Ice Shelf	Extensive use of semi-automatic edge detection. No sea ice, so high precision.	2017	LC08_L1GT_168110_20170126_20170310_01_T2_B8	127666	10.65	43.88	54.53

235	Landsat 8	OLI	1	NAH	Fimbul Ice Shelf	Some use of semi-automatic edge detection. Sea ice in some areas making coastline deliniation difficult.	2017	LC08_L1GT_174109_20170325_20170329_01_T2_B8	414368	18.71	43.88	62.58
236	Landsat 8	OLI	2	NAH	Fimbul Ice Shelf	Partial cloud cover	2017	LC08_L1GT_170109_20170209_20170217_01_T2_B8	56157	34.82	43.88	78.70
237	Sentinel-1b		2	NAH	Riiser-Larsen Ice Shelf	Sea ice making coastline deliniation difficult in places. Som euse of semi-automatic edge detection, but mainly manual	2017	S1B_IW_GRDH_1SSH_20170225T034826_20170225T034851_004451_007BF3_7C17_Orb_NR_Cal_dB_TC	496989	34.10	760.16	794.26
238	Landsat 8	OLI	1	NAH	Filchner Ice Shelf	Some use of semi-automatic edge detection to speed up digitising. Exact loactions difficult to identify in crevassed areas where ice shelves meet grounded ice.	2017	LC08_L1GT_183116_20170220_20170301_01_T2_B8	166961	18.71	43.88	62.58
239	Landsat 8	OLI	1	NAH	Berkner Island	Some use of semi-automatic edge detection to speed up digitising.	2017	LC08_L1GT_192116_20170219_20180527_01_T2_B8	99669	18.71	43.88	62.58
240	Sentinel-1a		1	NAH	Coats Land	A few creavassed areas, particularly around glacier tounges, making exact digitising difficult. Use of semi-automatic edge-detection techniques in some areas where coastline easy to deliminate.	2017	S1A_IW_GRDH_1SSH_20170114T035020_20170114T035048_014822_01826E_FE5A_Orb_NR_Cal_dB_TC	137597	34.10	760.16	794.26
241	Sentinel-1a		1	NAH	Brunt_Stancomb Ice Shelf	Very difficult to pick out the exact coastline on te margins of the ice tounge.	2017	S1A_IW_GRDH_1SSH_20170126T034951_20170126T035020_014997_0187E1_1BDA_Orb_NR_Cal_dB_TC	604140	62.90	760.16	823.06
242	Sentinel-1a		1	NAH	Lyddan Island	Extensive use of semi-automatic edge detection along the coast of the island.	2017	S1A_IW_GRDH_1SSH_20170126T034951_20170126T035020_014997_0187E1_1BDA_Orb_NR_Cal_dB_TC	89423	19.70	760.16	779.86

243	Sentinel-1a		1	NAH	Riiser-Larsen Ice Shelf	Extensive use of semi-automatic edge detection along the coast of the island.	2017	S1A_IW_GRDH_1SSH_20170126T034951_20170126T035020_014997_0187E1_1BDA_Orb_NR_Cal_dB_TC	9698	19.70	760.16	779.86
244	Sentinel-1b		1	NAH	Riiser-Larsen Ice Shelf	Some use of semi-automatic edge detection along non-crevassed coastline.	2017	S1B_IW_GRDH_1SSH_20170225T034801_20170225T034826_004451_007BF3_3F14_Orb_NR_Cal_dB_TC	126876	34.10	760.16	794.26
245	Sentinel-1b		1	NAH		Some use of semi-automatic edge detection along non-crevassed coastline.	2017	S1B_IW_GRDH_1SSH_20170225T034801_20170225T034826_004451_007BF3_3F14_Orb_NR_Cal_dB_TC	21403	34.10	760.16	794.26
246	Sentinel-1b		1	NAH	Cape Norvegia	Some use of semi-automatic edge detection along non-crevassed coastline.	2017	S1B_IW_GRDH_1SSH_20170225T034801_20170225T034826_004451_007BF3_3F14_Orb_NR_Cal_dB_TC	72110	34.10	760.16	794.26
247	Sentinel-1b		1	NAH	Ekstrom Ice Shelf	Some use of semi-automatic edge detection along non-crevassed coastline.	2017	S1B_IW_GRDH_1SSH_20170225T034801_20170225T034826_004451_007BF3_3F14_Orb_NR_Cal_dB_TC	9976	34.10	760.16	794.26
248	Sentinel-1b		1	NAH	Ekstrom Ice Shelf	Some use of semi-automatic edge detection in sea-ice free areas.	2017	S1B_IW_GRDH_1SSH_20170225T034736_20170225T034801_004451_007BF3_D342_Orb_NR_Cal_dB_TC	175375	34.10	760.16	794.26
249	Sentinel-1b		1	NAH	Unneruskollen Island	Some use of semi-automatic edge detection in sea-ice free areas.	2017	S1B_IW_GRDH_1SSH_20170225T034736_20170225T034801_004451_007BF3_D342_Orb_NR_Cal_dB_TC	27820	34.10	760.16	794.26
250	Sentinel-1b		1	NAH	Jelbart Ice Shelf	Some use of semi-automatic edge detection in sea-ice free areas.	2017	S1B_IW_GRDH_1SSH_20170225T034736_20170225T034801_004451_007BF3_D342_Orb_NR_Cal_dB_TC	83097	34.10	760.16	794.26
251	Sentinel-1b		1	NAH	Jelbart Ice Shelf	Some areas with sea ice.	2017	S1B_IW_GRDH_1SSH_20170225T034707_20170225T034736_004451_007BF3_69F7_Orb_NR_Cal_dB_TC	174040	62.90	760.16	823.06

252	Sentinel-1b		1	NAH	Blåskimen Island	Some areas with sea ice.	2017	S1B_IW_GRDH_1SSH_20170225T034707_20170225T034736_004451_007BF3_69F7_Orb_NR_Cal_dB_TC	38646	62.90	760.16	823.06
253	Landsat 8	OLI	1	NAH	Berkner Island		2019	LC08_L1GT_189116_20190119_20190201_01_T2_B8	101113	34.82	43.88	78.70
254	Landsat 8	OLI	1	NAH	Filchner Ice Shelf	Heavily crevassed areas near to the boundary with Berkner Island made picking out the ice fronts difficult	2019	LC08_L1GT_189116_20190119_20190201_01_T2_B8	267545	34.82	43.88	78.70
255	Landsat 8	OLI	1	NAH	Filchner Ice Shelf	Marginal areas in the nortern part of the ice shelf hesavily crevassed, making picking out the ice fronts difficult	2019	LC08_L1GT_187116_20190206_20190221_01_T2_B8	222459	34.82	43.88	78.70
256	Landsat 8	OLI	2	NAH	Coats Land	Difficult to differentiate between ice shelf edge and ice bergs, especially where they appear to have partially calved	2019	LC08_L1GT_187116_20190206_20190221_01_T2_B8	79760	34.82	43.88	78.70
257	Landsat 8	OLI	1	NAH	Coats Land		2019	LC08_L1GT_187115_20190206_20190221_01_T2_B8	34992	34.82	43.88	78.70
258	Landsat 8	OLI	2	NAH	Coats Land		2019	LC08_L1GT_187115_20190206_20190221_01_T2_B8	88619	34.82	43.88	78.70
259	Landsat 8	OLI	1	NAH	Coats Land		2019	LC08_L1GT_187115_20190206_20190221_01_T2_B8	33663	34.82	43.88	78.70
260	Sentinel-1b		1	NAH	Coats Land		2019	S1B_IW_GRDH_1SSH_20190122T035020_20190122T035047_014601_01B34D_4236_Orb_NR_Cal_dB_TC	255946	62.90	760.16	823.06
261	Sentinel-1b		1	NAH	Brunt_Stancomb Ice Shelf	Some heaily crevassed areas making exact locations difficult to locate	2019	S1B_IW_GRDH_1SSH_20190122T034955_20190122T035020_014601_01B34D_0795_Orb_NR_Cal_dB_TC	389619	62.90	760.16	823.06

262	Sentinel-1b		1	NAH	Brunt_Stancomb Ice Shelf	Brunt Ice Shelf is extremely crevassed an consists of ice bergs joined together. Ice front is judged to be the outermost icebergs which appear attahced to the ice shelf	2019	S1B_IW_GRDH_1SSH_20190122T034930_20190122T034955_014601_01B34D_BFD6_Orb_NR_Cal_dB_TC	460868	62.90	760.16	823.06
263	Sentinel-1b		2	NAH	Brunt_Stancomb Ice Shelf	Some heaily crevassed areas making exact locations difficult to locate	2019	S1B_IW_GRDH_1SSH_20190122T034930_20190122T034955_014601_01B34D_BFD6_Orb_NR_Cal_dB_TC	620842	62.90	760.16	823.06
264	Sentinel-1b		1	NAH	Brunt_Stancomb Ice Shelf		2019	S1B_IW_GRDH_1SSH_20190105T233047_20190105T233112_014365_01ABB5_7CC3_Orb_NR_Cal_dB_TC	40321	62.90	760.16	823.06
265	Landsat 8	OLI	1	NAH	Brunt_Stancomb Ice Shelf		2019	LC08_L1GT_185113_20190107_20190130_01_T2_B8	20545	34.82	43.88	78.70
266	Landsat 8	OLI	1	NAH	Brunt_Stancomb Ice Shelf		2019	LC08_L1GT_185112_20190123_20190205_01_T2_B8	44772	34.82	43.88	78.70
267	Sentinel-1b		1	NAH	Riiser-Larsen Ice Shelf		2019	S1B_IW_GRDH_1SSH_20190122T034905_20190122T034930_014601_01B34D_A853_Orb_NR_Cal_dB_TC	133037	62.90	760.16	823.06
268	Landsat 8	OLI	1	NAH	Riiser-Larsen Ice Shelf		2019	LC08_L1GT_184111_20190217_20190222_01_T2_B8	44033	34.82	43.88	78.70
269	Sentinel-1b		1	NAH	Riiser-Larsen Ice Shelf		2019	S1B_IW_GRDH_1SSH_20190122T034905_20190122T034930_014601_01B34D_A853_Orb_NR_Cal_dB_TC	98910	62.90	760.16	823.06
270	Sentinel-1b		2	NAH	Riiser-Larsen Ice Shelf		2019	S1B_IW_GRDH_1SSH_20190122T034905_20190122T034930_014601_01B34D_A853_Orb_NR_Cal_dB_TC	156898	62.90	760.16	823.06
271	Landsat 8	OLI	1	NAH	Riiser-Larsen Ice Shelf		2019	LC08_L1GT_184111_20190217_20190222_01_T2_B8	66497	34.82	43.88	78.70

272	Sentinel-1b		1	NAH	Riiser-Larsen Ice Shelf		2019	S1B_IW_GRDH_1SSH_20190122T034840_20190122T034905_014601_01B34D_C0AB_Orb_NR_Cal_dB_TC	508961	62.90	760.16	823.06
273	Sentinel-1b		1	NAH	Riiser-Larsen Ice Shelf		2019	S1B_IW_GRDH_1SSH_20190122T034815_20190122T034840_014601_01B34D_4F40_Orb_NR_Cal_dB_TC	121227	62.90	760.16	823.06
274	Sentinel-1b		1	NAH	Quar Ice Shelf		2019	S1B_IW_GRDH_1SSH_20190215T034814_20190215T034839_014951_01BEAC_C3E3_Orb_NR_Cal_dB_TC	116358	62.90	760.16	823.06
275	Sentinel-1b		1	NAH	Ekstrom Ice Shelf	Some sea ice at the coast making digitisation slightly difficult	2019	S1B_IW_GRDH_1SSH_20190202T212048_20190202T212113_014772_01B8D2_E80D_Orb_NR_Cal_dB_TC	267596	62.90	760.16	823.06
276	Sentinel-1b		1	NAH	Unneruskollen Island		2019	S1B_IW_GRDH_1SSH_20190130T205628_20190130T205654_014728_01B769_D7E5_Orb_NR_Cal_dB_TC	28922	62.90	760.16	823.06
277	Sentinel-1b		1	NAH	Blåskimen Island		2019	S1B_IW_GRDH_1SSH_20190130T205628_20190130T205654_014728_01B769_D7E5_Orb_NR_Cal_dB_TC	38321	62.90	760.16	823.06
278	Sentinel-1b		2	NAH	Jelbart Ice Shelf	Margin of ice shelf has many cracks and crevasses	2019	S1B_IW_GRDH_1SSH_20190130T205628_20190130T205654_014728_01B769_D7E5_Orb_NR_Cal_dB_TC	391854	62.90	760.16	823.06
279	Landsat 8	OLI	1	NAH	Fimbul Ice Shelf		2019	LC08_L1GT_171109_20190222_20190308_01_T2_B8	215841	34.82	43.88	78.70
280	Landsat 8	OLI	1	NAH	Fimbul Ice Shelf	Sea ice making manual digitisation difficult	2019	LC08_L1GT_168110_20190201_20190206_01_T2_B8	55302	34.82	43.88	78.70
281	Sentinel-1b		1	NAH	Fimbul Ice Shelf		2019	S1B_IW_GRDH_1SSH_20190130T205603_20190130T205628_014728_01B	43206	62.90	760.16	823.06

								769_6EA1_Orb_NR_Cal_dB_TC				
282	Landsat 8	OLI	2	NAH	Fimbul Ice Shelf	Clear imagery, but manual distinction between icebergs and ice shelf and sea ice difficult, especially in complex, heavily crevassed areas	2019	LC08_L1GT_173109_20190220_20190308_01_T2_B8	397274	34.82	43.88	78.70
283	Landsat 8	OLI	1	NAH	Fimbul Ice Shelf		2019	LC08_L1GT_171110_20190222_20190308_01_T2_B8	270274	34.82	43.88	78.70
284	Sentinel-1b		1	NAH	Fimbul Ice Shelf	Some areas of sea ice at the margin	2019	S1B_IW_GRDH_1SSH_20190203T034721_20190203T034750_014776_01B8F5_A653_Orb_NR_Cal_dB_TC	297590	62.90	760.16	823.06
285	Sentinel-1b		1	NAH	Coats Land	Some heaily crevassed areas making exact locations difficult to locate	2019	S1B_IW_GRDH_1SSH_20190122T034955_20190122T035020_014601_01B34D_0795_Orb_NR_Cal_dB_TC	153068	62.90	760.16	823.06
286	Sentinel-1b		2	NAH	Lyddan Island		2019	S1B_IW_GRDH_1SSH_20190122T034930_20190122T034955_014601_01B34D_BFD6_Orb_NR_Cal_dB_TC	38988	62.90	760.16	823.06
287	Sentinel-1b		1	NAH			2019	S1B_IW_GRDH_1SSH_20190215T034814_20190215T034839_014951_01BEAC_C3E3_Orb_NR_Cal_dB_TC	20577	62.90	760.16	823.06
288	Sentinel-1b		1	NAH	Lyddan Island		2019	S1B_IW_GRDH_1SSH_20190122T034905_20190122T034930_014601_01B34D_A853_Orb_NR_Cal_dB_TC	50087	62.90	760.16	823.06
289	Sentinel-1b		1	NAH	Cape Norvegia		2019	S1B_IW_GRDH_1SSH_20190122T034815_20190122T034840_014601_01B34D_4F40_Orb_NR_Cal_dB_TC	71463	62.90	760.16	823.06

290	Sentinel-1b		1	NAH	Ekstrom Ice Shelf		2019	S1B_IW_GRDH_1SSH_20190215T034814_20190215T034839_014951_01BEAC_C3E3_Orb_NR_Cal_dB_TC	9165	62.90	760.16	823.06
291	Sentinel-1b		1	NAH	Atka Ice Shelf	Some sea ice at the coast making digitisation slightly difficult	2019	S1B_IW_GRDH_1SSH_20190202T212048_20190202T212113_014772_01B8D2_E80D_Orb_NR_Cal_dB_TC	93823	62.90	760.16	823.06
292	Sentinel-1b		1	NAH	Atka Ice Shelf		2019	S1B_IW_GRDH_1SSH_20190130T205628_20190130T205654_014728_01B769_D7E5_Orb_NR_Cal_dB_TC	23041	62.90	760.16	823.06
293	Sentinel-1b		1	NAH	Fimbul Ice Shelf		2019	S1B_IW_GRDH_1SSH_20190130T205628_20190130T205654_014728_01B769_D7E5_Orb_NR_Cal_dB_TC	30058	62.90	760.16	823.06

Appendix II: Digitising Error Statistics (± m)

Platform	Sensor	Measure	Manual	Edge Extracted
Sentinal-1 EW	EW	Mean	102.7	2.1
Sentinal-1 EW	EW	Max	3331.3	76.5
Sentinal-1 EW	EW	Median	51.3	1.4
Sentinal-1 EW	EW	SD	233.8	4.1
Sentinel-1 IW	IW	Mean	62.9	5.3
Sentinel-1 IW	IW	Max	1875.6	122.2
Sentinel-1 IW	IW	Median	30.6	2.9
Sentinel-1 IW	IW	SD	132.1	8.9
Landsat Optical	OLI	Mean	34.8	2.6
Landsat Optical	OLI	Max	1411.0	62.6
Landsat Optical	OLI	Median	24.7	2.4
Landsat Optical	OLI	SD	55.4	1.8
Landsat Optical	ETM+	Mean	34.8	2.6
Landsat Optical	ETM+	Max	1411.0	62.6
Landsat Optical	ETM+	Median	24.7	2.4
Landsat Optical	ETM+	SD	55.4	1.8
1963_Argon		Mean	106.0	
1963_Argon		Max	963.747	
1963_Argon		Median	82.39849	
1963_Argon		SD	96.80501	

Appendix III: Measured Co-registration Errors (± m)

Scene	Sensor	Control Point	Distance from Control Point (m)
S1A_EW_GRDM_1SSH_20150126T025339_20150126T025443_004336_00549F_10D7_Orb_NR_Cal_dB_TC	EW	1	2436.4
S1A_EW_GRDM_1SSH_20150204T022920_20150204T023024_004467_0057A0_9052_Orb_NR_Cal_dB_TC	EW	1	2172.0
S1A_EW_GRDM_1SSH_20150201T020504_20150201T020537_004423_00568B_BED9_Orb_NR_Cal_dB_TC	EW	1	2091.8
S1A_EW_GRDM_1SSH_20150205T013242_20150205T013346_004481_0057F2_B7C3_Orb_NR_Cal_dB_TC	EW	1	2050.7
S1A_EW_GRDM_1SSH_20150126T025339_20150126T025443_004336_00549F_10D7_Orb_NR_Cal_dB_TC	EW	2	1644.3
S1A_EW_GRDM_1SSH_20150205T013242_20150205T013346_004481_0057F2_B7C3_Orb_NR_Cal_dB_TC	EW	2	1489.5
S1A_EW_GRDM_1SSH_20150201T020504_20150201T020537_004423_00568B_BED9_Orb_NR_Cal_dB_TC	EW	2	1466.3
S1A_EW_GRDM_1SSH_20150204T022920_20150204T023024_004467_0057A0_9052_Orb_NR_Cal_dB_TC	EW	2	1464.1
S1A_EW_GRDM_1SSH_20170214T215328_20170214T215432_015285_0190D5_5CD4_Orb_NR_Cal_dB_TC	EW	3	472.7
S1B_EW_GRDM_1SSH_20170114T224933_20170114T225038_003850_006A04_C591_Orb_NR_Cal_dB_TC	EW	3	273.0
S1B_IW_GRDH_1SSH_20170213T034851_20170213T034916_004276_0076B2_774E_Orb_NR_Cal_dB_TC	IW	3	509.1
S1B_IW_GRDH_1SSH_20170201T034851_20170201T034916_004101_007180_8182_Orb_NR_Cal_dB_TC	IW	3	507.9
S1B_IW_GRDH_1SSH_20170225T034851_20170225T034916_004451_007BF3_6126_Orb_NR_Cal_dB_TC	IW	3	506.4
S1B_IW_GRDH_1SSH_20170108T034852_20170108T034917_003751_00672A_6EAB_Orb_NR_Cal_dB_TC	IW	3	487.3
S1A_IW_GRDH_1SSH_20150525T034905_20150525T034930_006072_007DBB_048B_Orb_NR_Cal_dB_TC	IW	3	479.0
LC08_L1GT_182112_20170317_20170328_01_T2_B8	OLI	3	65.9
LC08_L1GT_179112_20190214_20190222_01_T2_B8	OLI	3	43.9
LE07_L1GT_179112_20090109_20161223_01_T2_B8	ETM+	3	29.6
LC08_L1GT_179112_20190129_20190206_01_T2_B8	OLI	3	25.3
LC08_L1GT_179112_20171107_20171121_01_T2_B8	OLI	3	24.2
S1A_EW_GRDM_1SSH_20170214T215328_20170214T215432_015285_0190D5_5CD4_Orb_NR_Cal_dB_TC	EW	4	715.2
S1B_EW_GRDM_1SSH_20170114T224933_20170114T225038_003850_006A04_C591_Orb_NR_Cal_dB_TC	EW	4	450.1
S1B_IW_GRDH_1SSH_20170108T034852_20170108T034917_003751_00672A_6EAB_Orb_NR_Cal_dB_TC	IW	4	626.3

S1B_IW_GRDH_1SSH_20170201T034851_20170201T034916_004101_007180_8182_Orb_NR_Cal_dB_TC	IW	4	624.6
S1B_IW_GRDH_1SSH_20170201T034851_20170201T034916_004101_007180_8182_Orb_NR_Cal_dB_TC	IW	4	621.9
S1B_IW_GRDH_1SSH_20170225T034851_20170225T034916_004451_007BF3_6126_Orb_NR_Cal_dB_TC	IW	4	618.0
S1A_IW_GRDH_1SSH_20160811T034929_20160811T034954_012547_013A63_1916_Orb_NR_Cal_dB_TC	IW	4	613.9
S1A_IW_GRDH_1SSH_20150525T034905_20150525T034930_006072_007DBB_048B_Orb_NR_Cal_dB_TC	IW	4	611.6
LC08_L1GT_179112_20190214_20190222_01_T2_B8	OLI	4	128.1
LC08_L1GT_179112_20190129_20190206_01_T2_B8	OLI	4	123.4
LE07_L1GT_179112_20090109_20161223_01_T2_B8	ETM+	4	46.0
LC08_L1GT_179112_20171107_20171121_01_T2_B8	OLI	4	30.9
LC08_L1GT_182112_20170317_20170328_01_T2_B8	OLI	4	14.8
LE07_L1GT_179112_20090125_20161222_01_T2_B8	ETM+	4	8.3
S1B_IW_GRDH_1SSH_20170108T034737_20170108T034802_003751_00672A_88EF_Orb_NR_Cal_dB_TC	IW	5	2125.2
S1B_IW_GRDH_1SSH_20170120T034736_20170120T034801_003926_006C45_B48B_Orb_NR_Cal_dB_TC	IW	5	2124.6
S1B_IW_GRDH_1SSH_20170213T034736_20170213T034801_004276_0076B2_EE94_Orb_NR_Cal_dB_TC	IW	5	2118.3
S1B_IW_GRDH_1SSH_20170225T034736_20170225T034801_004451_007BF3_D342_Orb_NR_Cal_dB_TC	IW	5	2113.0
S1A_EW_GRDM_1SSH_20150204T204009_20150204T204113_004478_0057E4_CED9_Orb_NR_Cal_dB_TC	EW	5	3711.2
LC08_L1GT_177110_20150205_20170413_01_T2_B8	OLI	5	43.9
S1A_EW_GRDM_1SSH_20150130T203155_20150130T203259_004405_00561F_33F9_Orb_NR_Cal_dB_TC	EW	6	660.6
S1A_EW_GRDM_1SSH_20150204T204009_20150204T204113_004478_0057E4_CED9_Orb_NR_Cal_dB_TC	EW	6	505.0
S1A_EW_GRDM_1SSH_20150204T204009_20150204T204113_004478_0057E4_CED9_Orb_NR_Cal_dB_TC	EW	6	303.9
LE07_L1GT_176110_20130131_20161125_01_T2_B8	ETM+	6	447.0
LE07_L1GT_176110_20121230_20190516_01_T2_B8	ETM+	6	434.4
LC08_L1GT_175110_20170127_20170214_01_T2_B8	OLI	6	354.6
LE07_L1GT_174110_20130218_20161126_01_T2_B8	ETM+	6	310.8
S1A_EW_GRDM_1SSH_20150204T204009_20150204T204113_004478_0057E4_CED9_Orb_NR_Cal_dB_TC	EW	7	476.6
S1B_IW_GRDH_1SSH_20170120T034736_20170120T034801_003926_006C45_B48B_Orb_NR_Cal_dB_TC	IW	7	203.2
S1B_IW_GRDH_1SSH_20170201T034736_20170201T034801_004101_007180_BAB6_Orb_NR_Cal_dB_TC	IW	7	187.5
S1B_IW_GRDH_1SSH_20170213T034736_20170213T034801_004276_0076B2_EE94_Orb_NR_Cal_dB_TC	IW	7	182.0
LE07_L1GT_176110_20090221_20161222_01_T2_B8	ETM+	7	175.0

S1B_IW_GRDH_1SSH_20170225T034736_20170225T034801_004451_007BF3_D342_Orb_NR_Cal_dB_TC	IW	7	154.8
LE07_L1GT_177110_20110101_20161211_01_T2_B8	ETM+	7	143.3
LC08_L1GT_177110_20150205_20170413_01_T2_B8	OLI	7	135.0
LE07_L1GT_177110_20110117_20161210_01_T2_B8	ETM+	7	109.9
S1B_IW_GRDH_1SSH_20170108T034737_20170108T034802_003751_00672A_88EF_Orb_NR_Cal_dB_TC	IW	7	98.9
S1A_EW_GRDM_1SSH_20150130T203155_20150130T203259_004405_00561F_33F9_Orb_NR_Cal_dB_TC	EW	8	894.3
S1A_EW_GRDM_1SSH_20150204T204009_20150204T204113_004478_0057E4_CED9_Orb_NR_Cal_dB_T	EW	8	873.9
LE07_L1GT_174110_20130218_20161126_01_T2_B8	ETM+	8	126.9
LE07_L1GT_174110_20110301_20161209_01_T2_B8	ETM+	8	73.3
LC08_L1GT_175110_20170127_20170214_01_T2_B8	OLI	8	62.9
LC08_L1GT_175110_20150207_20170413_01_T2_B8	OLI	8	47.4
S1B_IW_GRDH_1SSH_20170213T034826_20170213T034851_004276_0076B2_EDD6_Orb_NR_Cal_dB_TC	IW	9	449.1
S1B_IW_GRDH_1SSH_20170108T034827_20170108T034852_003751_00672A_2BF7_Orb_NR_Cal_dB_TC	IW	9	446.2
S1B_IW_GRDH_1SSH_20170225T034826_20170225T034851_004451_007BF3_7C17_Orb_NR_Cal_dB_TC	IW	9	446.1
S1B_IW_GRDH_1SSH_20170120T034826_20170120T034851_003926_006C45_BECD_Orb_NR_Cal_dB_TC	IW	9	443.9
LE07_L1GT_180111_20130228_20161125_01_T2_B8	ETM+	9	108.1
S1A_EW_GRDM_1SSH_20150203T195906_20150203T200010_004463_005788_080D_Orb_NR_Cal_dB_TC	EW	10	4359.5
LC08_L1GT_170110_20150204_20170413_01_T2_B8	OLI	10	44.7
LC08_L1GT_170110_20170124_20170311_01_T2_B8	OLI	10	27.1
S1B_IW_GRDH_1SSH_20190227T034839_20190227T034904_015126_01C475_16BF_Orb_NR_Cal_dB_TC	IW	11	1058.5
S1B_IW_GRDH_1SSH_20190203T034840_20190203T034905_014776_01B8F5_0D6E_Orb_NR_Cal_dB_TC	IW	11	1055.8
S1A_IW_GRDH_1SSH_20160811T034929_20160811T034954_012547_013A63_1916_Orb_NR_Cal_dB_TC	IW	11	1049.2
S1A_IW_GRDH_1SSH_20150525T034905_20150525T034930_006072_007DBB_048B_Orb_NR_Cal_dB_TC	IW	11	1049.1
S1B_IW_GRDH_1SSH_20190227T034839_20190227T034904_015126_01C475_16BF_Orb_NR_Cal_dB_TC	IW	11	1044.7
S1A_EW_GRDM_1SSH_20170214T215328_20170214T215432_015285_0190D5_5CD4_Orb_NR_Cal_dB_TC	EW	11	1364.5
LC08_L1GT_179112_20190129_20190206_01_T2_B8	OLI	11	36.6
LC08_L1GT_179112_20190214_20190222_01_T2_B8	OLI	11	35.7
LC08_L1GT_179112_20171107_20171121_01_T2_B8	OLI	11	29.4
LE07_L1GT_179112_20090125_20161222_01_T2_B8	ETM+	11	15.9

S1B_IW_GRDH_1SSH_20190203T034840_20190203T034905_014776_01B8F5_0D6E_Orb_NR_Cal_dB_TC	IW	12	767.6
S1A_IW_GRDH_1SSH_20150525T034905_20150525T034930_006072_007DBB_048B_Orb_NR_Cal_dB_TC	IW	12	764.6
LE07_L1GT_179112_20090125_20161222_01_T2_B8	ETM+	12	755.6
S1B_IW_GRDH_1SSH_20190227T034839_20190227T034904_015126_01C475_16BF_Orb_NR_Cal_dB_TC	IW	12	748.3
S1A_EW_GRDM_1SSH_20161201T212903_20161201T213007_014191_016EDE_1ED2_Orb_NR_Cal_dB_TC	EW	12	574.1
S1A_EW_GRDM_1SSH_20170214T215328_20170214T215432_015285_0190D5_5CD4_Orb_NR_Cal_dB_TC	EW	12	489.6
LE07_L1GT_179112_20090109_20161223_01_T2_B8	ETM+	12	27.0
LC08_L1GT_179112_20190129_20190206_01_T2_B8	OLI	12	26.7
LC08_L1GT_179112_20190214_20190222_01_T2_B8	OLI	12	23.5
LC08_L1GT_179112_20171107_20171121_01_T2_B8	OLI	12	22.7
S1A_IW_GRDH_1SSH_20190308T023458_20190308T023521_026240_02EE5D_2654_Orb_TC	IW	13	2581.7
S1A_EW_GRDM_1SSH_20170417T195919_20170417T195943_016188_01AC0E_6504_Orb_NR_Cal_dB_TC	EW	13	4496.3
S1A_EW_GRDM_1SSH_20150227T195906_20150227T200010_004813_005FC1_D8A1_Orb_NR_Cal_dB_TC	EW	13	4410.0
LE07_L1GT_169111_20111109_20161205_01_T2_B8	ETM+	13	88.4
LC08_L1GT_168111_20190217_20190222_01_T2_B8	OLI	13	63.0
LC08_L1GT_166111_20190219_20190222_01_T2_B8	OLI	13	26.6
LE07_L1GT_167111_20111111_20161205_01_T2_B8	ETM+	13	22.8
S1B_IW_GRDH_1SSH_20190203T034840_20190203T034905_014776_01B8F5_0D6E_Orb_NR_Cal_dB_TC	IW	14	1434.7
S1B_IW_GRDH_1SSH_20190227T034839_20190227T034904_015126_01C475_16BF_Orb_NR_Cal_dB_TC	IW	14	1422.1
S1A_IW_GRDH_1SSH_20150525T034905_20150525T034930_006072_007DBB_048B_Orb_NR_Cal_dB_TC	IW	14	1415.3
S1B_IW_GRDH_1SSH_20190227T034839_20190227T034904_015126_01C475_16BF_Orb_NR_Cal_dB_TC	IW	14	1401.0
S1A_EW_GRDM_1SSH_20161201T212903_20161201T213007_014191_016EDE_1ED2_Orb_NR_Cal_dB_TC	EW	14	2341.3
S1A_EW_GRDM_1SSH_20170214T215328_20170214T215432_015285_0190D5_5CD4_Orb_NR_Cal_dB_TC	EW	14	1479.3
LC08_L1GT_179112_20190214_20190222_01_T2_B8	OLI	14	49.0
LC08_L1GT_179112_20190129_20190206_01_T2_B8	OLI	14	29.5
LC08_L1GT_179112_20171107_20171121_01_T2_B8	OLI	14	15.3
LE07_L1GT_179112_20090125_20161222_01_T2_B8	ETM+	14	12.4

Appendix IV: Calculated Ice Shelf Areas

Area (km²)	1963	1974	1990	2000	2004	2009	2011	2012	2013	2014	2015	2017	2019	Total
Fimbul	43,302.8	39,532.1	40,175.1	40,643.9	40,905.0	40,781.7	40,750.1	41,057.0	40,877.8	41,124.4	41,064.3	41,161.8	41,260.6	532,636.6
Jelbart	11,563.9		10,388.3	10,660.5	10,745.3	10,878.5	10,943.2	11,016.8	11,020.5	11,117.7	11,106.5	11,181.6	11,206.6	131,829.4
Atka	1,983.7	1,870.4	1,898.4	1,955.8	1,990.4	1,981.2	1,836.1	1,828.7	1,831.9	1,833.9	1,845.3	1,850.9	1,857.1	24,564.0
Ekstrøm	7,578.9	7,382.6	6,688.3	6,788.7	6,786.5	6,853.0	6,880.8	6,865.3	6,863.0	6,888.9	6,906.4	6,922.0	6,948.2	90,352.5
Quar	2,239.5	2,121.8	2,156.0	2,139.0	2,124.6	2,153.8	2,161.8	2,168.9	2,166.2	2,172.5	2,180.3	2,184.8	2,190.1	28,159.3
Riiser-Larsen	44,778.6	43,751.4	42,078.8	42,548.4	42,869.8	42,880.8	43,001.8	43,083.1	43,076.3	43,250.3	43,240.7	43,356.8	43,454.6	561,371.4
Stancomb-Wills			26,656.9	28,165.1	28,959.6	28,791.4	29,105.2	29,580.0	29,332.9	30,002.3	29,597.0	29,868.7	30,159.5	320,218.6
Brunt			6,207.8	6,822.0	7,099.8	7,496.1	7,581.5	7,675.3	7,667.7	7,722.6	7,770.4	7,809.5	7,913.0	81,765.5
Filchner	99,593.0	101,946.0	91,692.5	94,031.1	94,002.2	94,961.5	95,398.0	95,674.4	95,730.8	95,937.2	96,174.4	96,668.9	97,135.9	1,248,945.9
Dawson-Lambton	79.8	71.0	17.5	14.4	24.1	21.6	24.0	28.3	26.6	29.6	30.0	34.2	37.3	438.4
Hayes	8.6	9.6	12.8	12.5	13.6	8.6	11.5	11.1	11.0	11.6	12.6	13.8	11.2	148.5
Mann	2.7	7.6	3.5	6.4	5.7	4.3	3.5	4.0	3.5	5.7	3.3	6.4	3.8	60.5
Mosley		2.5	12.2	13.4	13.9	10.7	13.1	7.7	6.0	10.5	7.5	5.9	5.8	109.2
Schweitzer		96.3	114.5	140.1	149.1	149.5	152.9	156.0	154.7	173.1	159.7	161.7	164.5	1,772.1
Wiedenmanngletscher			111.4	87.9	68.8	32.8	33.9	39.8	35.5	49.9	32.8	29.3	31.2	553.2
Glacier 1		2.6	1.1	1.4	1.7	1.4	0.5	1.3	0.8	1.7	0.6	0.8	1.2	14.9
Total	211,131.5	196,794.0	228,215.1	234,030.7	235,759.9	237,006.9	237,898.0	239,197.7	238,805.1	240,331.9	240,131.6	241,257.1	242,380.6	3,022,940.1

Appendix V: Ice-shelf Widths Calculated Using the Oriented Minimum Bounding Box Method

Ice Shelf	Width (km)
Fimbul	387,228
Riiser-Larsen	356,820
Filchner	186,973
Stancomb-Wills	116,881
Brunt	115,970
Jelbart	94,052
Ekstrøm	81,409
Atka	56,251
Quar	38,717
Schweitzer	11,896
Wiedenmangletscher	7,880
Mosley	7,389
Dawson-Lambton	7,170
Hayes	6,738
Mann	5,149
Glacier 1	678

Appendix VI: Estimated Error in Calculated Ice Shelf Areas

Error (± km²)	1963	1974	1990	2000	2004	2009	2011	2012	2013	2014	2015	2017	2019	Total
Fimbul	(42,838.52 to 43,886.18)	81.3	71.6	29.0	96.8	37.4	40.9	29.0	38.6	96.8	341.7	116.8	112.1	1,092.1
Jelbart	50.9		17.4	7.1	23.5	8.7	9.6	7.1	8.7	23.5	11.7	77.2	77.4	322.7
Atka	30.5	11.8	10.4	4.2	14.1	5.4	5.2	4.2	5.0	14.1	77.1	44.7	46.3	272.9
Ekstrøm	44.1	17.1	15.1	6.1	20.4	8.3	7.2	6.1	7.2	20.4	115.3	65.2	67.0	399.5
Quar	21.0	8.1	7.2	2.9	9.7	4.4	3.4	2.9	3.4	9.7	54.9	30.8	31.9	190.1
Riiser-Larsen	193.2	74.9	66.0	26.8	89.2	35.6	33.5	26.8	33.5	89.2	505.6	255.1	267.7	1,697.0
Stancomb-Wills			21.6	8.8	29.2	11.6	11.8	8.8	11.8	29.2	101.2	88.8	92.6	415.5
Brunt			21.5	8.7	29.0	11.5	11.7	8.7	11.7	29.0	100.5	88.1	91.9	412.2
Filchner	(99,079.95 to 99,795.65)	39.3	34.6	14.0	46.7	20.1	18.1	14.0	17.6	46.7	162.8	11.7	14.7	440.2
Dawson-Lambton	3.9	1.5	1.3	0.5	1.8	0.7	0.7	0.5	0.7	1.8	0.5	4.1	3.9	21.9
Hayes	3.7	1.4	1.2	0.5	1.7	0.6	0.7	0.5	0.7	1.7	0.5	3.8	3.7	20.6
Mann	2.8	1.1	1.0	0.4	1.3	0.5	0.5	0.4	0.5	1.3	0.3	2.9	2.8	15.8
Mosley		1.6	1.4	0.6	1.8	0.7	0.7	0.6	0.7	1.8	0.5	4.2	4.1	18.6
Schweitzer		2.5	2.2	0.9	3.0	1.1	1.1	0.9	1.1	3.0	0.8	6.7	6.5	30.0
Wiedenmangletscher			1.5	0.6	2.0	0.8	0.8	0.6	0.8	2.0	0.5	4.5	4.3	18.2
Glacier 1		0.1	0.1	0.1	0.2	0.1	0.1	0.1	0.1	0.2	0.0	0.4	0.4	1.7
Total	350.0	240.7	274.0	111.1	370.3	147.3	145.9	111.1	142.1	370.3	1,473.8	805.0	827.4	5,369.0

Appendix VII: Settings used for the ESRI ArcMap ArcScan Trace Tool

Intersection Solution:	*Geometrical*
Maximum Line Width:	*20*
Noise Level:	*65*
Compression Tolerance:	*0.025*
Smoothing Weight:	*1*
Gap Closure Tolerance:	*30*

Appendix VIII: Average Austral Summer Surface Temperatures (2 m) on the EWS Ice Shelves Over the Past Decade

2009 – 2019 average DJF surface temperatures

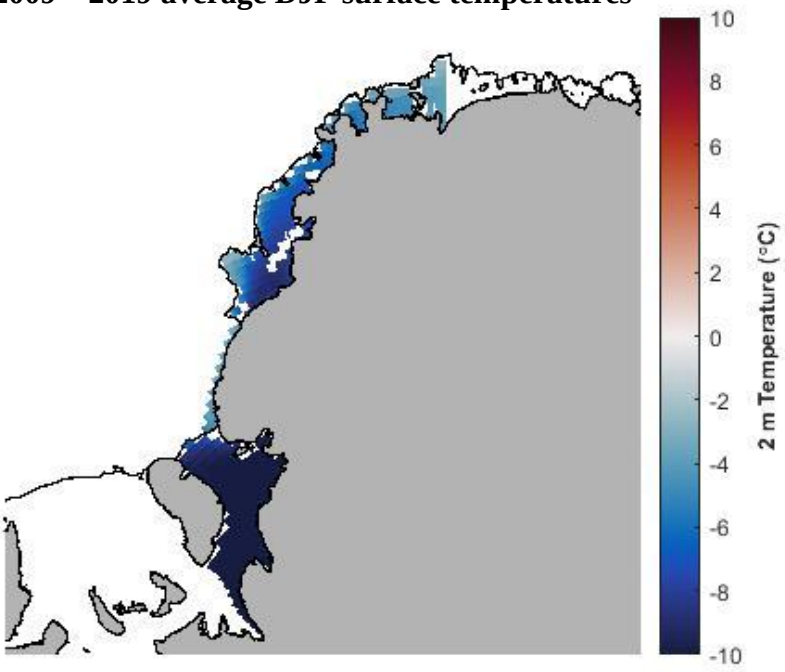

Source: ERA5 reanalysis data, as discussed in text .